

Universiteit
Leiden
The Netherlands

Endomembrane mutiny: how picornaviruses hijack host organelles to support their replication

Melia, C.E.

Citation
Melia, C. E. (2019, May 21). *Endomembrane mutiny: how picornaviruses hijack host organelles to support their replication*. Retrieved from https://hdl.handle.net/1887/73640

Version:	Not Applicable (or Unknown)
License:	Leiden University Non-exclusive license
Downloaded from:	https://hdl.handle.net/1887/73640

Note: To cite this publication please use the final published version (if applicable).

Cover Page



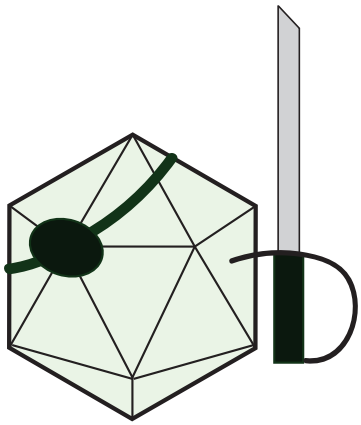
Universiteit Leiden



The handle http://hdl.handle.net/1887/73640 holds various files of this Leiden University dissertation.

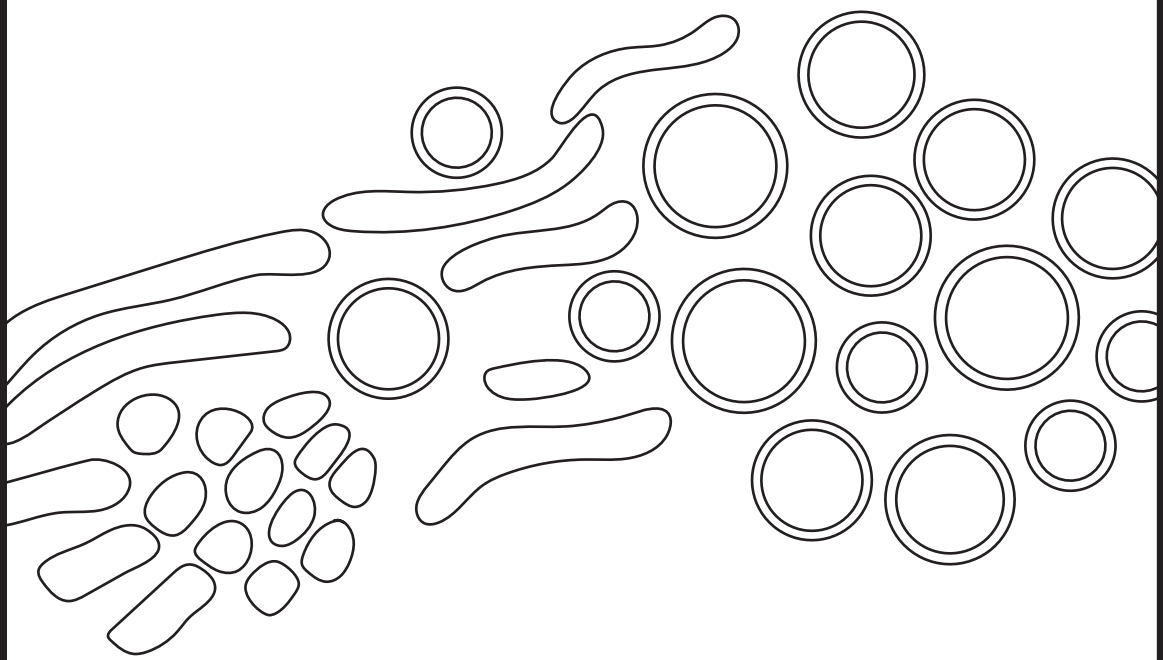
Author: Melia, C.E.
Title: Endomembrane mutiny: how picornaviruses hijack host organelles to support their replication
Issue Date: 2019-05-21

Endomembrane mutiny



How picornaviruses hijack host organelles to support their replication

Charlotte E. Melia



ENDOMEMBRANE MUTINY:

HOW PICORNAVIRUSES HIJACK HOST ORGANELLES TO SUPPORT THEIR REPLICATION

Charlotte E. Melia

PhD Thesis, Leiden University, 2019.

The research described in this thesis was performed at Leiden University Medical Center, Section Electron Microscopy, Leiden, The Netherlands and at University Utrecht, Faculty of Veterinary Medicine, Utrecht, The Netherlands.

This work was financially supported in part by the European Union 7th Framework; EUVIRNA Marie Curie Initial Training Network, grant agreement 264286 to prof. dr. F. van Kuppeveld.

Cover design by Charlotte E. Melia

Printed by: GVO drukkers & vormgevers B.V., Ede

ISBN: 978-94-6332-497-7

Copyright © 2019, Charlotte E. Melia, all rights reserved

ENDOMEMBRANE MUTINY:

HOW PICORNAVIRUSES HIJACK HOST ORGANELLES TO SUPPORT THEIR REPLICATION

Proefschrift

ter verkrijging van
de graad van Doctor aan de Universiteit Leiden,
op gezag van Rector Magnificus prof.mr. C.J.J.M. Stolker,
volgens besluit van het College voor Promoties
te verdedigen op dinsdag 21 mei 2019
klokke 13.45 uur

door

Charlotte Ellen Melia
geboren te Bolton, Verenigd Koninkrijk
in 1989

Promotoren:	Prof. dr. A.J. Koster Prof. dr. F.J.M. van Kuppeveld, Utrecht University
Co-promotor:	Dr. M. Bárcena
Leden Promotiecommissie:	Prof. dr. E.J. Snijder Prof. dr. A. Akhmanova, Utrecht University Prof. dr. R.C. Hoeben Prof. dr. J.M. Smit, Groningen University

Mum, dad, Dan, gran

TABLE OF CONTENTS

CHAPTER 1	General Introduction and thesis outline	**7**
CHAPTER 2	Illuminating the Sites of Enterovirus Replication in Living Cells by Using a Split-GFP-tagged Viral Protein	**23**
CHAPTER 3	Escaping Host Factor PI4KB Inhibition: Enterovirus Genomic RNA Replication in the Absence of Replication Organelles	**47**
CHAPTER 4	The Emergence of Enterovirus Replication Organelles Captured by Whole-Cell Electron Microscopy	**75**
CHAPTER 5	The Origin, Dynamic Morphology, and PI4P-Independent Formation of Encephalomyocarditis Virus Replication Organelles	**93**
CHAPTER 6	General Discussion	**115**
	Samenvatting	**126**
	Curriculum Vitae	**128**
	Publications	**128**
	Frequently used abbreviations	**129**

CHAPTER 1

GENERAL INTRODUCTION AND THESIS OUTLINE

Charlotte E. Melia[1,2]

[1]Department of Cell and Chemical biology, Section Electron Microscopy, Leiden University Medical Center, 2300 RC Leiden, The Netherlands.

[2]Sir William Dunn School of Pathology, University of Oxford, Oxford, OX1 3RE, United Kingdom.

PICORNAVIRUSES

The consequences of infection

The picornaviruses are a large family of positive-sense RNA viruses (+RNA viruses), responsible for a diverse range of pathologies in animals and humans. Perhaps the most infamous picornavirus is poliovirus, a member of the enterovirus genus and causative agent of poliomyelitis. Pictorial evidence of the disease is believed to date as far back as 2000 BCE, etched into an Egyptian stele (3) (Figure 1), suggesting that the virus has circulated in human populations for many thousands of years. Fortunately, extensive immunisation campaigns have seen a dramatic reduction in polio cases in more recent decades. This success has been in large part thanks to the development of the oral polio vaccine (OPV) which confers intestinal immunity, inhibiting viral multiplication in subsequent infections and limiting the risk of person-to-person spread (4). Nonetheless, efforts to eradicate poliovirus have met with resistance in some areas, where regional conflicts obstruct the distribution of vaccines, and poverty, overcrowding and poor sanitation contribute to viral spread (5). These challenges are further compounded by the reversion of OPV to virulence, which can stimulate new outbreaks in partially vaccinated populations (6).



Figure 1. Putative evidence for early poliovirus.
Egyptian stele depicting a man with an atrophied right leg, thought to represent a victim of poliomyelitis (circa 2000 BCE). Source: Wikimedia commons.

The success story of poliovirus is a relatively isolated case, as the development and deployment of antiviral drugs and vaccines for other enteroviruses is largely wanting. The task of developing vaccines against some picornaviruses is complicated by the number of viral serotypes in circulation; for instance, rhinovirus serotypes number in the hundreds (7), while for poliovirus only three serotypes are known. Vaccines to counter enterovirus EV-A71, a type of enterovirus A and causative agent of hand foot and mouth disease, are available in China (8). However, strategies to prevent or treat countless other enteroviruses, including the coxsackie A and B viruses, which can cause acute febrile illness, meningitis, encephalitis and myocarditis in young children, remain to be developed. The challenge of managing outbreaks where vaccines or treatments are not available is exemplified by the 2014 epidemic of EV-D68, an enterovirus capable of causing major respiratory illness, which developed across the United States, and spread as far as Canada, Europe and Asia (9) (10). Antiviral strategies to tackle cardioviruses, another genus of picornaviridae, are also limited. Diseases resulting from encephalomyocarditis virus (EMCV) infection are largely limited to swine, manifesting as acute focal myocarditis and sudden death, or reproductive failure in pregnant sows (11, 12). The recently discovered Saffold virus is more closely related to Theiler's murine encephalitis virus (TMEV), which can cause chronic demyelination in the mice it infects (13). Saffold virus has

been linked to disease in humans, and has been found predominantly as a co-infection with other viruses. As such the diseases caused by Saffold virus are difficult to untangle, but it may cause or contribute to pathologies as varied as non-polio acute flaccid paralysis, encephalitis, myocarditis and meningitis.

Picornavirus replication

Picornaviruses utilise receptor-mediated endocytosis as a general mechanism for internalisation into cells (14), representing the first step in the viral life-cycle (Figure 2). The viral genome is then released from its capsid and must cross the endocytic membrane to enter the cell cytosol. While the mechanism underlying this process remains unclear, genome release may be mediated by the VP4 capsid protein multimerising to form a pore within the endocytic membrane (15). Like all +RNA viral genomes, picornavirus genomic RNA, which resembles cellular mRNA, can be directly translated by host-cell ribosomes once within the cell. In the absence of a 5'cap, picornavirus genomes include an internal ribosome entry site (IRES) to facilitate translation. The single polyprotein produced during translation is subsequently cleaved by viral proteases into a handful of viral proteins and stable precursors, while the maturation of some capsid proteins (i.e. VP0)

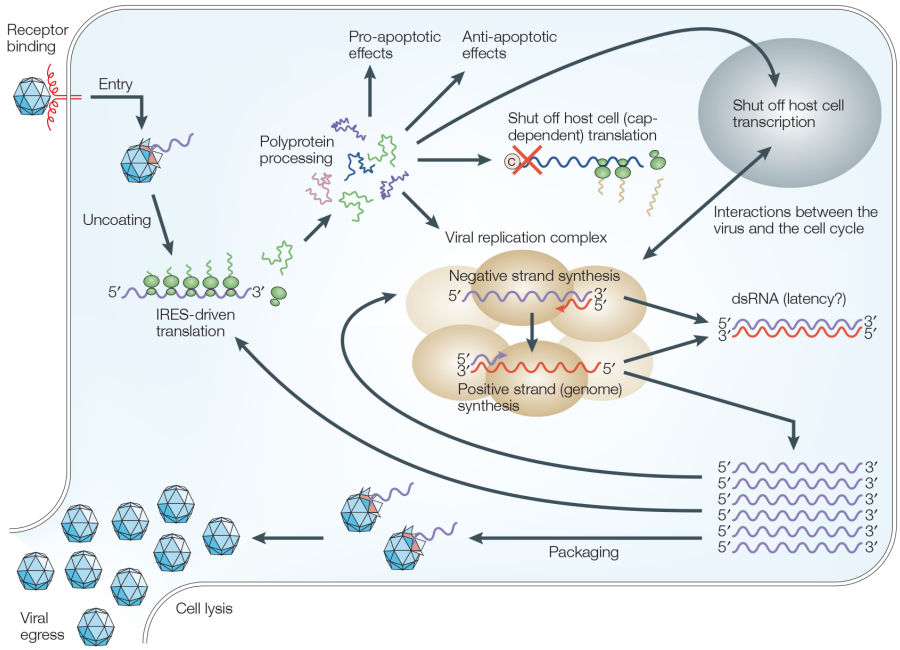


Figure 2. Model of the picornavirus life cycle.

(1) A virus particle enters the cell via receptor-mediated endocytosis. (2) The viral genome passes through a pore in the capsid and endocytic membrane to enter the cell cytosol. (3) The positive-sense single-stranded genome is directly translated into a viral polyprotein, which is cleaved into structural and non-structural proteins. These proteins serve numerous functions, including the shut-off of host transcription and translation. (4) Positive and negative strand viral RNA are replicated on a membrane platform (ROs). (5) Newly synthesised positive-strand RNA is packaged into nascent virions. These virions may reside in the cytosol, or be enwrapped by double-membrane vesicles (DMVs) (6) Viral particles exit the cell, either via fusion of virion containing-DMVs with the plasma membrane or as a result of cell lysis. Reproduced with permission from (2).

occurs by autocatalysis (16, 17). The primary role of the four structural proteins (VP1-VP4) that result from these events is to form the icosahedral viral capsid, which houses a newly synthesized copy of the viral genome. Conversely, the non-structural proteins, which include 2A-C, 3A-D and in some genera (e.g. aphthoviruses and cardioviruses (18, 19)) the leader protein, have a remarkably broad range of activities. Several important processes are mediated by the 2A (or aphthovirus leader) and 3C proteases, which facilitate self-cleavage within the viral polyprotein and subsequent cis-cleavages of precursor proteins, but are also responsible for the cleavage of host proteins. Cellular innate immune sensors, like MDA5 and PKR, are cleaved by 2A and 3C proteases during infection to limit a type I interferon-mediated innate immune response (20). Cleavage of eIF4G by the 2A protease, which is important for (cap-dependent) cellular mRNA translation, results in the shut-down of host protein production (21, 22). While lacking obvious protease activity, the cardiovirus leader protein is also able to contribute to host translational shut-off (23). A critical step during infection, viral RNA synthesis, is mediated by the viral 3D RNA-dependent RNA polymerase, but supported by many of the other non-structural proteins and precursors, including 2C, 3AB, 3B and 3CD (24). The viral 3B protein, or viral protein genome-linked (VPg), associates with the 5'end of the genome and acts as a primer for synthesis first of negative-sense viral RNA, which in turn serves as a template for positive-sense RNA synthesis. The 2BC and 3A proteins also contribute to another intriguing process during replication; the induction of endomembrane rearrangements (25). Genome replication in all eukaryote-infecting +RNA viruses occurs in conjunction with cellular endomembranes, whose compositions are necessarily modified by the accumulation of factors required for viral RNA synthesis. These changes are accompanied by striking alternations to the membrane morphology, resulting in novel membrane architectures that are believed to provide dedicated platforms for efficient viral RNA replication. For this reason, these structures can be referred to as viral 'replication organelles' (ROs).

THE REPLICATION ORGANELLES OF POSITIVE-SENSE RNA VIRUSES

A spectrum of replication organelle morphologies

While the formation of ROs is highly conserved amongst +RNA viruses, the endomembranes targeted and resulting RO morphologies are diverse. Different viruses have been found to generate complex and unique membrane rearrangements, but the archetypal morphologies produced are often categorised into two forms, spherules and double-membrane vesicle (DMVs), as all +RNA viruses characterised to date have been shown to induce either one of these morphologies. Spherules are produced via the invagination of otherwise recognisable host endomembranes like the ER, mitochondria or endolysosomes, to produce small membrane pockets that remain connected to the cytosol. These structures are formed by a number of viruses, including many members of the flavivirus family, like Zika virus and dengue virus (26, 27), as well as togaviruses and nodaviruses (28-31). For many DMV-inducing viruses, the evidence thus far suggests that ER membranes are predominantly utilised for RO biogenesis. DMVs are produced by many members of the order Nidoviridae, including the SARS- and MERS-coronaviruses and equine arteritis virus (32-34) and HCV (35). While the origins of enterovirus replication organelles are unclear, their morphologies, like those of other picornaviruses, include both single- and double-membrane structures (1, 36-38).

Secondary functions of replication organelles

Although supporting RNA synthesis is likely their primary function, additional roles have been ascribed to or hypothesised for ROs, which may confer distinct advantages during replication. ROs could act as replication hubs in the cell, by compartmentalising or segregating viral products and processes. Concentrating viral factors within ROs may serve to increase the efficacy of processes like viral RNA synthesis, but could also facilitate the coupling of ostensibly different processes, like genome synthesis and genome encapsidation, as has been suggested for enteroviruses (39, 40). Whether enterovirus RNA synthesis and viral translation are coupled or segregated remains uncertain. While both processes are essential for successful infection, translation itself precludes viral RNA synthesis (41), and thus, the timing and balance of both processes must be carefully controlled. Another proposed role of ROs is to segregate viral replication intermediates from sensors of the host innate immune system. These cellular sensors, like RIG-I and MDA-5 present in the cytosol, recognise viral dsRNA and trigger the production of type 1 interferons, thus promoting an antiviral state in infected and neighbouring cells (42-45). For viruses that induce invaginated spherules there is strong evidence to suggest that vRNA replication occurs within the spherule lumen, well separated from the remainder of the cytosol (31). Thus, the notion that spherules can shield dsRNA from cellular sensors is largely intuitive. For viruses that induce the formation of replication membranes with a DMV morphology the site of replication is less clear. While replication could also occur within the DMVs, the interior of DMVs often appears to be closed to the remaining cytosol. vRNA replication the DMV interior would be limited, and any replication products would be effectively trapped within the DMV. If replication happens instead on the DMV surface then, with regard to innate immune evasion, the topology of DMVs is less favourable than that of spherules, as cytosol-facing positive-curvature vesicles offers no physical barrier to cytosolic proteins.

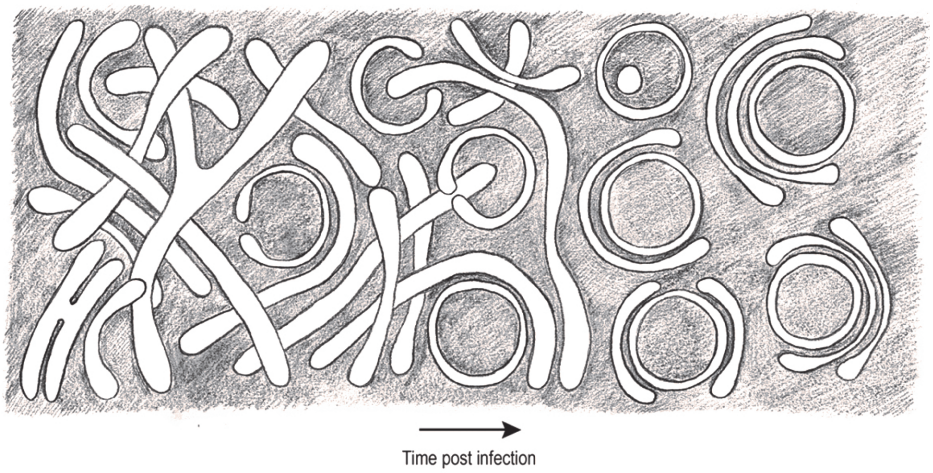


Figure 3. The transforming morphologies of picornavirus replication organelles. At early replication stages the viral replication complex associates with cellular membranes, like the Golgi apparatus (pictured), upon which viral RNA replication occurs. Replication organelles with archetypal morphologies, including single-membrane vesicles and tubules, are generated from these cellular endomembranes. Over the course of infection single-membrane structures have been found to transform form double-membrane vesicles, which may be further enwrapped to form multi-lamellar vesicles. Reproduced with permission from (1).

Nevertheless, DMVs that form later in infection could serve to enclose and protect excess dsRNA or stalled replication complexes from cytosolic sensors.

A FOCUS ON PICORNAVIRUS REPLICATION ORGANELLES

The dual morphologies of picornavirus replication organelles

Picornavirus replication organelles are an unusual case. Enteroviruses, the best-studied genus of *picornaviridae*, have been found to produce ROs with a two-phase morphology. Early in infection clusters of single-membrane tubules (SMTs) are found, interspersed with DMVs. Despite an abundance of suggestive data, the ultimate origin of these structures remains contentious (46). SMTs appear to transform into DMVs over the course of infection via membrane pairing, bending and enwrapping (1, 36) (Figure 3). These studies made use of electron tomography, highlighting the power of this 3D electron microscopy approach for the characterisation of RO membrane topologies, but also the importance of monitoring potentially dynamic structures throughout the infectious cycle. Our understanding of RO morphology in other picornavirus genera, like aphthoviruses and cardioviruses, is based on more limited thin-section electron microscopy analyses. Studies of EMCV infection ultrastructure thus far have reported vesicle clusters (47, 48) or vesicle clusters accompanied by DMVs (38). Similar structures are induced by the aphthovirus foot-and-mouth disease virus (FMDV), where single-membrane structures interspersed with occasional double-membrane structures have been reported (37). While these structures could closely reflect the RO morphologies formed in enterovirus infection, confirmation of an equivalent 3D RO architecture is lacking. Moreover, in the absence of in-depth time courses analyses, or reported intermediate structures, it remains unclear whether the transition from SMTs to DMVs characteristic of enterovirus infection is more broadly conserved amongst picornaviruses.

The origin of picornavirus replication organelles

Minimal systems to induce the formation of ROs based on the expression of a subset of viral proteins have been successfully applied across many virus families, for example, coronaviruses, arteriviruses and HCV (49-52). While this approach has yet to be applied to other picornaviruses, expression of the enterovirus 2BC and 3A proteins in cells was found to be sufficient to generate structures that, in 2D EM cell-sections, are morphologically similar to ROs found in infection (53).

Determining a membrane donor for picornavirus replication organelles has proven more challenging. For cardioviruses the available evidence is limited, but co-localisation between viral protein markers and the ER marker calreticulin suggests that the ER is the RO membrane donor (54). For enteroviruses the available data is more extensive, but is at times conflicting. In different studies the subcellular location of early vRNA synthesis, which could feasibly correspond to RO progenitor membranes, has been linked either to membranes of the ER (55) or the Golgi apparatus (56). Other indications of enterovirus RO origin have been derived from associations between viral and host proteins. One line of evidence suggests that autophagy-derived membranes or components may contribute to RO formation (reviewed in (57)). Other studies point to the involvement of either the ER (56)(58)(59) or Golgi apparatus (58), (46). The 3A protein, when expressed in isolation, has also been found to localise to Golgi membranes (56), while in other cell types or at different time points 3A expression results in Golgi disassembly with 3A ending up at ER exit sites (56, 60). Although

more suggestive than demonstrative, RO formation is also concomitant with Golgi apparatus disassembly during infection (1, 56), a process which could be driven in part by the transformation of Golgi membranes into ROs. Similarly, the host factors GBF1 and PI4KB (described below), essential for enterovirus replication, are Golgi-resident proteins in uninfected cells, which may point to the Golgi as a suitable target organelle for RO formation. Altogether, these studies present a somewhat fragmented array of evidence, and interpreting these data is problematic regardless. Sites of early vRNA synthesis may not necessarily correspond to sites utilised for RO formation, and cellular marker proteins may be actively recruited to novel sites by viral proteins, rendering them poor indicators of host-membrane utilisation. Thus, supporting ultrastructural evidence of the transition from cellular organelle to RO is still ultimately required. While for spherule-inducing viruses and many DMV-inducing viruses, connections between the cellular organelle and RO are readily found, direct connections between a cellular organelle and enterovirus ROs have not been reported. It may be that the transition between host membrane and enterovirus RO is rapid, or that the transition foci are small or rare. While uncertainty remains over the origins of picornavirus ROs, it is likely that the specific endomembranes targeted reflect compositional requirements either for other viral replication processes, or for RO biogenesis itself.

Essential host factors for picornavirus replication

Viruses are obligate intracellular parasites that usurp the host-cell translational machinery and other resources to support their replication. Picornaviruses, and other +RNA viruses, also usurp host endomembranes for the formation of their ROs. Viral RO formation, like viral replication, may also depend upon other host factors that the virus alone cannot provide. Thus far, a number of host factors required for enterovirus infection have been identified that may have a role in RO formation. One of these is reticulon 3, which associates with the viral 2C protein (61). Interestingly, the unrelated spherule-inducing brome mosaic virus (BMV) also recruits reticulons (62) as well as ESCRT proteins (63) for its RO formation. Other key host factors for enterovirus replication include the Golgi-localised protein GBF1, a guanine nucleotide exchange factor for Arf1, which mediates the formation of COP-I coated retrograde transport vesicles (64). GBF1 associates with the viral 3A protein during infection, resulting in its stabilisation on membranes (60)(65). Beyond a potential contribution to the shutdown of the host secretory pathway, the role of GBF1 in infection is unclear. A second Golgi-resident enterovirus host factor is phosphatidylinositol 4-kinase III-beta (PI4KB), which produces the lipid phosphatidylinositol 4-phosphate (PI4P). PI4P appears to influence the efficiency of proteolytic cleavage at specific positions in the enterovirus polyprotein, which could explain its importance during infection (66, 67). This lipid is critical not only for the replication of enteroviruses and other picornaviruses like kobuviruses (68) and cardioviruses (54), but also for the replication of a distantly related flavivirus, hepatitis C virus (HCV) (69). For cardioviruses and HCV, replication is reliant upon PI4P production via the III-beta isoform of PI4K (PI4KA). Intriguingly, a novel role for PI4P has been demonstrated during HCV infection, where it appears to modify the development of HCV replication organelles (70, 71). For enteroviruses and cardioviruses, oxysterol-binding protein (OSBP) is also critical for replication. In uninfected cells OSPB forms ER-Golgi contacts sites that mediate the exchange of cholesterol for PI4P (72). In infected cells, this mechanism appears to be hijacked to transfer cholesterol to PI4P-enriched enterovirus or cardiovirus ROs (54, 73).

METHODS AND APROACHES

Correlative light and electron microscopy

The challenge of understanding rare events within cells is best met through an approach that combines microscopy modalities with complementary advantages and disadvantages. Information about macromolecular complexes in their cellular context is becoming increasingly accessible using cryo-transmission electron microscopy (cryo-TEM), as sensitive detectors, rapid data collection and streamlined image processing have burst the established limits of structure determination by sub-tomogram averaging (74). While cryo-electron tomography (cryo-ET) can also provide unparalleled insights into the ultrastructure of cellular features, it is technically highly demanding. This renders it unsuitable in practice for addressing ultrastructural questions that require extensive sampling of cells and tissues. Room temperature TEM of resin-embedded sections provides a practical imaging solution at the level of cellular ultrastructure, particularly when combined with advanced sample preparation procedures (i.e. high-pressure freezing and freeze substitution) to preserve morphology. While this approach can provide a detailed snapshot of cellular morphology, it cannot be used to monitor processes in cells. For capturing dynamic events, light microscopy is the method of choice. Proteins of interest can now be routinely tagged using genetically-encoded fluorophores, or specific lipids or organelles stained with fluorophores, which can be then be visualised in live cells using fluorescence microscopy (reviewed in (75) and (76)). In this way important cellular or viral processes can be monitored, providing a route to unravel the functions of proteins and structures involved. Correlative light and electron microscopy (CLEM) workflows couple these approaches, wherein features of interest are first imaged by (live-cell) light microscopy and then electron microscopy (77). Cells can be monitored to follow specific processes and then immobilised at a critical moment by chemical fixation or rapid freezing. Foci of interest highlighted by light microscopy can then serve further as a guide to exploring the sample in EM, where structures underlying the fluorescent signal and their surrounding cellular context are revealed.

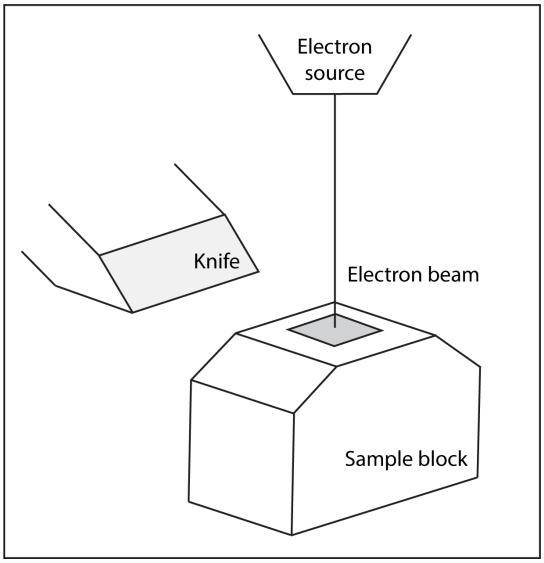


Figure 4. Schematic of Serial block-face Scanning Electron Microscope chamber.

The SEM beam scans across the sample to acquire an image of the surface layer. The knife positioned within the chamber shears the surface layer, removing 25 nm or more. The cycle is repeated until the required sample volume has been consecutively sectioned and imaged in this way. Image stacks are aligned and analysed.

Serial block-face scanning electron microscopy

While CLEM overcomes the hurdle of pinpointing small, rare or transient foci of interest in a dynamic and structure-dense cell, further benefits can be gained by considering the electron microscopy method utilised. Correlating optical sections from light microscopy and the EM sections is challenging, as diffraction-limited light microscopy imaging results in a large z-resolution discrepancy in images from the two modalities. This discrepancy typically necessitates laborious and error-prone serial sectioning to find the most appropriate EM section. Furthermore, thin-section TEM provides only limited contextual information, as each section includes <100 nm of the cell depth. One approach to resolve more information is to use electron tomography, where images of thicker sections are collected at different tilt angles and reconstructed to produce a 3D volume (78). However, electron tomography is unsuitable for imaging very large volumes, as section thickness is limited to a few hundred nanometres.

The alternative to electron tomography is to produce serial thin sections through the entire sample volume for conventional 2D imaging. However, visualizing serial sections is laborious, error-prone and often impractical. To image complete eukaryotic cells or even larger volumes, a number of techniques have recently emerged. Rather than TEM, these approaches utilise scanning electron microscopy (SEM), where a focused electron beam scans the sample surface. One of these approaches, array tomography, involves the collection of ultrathin sections on glass slides or silicon wafers, which can then be repeatedly stained and imaged by LM to gain functional information within large cellular volumes. These sections are subsequently scanned in the SEM to obtain high-resolution ultrastructural information (79). Another approach for volume imaging is focussed ion beam SEM (FIB-SEM). FIB-SEM utilises a secondary beam within the SEM column, typically of gallium ions, to etch away the sample surface and reveal the material below. Etching and imaging can be performed iteratively to gain 3D information about the sample, although this two-step process results in long collection times (80). Another approach is serial block-face SEM (SBF-SEM) (81). For this, samples are prepared and mounted within an SEM chamber that incorporates a diamond knife. Once the sample surface is imaged, the diamond knife slices away a specified thickness to reveal the material beneath, and in this way semi-automated imaging of sample volumes can be iteratively collected to produce stacks of TEM-like images (Figure 4). While the xy resolution is in the nm range (somewhat lower than in TEM), the z-resolution is limited by the minimum sectioning thickness (~25-50 nm), and in all cases a compromise between resolution, field of view and data collection time must be reached. Nonetheless, SBF-SEM provides more complete contextual information than thin section TEM imaging, eliminating the need for extensive serial sectioning for CLEM.

THESIS OUTLINE

This thesis addresses several open questions regarding enterovirus ROs, including the host factor requirements for their formation, their potential functions, and the on-going uncertainty surrounding their origin. It extends our detailed understanding of enterovirus ROs to a second picornavirus genus, the cardioviruses, with broader ramifications for the development of antiviral strategies. The resulting data highlight an unexpected degree of flexibility in the use of membranes

for vRNA synthesis, asking for a re-examination of how we define the ROs of +RNA viruses. Many studies utilise fluorescent markers as a means of assessing co-localisations or the sub-cellular location of a protein of interest. However, the majority of genetically encoded fluorescent tags require large insertions, which may disrupt functions of the target protein. This is particularly problematic for small multifunctional proteins, like those of the picornaviruses.

Chapter 2 explores the generation and applications of a genetically-tagged enterovirus, which utilises a split-GFP approach. This system was used to monitor RO formation concomitant with Golgi apparatus disassembly during infection by live-cell confocal microscopy, and to visualise the accumulation of the 3A protein at ROs using CLEM. This latter application was utilised in **Chapter 3**, which examines the functions of PI4P in enterovirus replication. By exploiting a mutant coxsackievirus capable of replication under PI4KB inhibition, we explore the effects of low PI4P conditions on RO formation. Using a range of approaches including TEM, CLEM and autoradiography, a role for PI4P in expediting RO formation was established. The intriguing ability of this virus to replicate extensively in the absence of ROs was further exploited to investigate the functions of enterovirus ROs, the results of which cast doubt on the notion that enterovirus ROs are essential for innate immune evasion.

In **Chapter 2** and **Chapter 3**, tantalising hints regarding the origin of enterovirus ROs were uncovered. Accumulation of the 3A protein at the Golgi apparatus was found to result in rapid Golgi disintegration and, under low PI4P conditions that slow RO formation, substantial vRNA synthesis occurred at a morphologically intact Golgi apparatus. While these data support the hypothesis that enterovirus ROs are derived from Golgi membranes, in **Chapter 4** this possibility is addressed directly by visualising nascent ROs. Using the split-GFP system, we pinpoint the early phase of RO formation in live cells for CLEM. Given that RO biogenesis may occur at small foci, CLEM was coupled to SBF-SEM to ensure the whole-cell volume was captured. Remarkably, membrane continuities were found between both ER and trans-Golgi network and ROs, suggesting that both organelles are capable of supporting RO biogenesis, and uniting seemingly conflicting hypotheses regarding the origin of enterovirus ROs. SBF-SEM data were probed further, revealing more about the cellular context at this time point, and later in infection.

To date, our understanding of ROs in picornaviruses other than enteroviruses is based upon evaluations of 2D EM cell-sections. In **Chapter 5** we pursue an in-depth investigation of cardiovirus ROs, using electron tomography to probe the 3D morphology across a range of infection time points. This investigation reveals striking morphological similarities and differences in the origin of cardiovirus and enterovirus ROs. Furthermore, we found that any role for PI4P in cardiovirus replication, including RO formation, can be bypassed. These data highlight important similarities between the ROs of these closely related viruses, which may well constitute hallmarks of picornavirus infection.

Chapter 6 discusses the broader context and implications of the previous chapters, and draws together key findings that highlight emerging themes in +RNA virus research.

REFERENCES

1. Limpens RWAL, van der Schaar HM, Kumar D, Koster AJ, Snijder EJ, van Kuppeveld FJM, Barcena M. 2011. The Transformation of Enterovirus Replication Structures: a Three-Dimensional Study of Single- and Double-Membrane Compartments. mBio 2.
2. Whitton JL, Cornell CT, Feuer R. 2005. Host and virus determinants of picornavirus pathogenesis and tropism. Nat Rev Microbiol 3:765-76.
3. Galassi FM, Habicht ME, Ruhli FJ. 2017. Poliomyelitis in Ancient Egypt? Neurological Sciences 38:375-375.
4. Ghendon Y, Robertson SE. 1994. Interrupting the Transmission of Wild Polioviruses with Vaccines - Immunological Considerations. Bulletin of the World Health Organization 72:973-983.
5. Nnadi C, Etsano A, Uba B, Ohuabunwo C, Melton M, Nganda GW, Esapa L, Bolu O, Mahoney F, Vertefeuille J, Wiesen E, Durry E. 2017. Approaches to Vaccination Among Populations in Areas of Conflict. Journal of Infectious Diseases 216:S368-S372.
6. Parker EPK, Grassly NC. 2016. Polio vaccination: preparing for a change of routine. Lancet 388:107-108.
7. McLean GR. 2014. Developing a vaccine for human rhinoviruses. J Vaccines Immun 2:16-20.
8. Mao QY, Wang YP, Bian LL, Xu M, Liang ZL. 2016. EV71 vaccine, a new tool to control outbreaks of hand, foot and mouth disease (HFMD). Expert Review of Vaccines 15:599-606.
9. Midgley CM, Watson JT, Nix WA, Curns AT, Rogers SL, Brown BA, Conover C, Dominguez SR, Feikin DR, Gray S, Hassan F, Hoferka S, Jackson MA, Johnson D, Leshem E, Miller L, Nichols JB, Nyquist AC, Obringer E, Patel A, Patel M, Rho B, Schneider E, Schuster JE, Selvarangan R, Seward JF, Turabelidze G, Oberste MS, Pallansch MA, Gerber S, Grp E-DW. 2015. Severe respiratory illness associated with a nationwide outbreak of enterovirus D68 in the USA (2014): a descriptive epidemiological investigation. Lancet Respiratory Medicine 3:879-887.
10. Holm-Hansen CC, Midgley SE, Fischer TK. 2016. Global emergence of enterovirus D68: a systematic review. Lancet Infectious Diseases 16:E64-E75.
11. Carocci M, Bakkali-Kassimi L. 2012. The encephalomyocarditis virus. Virulence 3:351-367.
12. Koenen F, Vanderhallen H, Castryck F, Miry C. 1999. Epidemiologic, pathogenic and molecular analysis of recent encephalomyocarditis outbreaks in Belgium. Journal of Veterinary Medicine Series B-Infectious Diseases and Veterinary Public Health 46:217-231.
13. Lipton HL. 1975. Theilers Virus-Infection in Mice - Unusual Biphasic Disease Process Leading to Demyelination. Infection and Immunity 11:1147-1155.
14. Tuthill TJ, Groppelli E, Hogle JM, Rowlands DJ. 2010. Picornaviruses. Cell Entry by Non-Enveloped Viruses 343:43-89.
15. Panjwani A, Strauss M, Gold S, Wenham H, Jackson T, Chou JJ, Rowlands DJ, Stonehouse NJ, Hogle JM, Tuthill TJ. 2014. Capsid protein VP4 of human rhinovirus induces membrane permeability by the formation of a size-selective multimeric pore. PLoS Pathog 10:e1004294.

16. Pallansch MA, Kew OM, Semler BL, Omilianowski DR, Anderson CW, Wimmer E, Rueckert RR. 1984. Protein processing map of poliovirus. J Virol 49:873-80.
17. Arnold E, Luo M, Vriend G, Rossmann MG, Palmenberg AC, Parks GD, Nicklin MJ, Wimmer E. 1987. Implications of the picornavirus capsid structure for polyprotein processing. Proc Natl Acad Sci U S A 84:21-5.
18. Liu Y, Zhu Z, Zhang M, Zheng H. 2015. Multifunctional roles of leader protein of foot-and-mouth disease viruses in suppressing host antiviral responses. Vet Res 46:127.
19. Paul S, Michiels T. 2006. Cardiovirus leader proteins are functionally interchangeable and have evolved to adapt to virus replication fitness. Journal of General Virology 87:1237-1246.
20. Dotzauer A, Kraemer L. 2012. Innate and adaptive immune responses against picornaviruses and their counteractions: An overview. World J Virol 1:91-107.
21. Novoa I, Carrasco L. 1999. Cleavage of eukaryotic translation initiation factor 4G by exogenously added hybrid proteins containing poliovirus 2A(pro) in HeLa cells: Effects on gene expression. Molecular and Cellular Biology 19:2445-2454.
22. Glaser W, Skern T. 2000. Extremely efficient cleavage of eIF4G by picornaviral proteinases L and 2A in vitro. FEBS Lett 480:151-5.
23. Zoll J, Galama JMD, vanKuppeveld FJM, Melchers WJG. 1996. Mengovirus leader is involved in the inhibition of host cell protein synthesis. Journal of Virology 70:4948-4952.
24. Lin JY, Chen TC, Weng KF, Chang SC, Chen LL, Shih SR. 2009. Viral and host proteins involved in picornavirus life cycle. J Biomed Sci 16:103.
25. Suhy DA, Giddings TH, Kirkegaard K. 2000. Remodeling the endoplasmic reticulum by poliovirus infection and by individual viral proteins: an autophagy-like origin for virus-induced vesicles. Journal of Virology 74:8953-8965.
26. Cortese M, Goellner S, Acosta EG, Neufeldt CJ, Oleksiuk O, Lampe M, Haselmann U, Funaya C, Schieber N, Ronchi P, Schorb M, Pruunsild P, Schwab Y, Chatel-Chaix L, Ruggieri A, Bartenschlager R. 2017. Ultrastructural Characterization of Zika Virus Replication Factories. Cell Reports 18:2113-2123.
27. Welsch S, Miller S, Romero-Brey I, Merz A, Bleck CKE, Walther P, Fuller SD, Antony C, Krijnse-Locker J, Bartenschlager R. 2009. Composition and Three-Dimensional Architecture of the Dengue Virus Replication and Assembly Sites. Cell Host & Microbe 5:365-375.
28. Grimley PM, Berezesky IK, Friedman RM. 1968. Cytoplasmic Structures Associated with an Arbovirus Infection - Loci of Viral Ribonucleic Acid Synthesis. Journal of Virology 2:1326-+.
29. Kujala P, Ahola T, Ehsani N, Avuinen P, Vihinen H, Kaariainen L. 1999. Intracellular distribution of rubella virus nonstructural protein P150. Journal of Virology 73:7805-7811.
30. Short JR, Speir JA, Gopal R, Pankratz LM, Lanman J, Schneemann A. 2016. Role of Mitochondrial Membrane Spherules in Flock House Virus Replication. Journal of Virology 90:3676-3683.
31. Kopek BG, Perkins G, Miller DJ, Ellisman MH, Ahlquist P. 2007. Three-dimensional analysis of a viral RNA replication complex reveals a virus-induced mini-organelle. Plos Biology 5:2022-2034.
32. Knoops K, Kikkert M, van den Worm SHE, Zevenhoven-Dobbe JC, van der Meer Y, Koster AJ, Mommaas AM, Snijder EJ. 2008. SARS-coronavirus replication is supported by a reticulovesicular network of modified endoplasmic reticulum. Plos Biology 6:1957-1974.

33. de Wilde AH, Raj VS, Oudshoorn D, Bestebroer TM, van Nieuwkoop S, Limpens RWAL, Posthuma CC, van der Meer Y, Barcena M, Haagmans BL, Snijder EJ, van den Hoogen BG. 2013. MERS-coronavirus replication induces severe in vitro cytopathology and is strongly inhibited by cyclosporin A or interferon-alpha treatment. Journal of General Virology 94:1749-1760.
34. Knoops K, Barcena M, Limpens RW, Koster AJ, Mommaas AM, Snijder EJ. 2012. Ultrastructural characterization of arterivirus replication structures: reshaping the endoplasmic reticulum to accommodate viral RNA synthesis. J Virol 86:2474-87.
35. Romero-Brey I, Merz A, Chiramel A, Lee JY, Chlanda P, Haselman U, Santarella-Mellwig R, Habermann A, Hoppe S, Kallis S, Walther P, Antony C, Krijnse-Locker J, Bartenschlager R. 2012. Three-Dimensional Architecture and Biogenesis of Membrane Structures Associated with Hepatitis C Virus Replication. Plos Pathogens 8.
36. Belov GA, Nair V, Hansen BT, Hoyt FH, Fischer ER, Ehrenfeld E. 2012. Complex Dynamic Development of Poliovirus Membranous Replication Complexes. Journal of Virology 86:302-312.
37. Monaghan P, Cook H, Jackson T, Ryan M, Wileman T. 2004. The ultrastructure of the developing replication site in foot-and-mouth disease virus-infected BHK-38 cells. J Gen Virol 85:933-46.
38. Amako K, Dales S. 1967. Cytopathology of Mengovirus infection. II. Proliferation of membranous cisternae. Virology 32:201-15.
39. Nugent CI, Johnson KL, Sarnow P, Kirkegaard K. 1999. Functional coupling between replication and packaging of poliovirus replicon RNA. Journal of Virology 73:427-435.
40. Liu Y, Wang CL, Mueller S, Paul AV, Wimmer E, Jiang P. 2010. Direct Interaction between Two Viral Proteins, the Nonstructural Protein 2C(ATPase) and the Capsid Protein VP3, Is Required for Enterovirus Morphogenesis. Plos Pathogens 6.
41. Gamarnik AV, Andino R. 1998. Switch from translation to RNA replication in a positive-stranded RNA virus. Genes Dev 12:2293-304.
42. Hensley LE, Fritz EA, Jahrling PB, Karp CL, Huggins JW, Geisbert TW. 2004. Interferon-beta 1a and SARS coronavirus replication. Emerging Infectious Diseases 10:317-319.
43. Liu ML, Lee YP, Wang YF, Lei HY, Liu CC, Wang SM, Su IJ, Wang JR, Yeh TM, Chen SH, Yu CK. 2005. Type I interferons protect mice against enterovirus 71 infection. Journal of General Virology 86:3263-3269.
44. Yu GY, He GB, Li CY, Tang M, Grivennikov S, Tsai WT, Wu MS, Hsu CW, Tsai Y, Wang LHC, Karin M. 2012. Hepatic Expression of HCV RNA-Dependent RNA Polymerase Triggers Innate Immune Signaling and Cytokine Production. Molecular Cell 48:313-321.
45. Nikonov A, Molder T, Sikut R, Kiiver K, Mannik A, Toots U, Lulla A, Lulla V, Utt A, Merits A, Ustav M. 2013. RIG-I and MDA-5 Detection of Viral RNA-dependent RNA Polymerase Activity Restricts Positive-Strand RNA Virus Replication. Plos Pathogens 9.
46. Richards AL, Soares-Martins JAP, Riddell GT, Jackson WT. 2014. Generation of Unique Poliovirus RNA Replication Organelles. Mbio 5.
47. Masek-Hammerman K, Miller AD, Lin KC, MacKey J, Weissenbock H, Gierbolini L, Burgos A, Perez H, Mansfield KG. 2012. Epizootic Myocarditis Associated With Encephalomyocarditis Virus in a Group of Rhesus Macaques (Macaca mulatta). Veterinary Pathology 49:386-392.

48. Dales S, Franklin RM. 1962. A comparison of the changes in fine structure of L cells during single cycles of viral multiplication, following their infection with the viruses of Mengo and encephalomyocarditis. J Cell Biol 14:281-302.
49. Oudshoorn D, Rijs K, Limpens R, Groen K, Koster AJ, Snijder EJ, Kikkert M, Barcena M. 2017. Expression and Cleavage of Middle East Respiratory Syndrome Coronavirus nsp3-4 Polyprotein Induce the Formation of Double-Membrane Vesicles That Mimic Those Associated with Coronaviral RNA Replication. MBio 8.
50. Angelini MM, Akhlaghpour M, Neuman BW, Buchmeier MJ. 2013. Severe acute respiratory syndrome coronavirus nonstructural proteins 3, 4, and 6 induce double-membrane vesicles. MBio 4.
51. Snijder EJ, van Tol H, Roos N, Pedersen KW. 2001. Non-structural proteins 2 and 3 interact to modify host cell membranes during the formation of the arterivirus replication complex. J Gen Virol 82:985-94.
52. Romero-Brey I, Berger C, Kallis S, Kolovou A, Paul D, Lohmann V, Bartenschlager R. 2015. NS5A Domain 1 and Polyprotein Cleavage Kinetics Are Critical for Induction of Double-Membrane Vesicles Associated with Hepatitis C Virus Replication. MBio 6:e00759.
53. Suhy DA, Giddings TH, Jr., Kirkegaard K. 2000. Remodeling the endoplasmic reticulum by poliovirus infection and by individual viral proteins: an autophagy-like origin for virus-induced vesicles. J Virol 74:8953-65.
54. Dorobantu CM, Albulescu L, Harak C, Feng Q, van Kampen M, Strating JRPM, Gorbalenya AE, Lohmann V, van der Schaar HM, van Kuppeveld FJM. 2015. Modulation of the Host Lipid Landscape to Promote RNA Virus Replication: The Picornavirus Encephalomyocarditis Virus Converges on the Pathway Used by Hepatitis C Virus. Plos Pathogens 11.
55. Bienz K, Egger D, Pasamontes L. 1987. Association of Polioviral Proteins of the P2-Genomic Region with the Viral Replication Complex and Virus-Induced Membrane Synthesis as Visualized by Electron-Microscopic Immunocytochemistry and Autoradiography. Virology 160:220-226.
56. Hsu NY, Ilnytska O, Belov G, Santiana M, Chen YH, Takvorian PM, Pau C, van der Schaar H, Kaushik-Basu N, Balla T, Cameron CE, Ehrenfeld E, van Kuppeveld FJM, Altan-Bonnet N. 2010. Viral Reorganization of the Secretory Pathway Generates Distinct Organelles for RNA Replication. Cell 141:799-811.
57. Lai JKF, Sam IC, Chan YF. 2016. The Autophagic Machinery in Enterovirus Infection. Viruses-Basel 8.
58. Schlegel A, Giddings TH, Jr., Ladinsky MS, Kirkegaard K. 1996. Cellular origin and ultrastructure of membranes induced during poliovirus infection. J Virol 70:6576-88.
59. Rust RC, Landmann L, Gosert R, Tang BL, Hong WJ, Hauri HP, Egger D, Bienz K. 2001. Cellular COPII proteins are involved in production of the vesicles that form the poliovirus replication complex. Journal of Virology 75:9808-9818.
60. Wessels E, Duijsings D, Niu TK, Neumann S, Oorschot VM, de Lange F, Lanke KHW, Klumperman J, Henke A, Jackson CL, Melchers WJG, van Kuppeveld FJM. 2006. A viral protein that blocks Arf1-mediated COP-I assembly by inhibiting the guanine nucleotide exchange factor GBF1. Developmental Cell 11:191-201.
61. Tang WF, Yang SY, Wu BW, Jheng JR, Chen YL, Shih CH, Lin KH, Lai HC, Tang P, Horng JT.

2007. Reticulon 3 binds the 2C protein of enterovirus 71 and is required for viral replication. Journal of Biological Chemistry 282:5888-5898.

62 Diaz A, Wang XF, Ahlquist P. 2010. Membrane-shaping host reticulon proteins play crucial roles in viral RNA replication compartment formation and function. Proceedings of the National Academy of Sciences of the United States of America 107:16291-16296.

63. Diaz A, Zhang JT, Ollwerther A, Wang XF, Ahlquist P. 2015. Host ESCRT Proteins Are Required for Bromovirus RNA Replication Compartment Assembly and Function. Plos Pathogens 11.

64.. Lanke KHW, van der Schaar HM, Belov GA, Feng Q, Duijsings D, Jackson CL, Ehrenfeld E, van Kuppeveld FJM. 2009. GBF1, a Guanine Nucleotide Exchange Factor for Arf, Is Crucial for Coxsackievirus B3 RNA Replication. Journal of Virology 83:11940-11949.

65. Belov GA, Altan-Bonnet N, Kovtunovych G, Jackson CL, Lippincott-Schwartz J, Ehrenfeld E. 2007. Hijacking components of the cellular secretory pathway for replication of poliovirus RNA. Journal of Virology 81:558-567.

66. Arita M. 2016. Mechanism of Poliovirus Resistance to Host Phosphatidylinositol-4 Kinase III beta Inhibitor. Acs Infectious Diseases 2:140-148.

67. Lyoo H, Dorobantu CM, van der Schaar HM, van Kuppeveld FJM. 2017. Modulation of proteolytic polyprotein processing by coxsackievirus mutants resistant to inhibitors targeting phosphatidylinositol-4-kinase IIIbeta or oxysterol binding protein. Antiviral Res 147:86-90.

68. Ishikawa-Sasaki K, Sasaki J, Taniguchi K. 2014. A Complex Comprising Phosphatidylinositol 4-Kinase III beta, ACBD3, and Aichi Virus Proteins Enhances Phosphatidylinositol 4-Phosphate Synthesis and Is Critical for Formation of the Viral Replication Complex. Journal of Virology 88:6586-6598.

69. Berger KL, Kelly SM, Jordan TX, Tartell MA, Randall G. 2011. Hepatitis C Virus Stimulates the Phosphatidylinositol 4-Kinase III Alpha-Dependent Phosphatidylinositol 4-Phosphate Production That Is Essential for Its Replication. Journal of Virology 85:8870-8883.

70. Reiss S, Harak C, Romero-Brey I, Radujkovic D, Klein R, Ruggieri A, Rebhan I, Bartenschlager R, Lohmann V. 2013. The lipid kinase phosphatidylinositol-4 kinase III alpha regulates the phosphorylation status of hepatitis C virus NS5A. PLoS Pathog 9:e1003359.

71. Reghellin V, Donnici L, Fenu S, Berno V, Calabrese V, Pagani M, Abrignani S, Peri F, De Francesco R, Neddermann P. 2014. NS5A inhibitors impair NS5A-phosphatidylinositol 4-kinase IIIalpha complex formation and cause a decrease of phosphatidylinositol 4-phosphate and cholesterol levels in hepatitis C virus-associated membranes. Antimicrob Agents Chemother 58:7128-40.

72. Mesmin B, Bigay J, Moser von Filseck J, Lacas-Gervais S, Drin G, Antonny B. 2013. A four-step cycle driven by PI(4)P hydrolysis directs sterol/PI(4)P exchange by the ER-Golgi tether OSBP. Cell 155:830-43.

73. Strating JRPM, van der Linden L, Albulescu L, Bigay J, Arita M, Delang L, Leyssen P, van der Schaar HM, Lanke KHW, Thibaut HJ, Ulferts R, Drin G, Schlinck N, Wubbolts RW, Sever N, Head SA, Liu JO, Beachy PA, De Matteis MA, Shair MD, Olkkonen VM, Neyts J,

74. van Kuppeveld FJM. 2015. Itraconazole Inhibits Enterovirus Replication by Targeting the Oxysterol-Binding Protein. Cell Reports 10:600-615.

75. Callaway E. 2015. The revolution will not be crystallized: a new method sweeps through

structural biology. Nature 525:172-4.

Toseland CP. 2013. Fluorescent labeling and modification of proteins. J Chem Biol 6:85-95.

76. Hu F, Liu B. 2016. Organelle-specific bioprobes based on fluorogens with aggregation-induced emission (AIE) characteristics. Organic & Biomolecular Chemistry 14:9931-9944.

77. de Boer P, Hoogenboom JP, Giepmans BNG. 2015. Correlated light and electron microscopy: ultrastructure lights up! Nature Methods 12:503-513.

78. Koster AJ, Grimm R, Typke D, Hegerl R, Stoschek A, Walz J, Baumeister W. 1997. Perspectives of molecular and cellular electron tomography. Journal of Structural Biology 120:276-308.

79. Micheva KD, Smith SJ. 2007. Array tomography: A new tool for Imaging the molecular architecture and ultrastructure of neural circuits. Neuron 55:25-36.

80. Subramaniam S, Zhang PJ, Lefman J, Juliani J, Kessel M. 2003. Electron tomography: a powerful tool for 3D cellular microscopy. Asm News 69:240-+.

81. Peddie CJ, Collinson LM. 2014. Exploring the third dimension: Volume electron microscopy comes of age. Micron 61:9-19.

CHAPTER 2

ILLUMINATING THE SITES OF ENTEROVIRUS REPLICATION IN LIVING CELLS BY USING A SPLIT-GFP-TAGGED VIRAL PROTEIN

H.M. van der Schaar[1,$], C.E. Melia[2,$], J.A.C. van Bruggen[1,*], J.R.P.M. Strating[1], M.E.D. van Geenen[1], A.J. Koster[2], M. Bárcena[2,&] and F.J.M. van Kuppeveld[1,&]

Published in mSphere 2016. 1(4):e00104-16
DOI: 10.1128/mSphere.00104-16

[1] Department of Infectious Diseases & Immunology, Virology Division, Faculty of Veterinary Medicine, Utrecht University, Utrecht, The Netherlands

[2] Department of Molecular Cell Biology, Section Electron Microscopy, Leiden University Medical Center, Leiden, The Netherlands

*Current address: Department of Hematology, Lymphoma and Myeloma Center, Academic Medical Center Amsterdam, University of Amsterdam, Amsterdam, The Netherlands

[$,&]These authors contributed equally

SUMMARY

Like all other positive-strand RNA viruses, enteroviruses generate new organelles ("replication organelles", ROs) with a unique protein and lipid composition on which they multiply their viral genome. Suitable tools for live-cell imaging of enterovirus ROs are currently unavailable, as recombinant enteroviruses that encode RO-anchored viral proteins tagged with fluorescent reporters have to date not been reported. To overcome this limitation, we used a split-GFP system, comprising a large fragment (S1-10) and a small fragment (S11) of only 16 residues. The GFP(S11) fragment was inserted into the 3A protein of the enterovirus coxsackievirus B3 (CVB3), while the large fragment was supplied by transient or stable expression in cells. The introduction of GFP(S11) did not affect the known functions of 3A when expressed in isolation. Using correlative light electron microscopy (CLEM) we showed that GFP fluorescence was detected at ROs, whose morphologies are essentially identical to those previously observed for wild-type CVB3, indicating that GFP(S11)-tagged 3A proteins assemble with GFP(S1-10) to form GFP for illumination of bona fide ROs. It is well established that enterovirus infection leads to Golgi disintegration. Through live-cell imaging of infected cells expressing an mCherry-tagged Golgi marker, we monitored RO development and revealed the dynamics of Golgi disassembly in real time. Having demonstrated the suitability of this virus for imaging ROs, we constructed a CVB3 encoding GFP(S1-10) and GFP(S11)-tagged 3A to bypass the need to express GFP(S1-10) prior to infection. These tools will have multiple applications in future studies on the origin, location, and function of enterovirus ROs.

INTRODUCTION

The Enterovirus genus of the Picornaviridae family comprises many human pathogens, such as poliovirus, coxsackievirus A and B, enterovirus-68, enterovirus-71, and rhinovirus, which can cause a wide spectrum of illnesses (1). Being obligate intracellular parasites, enteroviruses rely on the machineries of their host cell for propagation. Like all other viruses that carry a positive-sense, single-stranded RNA genome, enteroviruses redecorate the cell's interior to form new membranous structures that serve as a platform for viral RNA replication (2–6). These structures may aid in concentrating as well as in conferring the proper topology of all required components for genome replication. Furthermore, it has been suggested that they can shield viral RNA products from degradation by cellular RNAses or from detection by sensors of the innate immune system (7, 8).

The morphology of the enterovirus-induced membrane structures (often termed "replication organelles", ROs) has been a subject of intense investigation. Two-dimensional electron microscopy (EM) studies have shown both single-membrane and double-membrane structures, depending on the cell type, time point, and experimental procedure (9–16). Recently, two studies with poliovirus and coxsackievirus B3 (CVB3) were conducted to reveal the three-dimensional structure of the ROs in the course of infection using electron tomography (17, 18). Both studies showed that the first structures detected upon infection are single-membrane tubular structures. These tubules appear to be formed at the expense of Golgi membranes, since the Golgi is in most cell sections no longer detected when the tubules are present. The tubules emerge during the exponential phase of viral RNA replication, suggesting that they are the pre-eminent structures supporting viral genome

synthesis. Later in infection, the tubular ROs morph into double-membrane vesicles (DMVs) and multilamellar structures, a phenomenon that is reminiscent of autophagy. For poliovius it was shown that newly-synthesized viral RNA localizes not only to the tubular structures, but also to the DMVs, implying that the DMVs may also facilitate genome replication (17). In addition, DMVs have been proposed to mediate non-lytic release of progeny virions (19–21).

While EM analyses have provided insight into the structure of the enterovirus ROs, fluorescence microscopy studies have focused on unraveling their origin by investigating the presence of essential host factors or marker proteins on the ROs. These studies have been performed in cells that had been fixed at various time points post-infection, usually at 1 to 2 hour intervals, which gives limited insight into the dynamics of RO formation. ROs are mostly visualized by immunolabeling using antibodies directed against viral proteins that are anchored in the RO membrane, i.e. 2B, 2C, or 3A. With this approach, ROs were shown to colocalize with several proteins involved in ER-to-Golgi transport (22–25) as well as with LC3, a protein involved in the autophagy pathway (11, 13, 19). However, ROs are not mere remnants of the early secretory pathway or constituents of the autophagy pathway. Instead, enteroviruses seem highly selective in hijacking components from these pathways to create completely new organelles with a unique protein and lipid composition optimized for genome replication (reviewed in (5)).

Although we are learning more and more about the morphology and the origin of enterovirus ROs by three-dimensional EM studies and by fluorescence microscopy of fixed cells, it has not been possible thus far to directly visualize ROs in living cells. Live-cell imaging can provide unprecedented insights into the dynamics of biological processes, including RO formation and viral effects on other cellular structures or organelles, and may capture rare or rapid events that may be missed in the analysis of fixed cells. Moreover, observations by immunolabeling of fixed cells may be compromised by artifacts induced during sample preparation, and should be complemented by live-cell imaging (26). To date, enterovirus ROs have only been monitored indirectly in living cells that expressed a fluorescently labeled cellular protein, the Golgi-resident Arf1-RFP, as an RO marker (22). Yet, the use of a cellular protein as a RO marker may complicate investigations examining the transition from Golgi to early enterovirus ROs. A better strategy for direct visualization of ROs in living cells is to label a viral protein involved in their formation. The enterovirus genome can accept coding sequences of foreign proteins (GFP (27, 28), proLC3 (16), Timer (29), and luciferase (27, 30) among others) at the start of the open-reading frame before the capsid coding region. In addition, a poliovirus encoding a viral proteinase (i.e. the 2A protein) tagged with dsRed was generated (31). However, 2A is not a bona fide RO-marker as it does not localize exclusively to ROs. Attempts to generate enteroviruses that encode fluorescently labeled, membrane-anchored viral proteins to illuminate ROs have thus far been futile, most likely because fusion of a fluorescent protein to an RO-anchored viral protein impaired its function or liberation from the polyprotein. The use of small genetically-encoded tags may overcome this limitation, as evidenced by the successful generation of recombinant polioviruses that encode small epitope tags (such as HA, FLAG, and c-myc) in their 3A protein (32) and a recombinant CVB3 encoding an HA-tag in its 2B protein (33).

In this study, we used a split-GFP system (34) to tag the 3A protein of CVB3, a small protein of 89 amino acids with a C-terminal hydrophobic domain that inserts into the RO membranes (35). This split-GFP system is based on superfolder GFP, a variant of GFP that folds better, matures more rapidly, and fluoresces more brightly than GFP (36). Like GFP, superfolder GFP has a beta barrel structure

consisting of eleven beta-strands, which in this system are split into a large fragment (strands 1-10, S1-10) and a small fragment (S11) of only 16 amino acids. Separately, these two fragments are non-fluorescent. Green fluorescence is emitted only when they assemble into superfolder GFP (34). We show that tagging 3A with GFP(S11) does not affect its known functions when 3A is expressed alone. When introduced into the viral genome of CVB3, GFP(S11)-tagged 3A assembled with GFP(S1-10) to illuminate enterovirus ROs as shown by correlative light electron microscopy (CLEM). We illustrate the suitability of CVB3 encoding this split-GFP-tagged 3A for live-cell imaging by monitoring the development of ROs and the disintegration of the Golgi, as visualized using GM130-mCherry, in infected cells in real time. This new tool simplifies the visualization of enterovirus ROs, avoiding immunolabeling of viral proteins in fixed cells, and will have multiple applications in future studies on the origin, location, and function of enterovirus ROs.

RESULTS

3A tagged with GFP(S11) assembles with GFP(S1-10) to yield GFP fluorescence

In order to visualize the enterovirus ROs in living cells, one of the non-structural proteins that is anchored in the membranes of the ROs should be labeled with a fluorescent tag. A transposon-based insertion mutagenesis study revealed that the N-terminal region of poliovirus 3A tolerates small insertions (32, 37). Specifically, viable insertions were found after residues 2, 6, 9, 10, or 11. Since the 3A proteins of coxsackievirus B3 (CVB3) and poliovirus are highly homologous, these positions were good candidates for introduction of a small tag in CVB3 3A. We chose to insert GFP(S11) after amino acid 2 in CVB3 3A without using any linker residues, yielding 3A(S11aa2) (Fig. 1A).

Before introducing GFP(S11) into the viral genome, we first tested whether inserting the tag into 3A at this position would generate GFP fluorescence upon co-expression with GFP(S1-10). Staining with an anti-3A antibody demonstrated that the expression pattern of 3A(S11aa2) resembled that of untagged 3A (i.e. lacking GFP(S11)) in HeLa (Fig. S1A) and in BGM cells (data not shown), indicating that the GFP(S11)-tag does not alter the localization of 3A. Co-expression of GFP(S1-10) with 3A(S11aa2), but not with untagged 3A, resulted in a GFP signal that greatly overlapped with the 3A-pattern generated with the anti-3A antibody (Fig. S1B, HeLa cells not shown). Furthermore, 3A(S11aa2) was not GFP fluorescent in the absence of GFP(S1-10) (Fig. S1A). Thus, GFP(S1-10) can assemble with 3A(S11aa2) to yield GFP fluorescence at the sites where 3A is localized in the cell.

Introduction of GFP(S11) into 3A does not impair its known functions

Next, we investigated whether 3A(S11aa2) is able to perform the same functions as untagged 3A. Enteroviruses hijack the Golgi-resident PI4KB (phosphatidylinositol 4-kinase III beta) via their 3A protein to ROs to enrich these membranes in PI4P (phosphatidylinositol 4-phosphate), an essential lipid for viral RNA replication (22). In line with previous observations (22, 38, 39), PI4KB was present in a faint Golgi-like pattern in untransfected HeLa cells, whereas in 3A-transfected cells an intese PI4KB signal was detected at membranes containing untagged 3A (Fig. 1B). Likewise, in cells co-expressing 3A(S11aa2) and GFP(S1-10), PI4KB recruitment was observed to the membranes containing fluorescent 3A (Fig. 1B).

The enterovirus 3A protein interacts directly with GBF1, an essential host factor for enterovirus replication (27, 30). Under normal conditions, GBF1 is an activator of the small GTPase Arf1, which

in turn recruits the COP-I complex to Golgi membranes upon activation (40). The COP-I coat initiates budding of transport vesicles that ferry cargo at the ER-Golgi interface and in the Golgi (41). Expression of 3A in isolation leads to the perturbation of ER to Golgi transport (30, 42–44), as

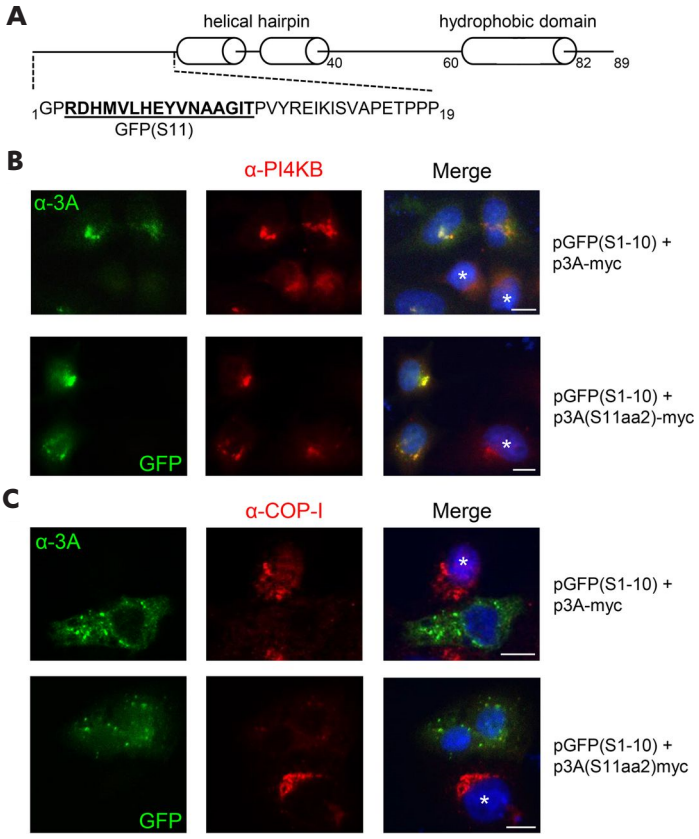


Figure 1. 3A(S11aa2) recruits PI4KB and dissociates COP-I from Golgi membranes. A) The CVB3-3A(S11aa2) protein. The GFP(S11)-tag (bold, underlined) is inserted after amino 2 of 3A without any linker residues. The hydrophobic domain, predicted by the Kyte and Doolittle method (67), is indicated as well as the location of the helical hairpin predicted by NMR analysis of the truncated poliovirus 3A protein (68). B, C) HeLa R19 (B) or BGM (C) cells were co-transfected with the plasmid encoding GFP(S1-10) (i.e. pGFP(S1-10)) and either p3A-myc or p3A(S11aa2)-myc. The next day, cells were fixed and subjected to immunofluorescence analysis. The 3A protein was visualized with an antibody staining for p3A-myc (a primary anti-3A antibody and a secondary Alexa488-labeled antibody), while p3A(S11aa2) was visualized by the GFP fluorescence as a result of assembly with GFP(S1-10). PI4KB (A) or COP-I (B) were detected with immunofluorescence using a secondary Alexa594-labeled antibody. Untransfected cells are indicated with an asterisk. Nuclei were stained with DAPI. Wide-field images were acquired with an Olympus BX60 fluorescence microscope. Scale bars equal 10 µm.

demonstrated by the dissociation of COP-I from Golgi membranes in BGM cells (44), presumably as a result of the interaction of 3A with GBF1 (30, 44). Similar to untagged 3A, 3A(S11aa2) visualized by co-expression of GFP(S1-10) clearly caused COP-I dissociation (Fig. 1C).

In addition to the interaction with GBF1, enterovirus 3A also directly binds to the host factor ACBD3 (acyl-CoA-binding protein domain 3), although the role of this protein in enterovirus

replication is still enigmatic (38, 39, 45–47). We tested whether 3A(S11aa2) could still interact with GBF1 and ACBD3 in a mammalian two-hybrid system (38, 39). Similar to untagged 3A, 3A(S11aa2) interacted with GBF1 and ACBD3, even in the presence of overexpressed GFP(S1-10) (Fig. S2). Collectively, our results demonstrate that introduction of GFP(S11) in CVB3 3A after the second residue does not affect the ability of 3A to interact with previously identified host factors or to perform its known functions, which prompted us to introduce GFP(S11) into the viral genome of CVB3.

Tagging 3A with GFP(S11) results in a replication-competent CVB3 that generates fluorescent replication organelles

Introduction of the GFP(S11)-tag into the infectious clone of CVB3 yielded viable virus, i.e. CVB3-3A(S11aa2). Sequence analysis of the viral genome confirmed that the tag was retained in the 3A protein without mutations. In addition, we generated a replication-competent CVB3 with the short affinity tag StrepII of 10 residues in 3A (i.e. CVB3-3A(StrepIIaa2)). Insertion of the StrepII-tag also did not affect the known functions of 3A (data not shown), and the tag was retained in 3A for five passages (data not shown), further demonstrating that residue 2 is an amenable site for introduction of a small tag.

Subsequently, we tested whether the GFP(S11)-tag in 3A affects the replication kinetics of the virus. Since cells that have been transfected with plasmid DNA are less susceptible to picornavirus infection (48), we generated single cell clones of HeLa and BGM cells that stably express GFP(S1-10). Next, we compared the growth kinetics of CVB3-3A(S11aa2) to wild-type (wt) CVB3 in the presence and in the absence of GFP(S1-10). Samples were subjected to endpoint titration to determine the production of infectious virus, or quantitative PCR to measure viral RNA levels. Replication of wt CVB3 in BGM cells and BGM(GFPS1-10) cells was nearly identical, showing that the presence of GFP(S1-10) did not alter CVB3 replication kinetics (Fig. 2A, 2B). The replication kinetics of tagged CVB3 in BGM(GFPS1-10) also resembled that of BGM cells, indicating that binding of GFP(S1-10) to 3A(S11aa2) does not impede replication (Fig. 2A, 2B). Both infectious virus production and viral RNA levels of the tagged CVB3 were delayed compared to wt CVB3 (Fig. 2B). This delay in replication has also been observed for recombinant polioviruses that encode 3A proteins with small epitope tags (32). Together, these findings showed that replication of CVB3-3A(S11aa2) is similar to other enteroviruses that encoding small tags in a viral protein.

Having produced replication-competent CVB3-3A(S11aa2), we then tested whether this virus induced GFP fluorescence in cells expressing GFP(S1-10). Figure 3 (left images) shows that these cells do emit GFP fluorescence upon infection with CVB3-3A(S11aa2). To investigate whether the GFP fluorescence was restricted to the sites where the 3A(S11aa2) proteins are localized in the cell, we first stained cells with an anti-GFP antibody. Figure 3A shows that the anti-GFP antibody recognized GFP(S1-10) as demonstrated by the cytoplasmic staining in uninfected cells, whereas BGM cells lacking GFP(S1-10) were negative (data not shown). In infected cells, GFP fluorescence was not observed throughout the entire cytoplasm, but instead in a pattern that is reminiscent of a 3A staining pattern. This suggests that assembled, fluorescent GFP is only found at sites that contain 3A(S11aa2). Interestingly, while anti-GFP antibody staining in infected cells was detected throughout the cytoplasm, the signal was more intense at regions corresponding to GFP fluorescence. This is likely the result of recruitment of GFP(S1-10) to sites where 3A is localized. Another possibility is that

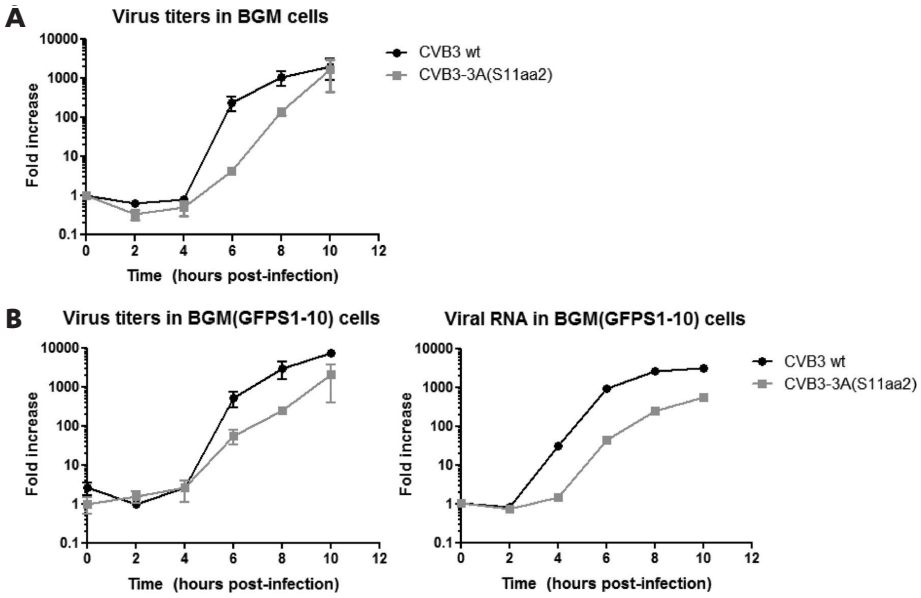


Figure 2. Single-cycle growth curve analysis of CVB3-3A(S11aa2). BGM cells (A) or BGM cells that stably express GFP(S1-10) (B) were infected with wt CVB3 or CVB3-3A(S11aa2) for 30 min at MOI 1. At the indicated time points, cells were subjected to titration analysis after freeze-thawing cycles to determine the amount of infectious virus particles. Alternatively, cells were lysed to determine the amount of viral RNA by quantitative PCR. The results are expressed as fold induction relative to the quantities determined directly after removing the inoculum.

the anti-GFP antibody has a higher affinity for full-length, assembled GFP.

To ensure that GFP fluorescence is exclusively emitted from 3A(S11aa2)-containing sites, cells from the same infection were stained with an anti-3A antibody. Figure 3B shows that GFP fluorescence was detected in a pattern that greatly overlapped with 3A visualized by immunofluorescence. However, the immunofluorescence with the 3A-antibody generated a slightly more extensive 3A-pattern, most likely as a consequence of not all 3A(S11aa2) proteins being bound by GFP(S1-10). This could be due to partial inaccessibility of 3A(S11aa2) proteins to their GFP(S1-10) counterparts as 3A proteins localize to densely-packed ROs.

Next, we set out to confirm that the emerging GFP fluorescence is emitted from ROs that contain 3A(S11aa2). To this end, we applied correlative light electron microscopy (CLEM) (49, 50), which provides a direct link between fluorescent signals and the virus-induced structures that underlie them at high resolution. The emerging fluorescence signal in BGM (GFPS1-10) cells infected with CVB3-3A(S11aa2) and stained with Mitotracker Deep Red FM was monitored by live-cell imaging. Cells were imaged and fixed at an intermediate time point in infection. Following sample processing and EM imaging, the Mitotracker signal and corresponding mitochondria were used to orient fluorescence and EM images with an independent marker. Using this method, 3A(S11aa2) was found to localize to ROs, evident as both tubules and clusters of DMVs and multilamellar structures (Fig. 4). Furthermore, the CLEM results not only show that GFP fluorescence was emitted from bona fide ROs, they also demonstrate that the GFP(S11) insertion in 3A does not affect the development of the different RO morphologies typically observed during enterovirus infections.

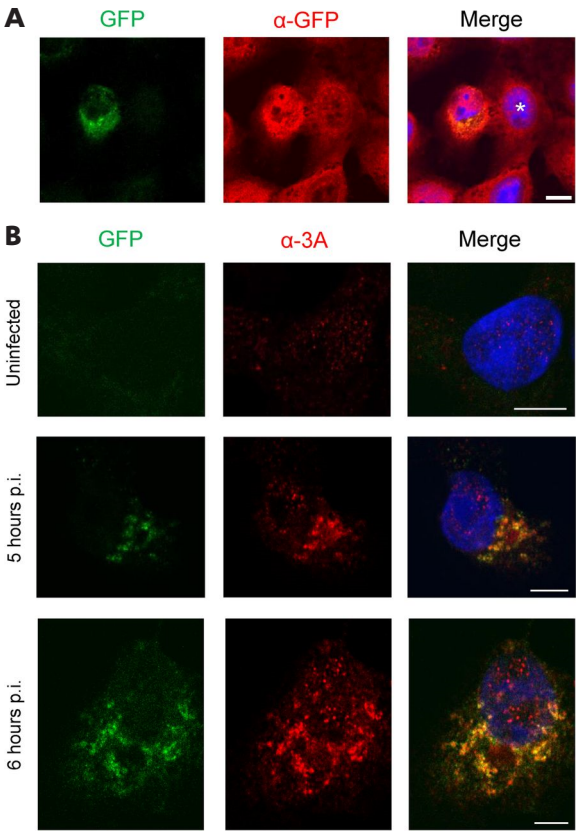


Figure 3. GFP fluorescence is only emitted from sites where 3A(S11aa2) is localized in cells. A, B) BGM cells stably expressing GFP(S1-10) were infected with CVB3-3A(S11aa2). At 5 and 6 h p.i., cells were fixed and subjected to immunofluorescence analysis. The detected GFP fluorescence is the result of GFP(S1-10) assembling with 3A(S11aa2). Nuclei were visualized with DAPI. Images were acquired with a Leica SPE-II DMI-4000 confocal laser scanning microscope. Scale bars equal 10 µm. A) GFP(S1-10) was detected with a primary polyclonal antibody directed against GFP and a secondary Alexa594-labeled antibody. The uninfected cell is marked with an asterisk. B) The 3A(S11aa2) protein was stained with a primary antibody directed against 3A and a secondary Alexa594-labeled antibody. An uninfected cell and typical examples of cells early in infection (5 h p.i.) and later in infection (6 h p.i.) are shown.

Live-cell imaging reveals the dynamics of Golgi disassembly in live infected cells

Enterovirus infections trigger the disassembly of the Golgi apparatus, which coincides with the formation of early ROs (18, 22). Here, we used live-cell imaging to visualize this process in living cells. To this end, BGM cells stably expressing GFP(S1-10) were transduced with MLV particles encoding mCherry-GM130 as a traceable marker for the Golgi. Live-cell confocal imaging was first carried out with a narrow pinhole (95.56 µm) to detect the first local changes in Golgi structure during infection. As expected, GM130 was observed as a condensed perinuclear signal in uninfected cells (Fig. 5A) or early in infection with CVB3-3A(S11aa2) when fluorescent 3A (which will be further referred to as 3A-GFP) could not yet be detected (Fig. 5B, Movies S1 and S2). Strikingly, the first 3A-GFP signal detected in infected cells was rarely associated with GM130, but could instead be observed as distinct cytoplasmic punctae. Localization of 3A-GFP signal to the Golgi region typically occurred

within 25 minutes (n=17, range 0-45 minutes) of initial detection. This was followed by a sharp increase in the intensity and number of Golgi-adjacent 3A-GFP punctae and a local perturbation of Golgi morphology, characterized by the onset of GM130 signal fragmentation (Fig. 5B, asterisk GM130 channel). Interestingly, while this rapidly increasing 3A-GFP signal was clearly detected in the Golgi region, it rarely co-localized directly with the GM130 marker (Fig. 5B inset, arrowhead), which is in agreement with previous observations in fixed cells (22). This suggests that RO membranes originate from a compartment of the Golgi not labeled by the cis-Golgi marker GM130, or that 3A resides there only transiently before accumulating in the ROs.

The first signs of disruption of Golgi morphology largely began during or even preceding the accumulation of visible 3A signal (Fig. 5B asterisk 3A-GFP channel, Movie S1), suggesting that local changes to morphology occur rapidly and may be triggered by 3A accumulation in regions of the Golgi outside the imaging plane. To facilitate the detection of the whole Golgi and to monitor large scale changes in Golgi morphology, imaging was carried out using a wider confocal

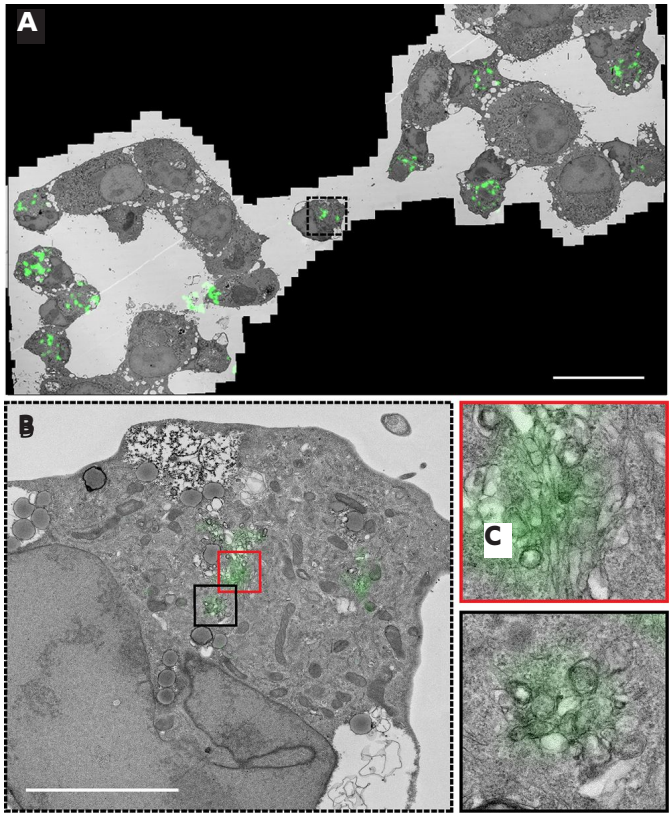


Figure 4. 3A(S11aa2) localizes to ROs that have tubule and DMV morphologies. A, B) BGM GFP(S1-10) cells were infected with CVB3-3A(S11aa2), stained with Mitotracker Deep Red FM and monitored by live cell imaging. Full-depth z-stacks of cells emitting GFP fluorescence were taken and cells were processed for EM. LM-EM overlays were made using the Mitotracker as an orientation guide, and 3A-GFP signal was aligned to the corresponding EM image in this manner first at low magnification (A), and then within individual cells of interest (B, which is the boxed area in A). 3A-GFP signal was found at the typical structures that develop during CVB3 infection, including single-membrane tubules (B, red box, enlargement shown on the right) and double-membrane vesicles (B, black box, enlargement shown on the right). Scale bars equal 30 µm (A) and 5 µm (B).

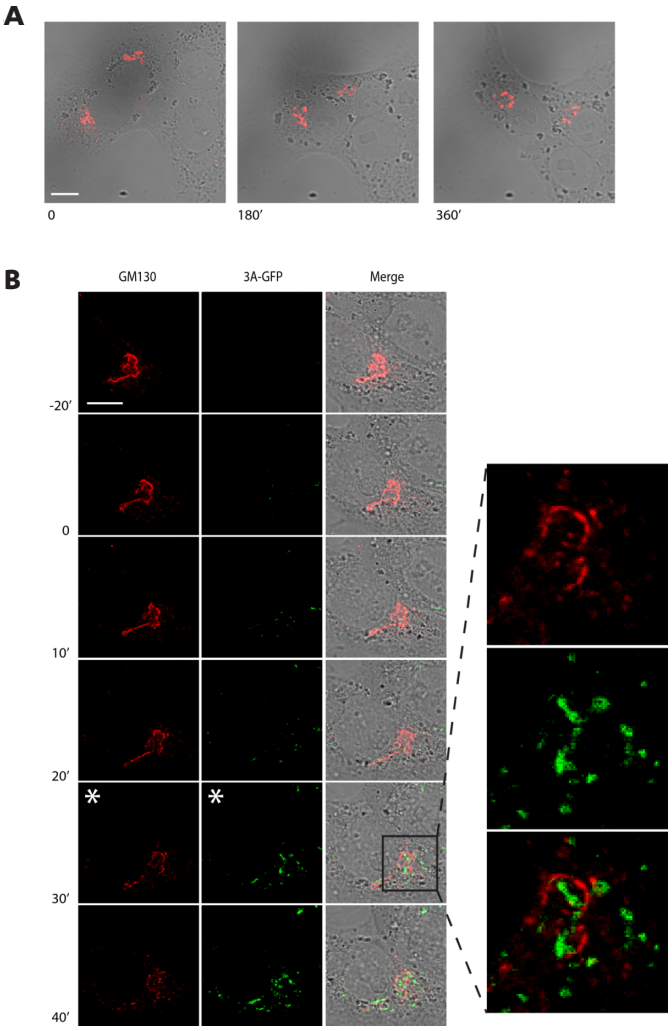


Figure 5. Live-cell imaging reveals the association between 3A accumulation and local perturbation to Golgi morphology. A, B) BGM GFP(S1-10) cells transduced with mCherry-GM130 MLV particles were mock-infected (A) or infected with CVB3-3A(S11aa2) (B), and imaged by live-cell microscopy with images taken at 5 minute intervals. The frames given as time '0' represent either an arbitrary time point (A) or the moment of appearance of 3A-GFP signal (B). Images are presented at 180 (A) or 10 to 20 (B) min intervals as indicated. The confocal pinhole was adjusted for analysis of local effects (95.56 µm confocal pinhole). While Golgi integrity was maintained for the duration of imaging in mock cells (A), local fragmentation of GM130 was evident in infected cells (B, asterisk GM130 channel). The onset of fragmentation was associated with a marked increase in the intensity and number of 3A-GFP punctae at the Golgi (B, asterisk 3A-GFP channel) although, while 3A signal and GM130 were proximal at this stage, there was no clear colocalization (B inset). Scale bar equals 10 µm.

pinhole (600 µm). Global Golgi fragmentation began typically 10-30 minutes after 3A started to accumulate in high amounts (Fig. 6) (n=8, range 0-45 min), which presumably reflects the time taken for the cumulative local changes to become apparent within the entire structure, and was completed 75-105 min after the initial detection of 3A-GFP signal (n=8). Together, these data show that 3A accumulation coincides with the local disruption of Golgi morphology, leading to

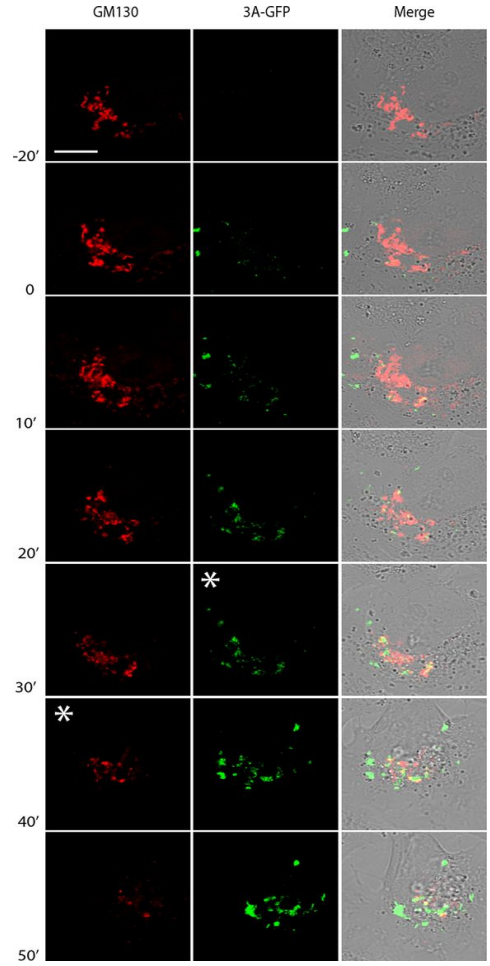


Figure 6. Global disruption to Golgi morphology during CVB3 infection visualized by live-cell imaging. Cells were treated as described in Figure 5. Imaging conditions were adjusted to better ascertain global Golgi morphology (600 µm confocal pinhole) over the course of infection. The frame given as time '0' represents the moment of appearance of 3A-GFP signal. Golgi fragmentation (asterisk GM130 channel) was visible following accumulation of 3A-GFP (asterisk 3A-GFP channel), leading to complete disassembly and a punctate GM130 signal. Scale bar equals 10 µm.

global fragmentation and eventual disassembly of the Golgi apparatus. After complete Golgi fragmentation, the 3A-GFP signal expands throughout the cell and eventually occupies the entire cytoplasm before the cell goes into demise, demonstrating that 3A-GFP signals can be imaged to the point of cell lysis (Movies S1 and S2).

Construction of CVB3 encoding both GFP(S1-10) and 3A(S11aa2)

Studying ROs induced by CVB3 encoding split-GFP-tagged 3A in distinct cell types requires the cellular expression of GFP(S1-10). To bypass the need for delivering the GFP(S1-10) gene via retroviral transduction or by generating stable cell lines, we constructed a CVB3 that encodes not

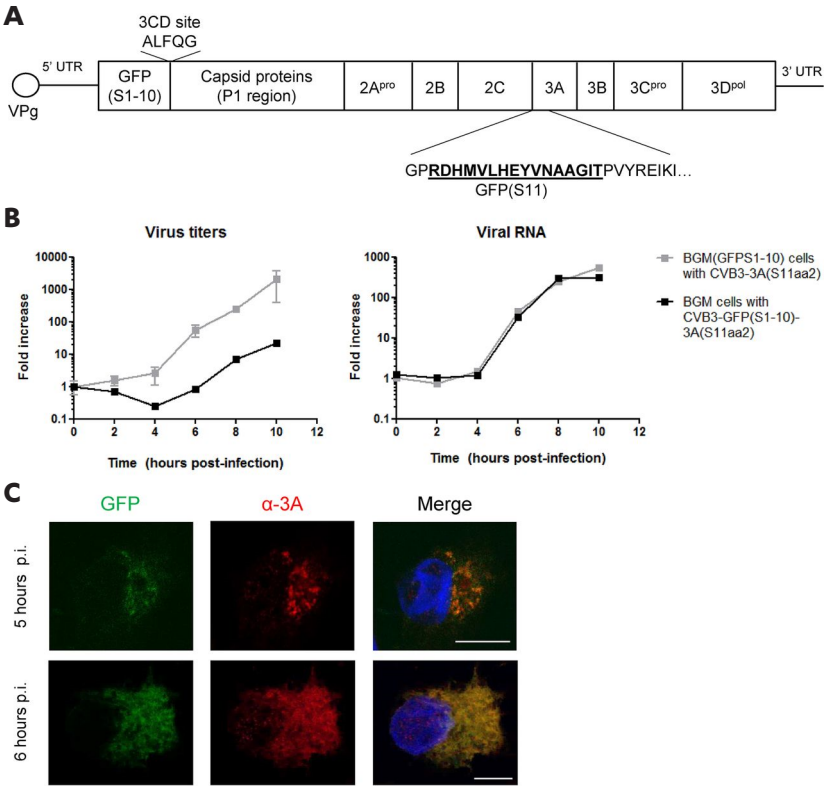


Figure 7. Construction of CVB3 that encodes both GFP(S1-10) and 3A(S11aa2). A) A schematic diagram of the genome organization of CVB3 showing the insertion of GFP(S1-10) before the capsid coding region and GFP(S11) in 3A after amino acid 2. B) Growth curve analysis of CVB3-GFP(S1-10)-3A(S11aa2) in BGM cells and CVB3-3A(S11aa2) in BGM(GFPS1-10) cells. Cells were infected for 30 min at MOI 1. At the indicated time points, cells were subjected to titration analysis after freeze-thawing cycles to determine the amount of infectious virus particles. Alternatively, cells were lysed to determine the amount of viral RNA with quantitative PCR. The results are expressed as fold induction relative to the quantities determined directly after removing the inoculum. C) BGM cells were infected with CVB3 GFP(S1-10) 3A(S11aa2). At 5 and 6 h p.i., cells were fixed and subjected to immunofluorescence analysis. The detected GFP fluorescence resulted from the assembly of GFP(S1-10) with 3A(S11aa2). Nuclei were visualized with DAPI. Images were acquired with a Leica SPE-II DMI-4000 confocal laser scanning microscope. Typical examples of cells early in infection (top panel) and later in infection (lower panel) are shown. Scale bars equal 10 µm.

only 3A(S11aa2) but also GFP(S1-10) (Fig. 7A). For this, the gene encoding GFP(S1-10) was inserted upstream of the capsid coding region (P1) in the infectious clone containing 3A(S11aa2). GFP(S1-10) was followed by an artificial 3CD cleavage site to release the protein from the P1 region upon translation. Viable virus (i.e. CVB3-GFP(S1-10)-3A(S11aa2) was obtained upon transfection of BGM cells with RNA transcripts of the infectious clone. After harvesting CVB3-GFP(S1-10)-3A(S11aa2), we compared its replication kinetics in BGM cells to CVB3-3A(S11aa2) in BGM(GFPS1-10), so that in both cases the 3A(S11aa2) protein would bind to GFP(S1-10). The level of viral RNA replication was nearly identical for both viruses (Fig. 7B), suggesting that the generation of ROs during the course of infection occurs similarly. However, the virus encoding both GFP fragments (i.e. CVB3-GFP(S1-10)-3A(S11aa2)) was delayed in production of infectious progeny in comparison to CVB3-3A(S11aa2) (Fig. 7B). In line with a previous study (51), we found that the processing of the artificial 3CD cleavage site

between a foreign protein and P1 is suboptimal (Fig. S3), which may explain the delay in progeny virion production.

Next, we tested whether BGM cells became GFP fluorescent upon infection with CVB3-GFP(S1-10)-3A(S11aa2). Figure 7C shows that GFP fluorescence colocalized with 3A, visualized with an anti-3A antibody, both early (upper panel) and later (lower panel) in infection. Yet, the GFP fluorescence was substantially dimmer compared to BGM(GFPS1-10) cells infected with CVB3-3A(S11aa2). It is plausible that the dimmer signal is a result of the equimolar ratios of 3A(S11aa2) and GFP(S1-10) generated by this virus, while BGM(GFPS1-10) cells produce an excess of GFP(S1-10). Another explanation for the dim GFP fluorescence is that not all GFP(S1-10) is released from P1 due to suboptimal cleavage of the artificial cleavage site. When GFP(S1-10) is still fused to P1, it might be unable to assemble with 3A(S11aa2) and/or become fluorescent. Nevertheless, these findings suggest that the virus containing both GFP fragments is suitable for live-cell imaging.

DISCUSSION

Live-cell imaging is a powerful technology to gain insight into the dynamics of biological processes. In the field of virology, this method has mostly been applied to visualize the entry and egress pathways of viruses by following the fate of fluorescently labeled, individual virus particles in living cells and monitoring their interactions with cellular structures (52). Imaging replication structures during infection has so far only been reported for a few viruses, including hepatitis C virus (53, 54), vaccinia virus (55), turnip mosaic virus (56), mouse hepatitis virus (57, 58) and equine arteritis virus (59). In most of these studies, replication structures are illuminated by a viral protein that is fused to GFP. Recombinant enteroviruses that encode an RO-anchored viral protein fused to GFP (or another fluorescent reporter) have to date not been reported. Small epitope tags on the other hand were successfully introduced in the 3A protein of poliovirus (32), which prompted us to test whether small tags suitable for fluorescent labeling are accepted in the 3A protein of CVB3. The smallest tag for fluorescent labeling of a protein is the tetracysteine tag of 6-20 residues (depending on the version), but it requires visualization with biarsenical dyes FlAsH and ReAsH in extra labeling steps, and results in fluorescence with a relatively poor quantum yield (60, 61). The split-GFP system uses a tag of 16 residues, GFP(S11), which has the advantage that it does not require staining but becomes directly fluorescent upon assembly with the large GFP(S1-10) fragment in living cells (34). This system has been successfully applied before in the context of a virus to study the intracellular trafficking of ribonucleoproteins of Influenza A virus, where the PB2 polymerase subunit was tagged with GFP(S11) (62). In our study, we incorporated GFP(S11) into the RO-anchored 3A protein of CVB3. We show that the introduction of GFP(S11) after the second residue does not affect the localization or function of 3A when it is expressed in isolation. Whether binding of GFP(S1-10) affects the function of 3A(S11aa2) proteins remains unknown, as it is possible that not all 3A(S11aa2) proteins are bound by the GFP(S1-10) counterparts. Therefore, the subset of unbound 3A(S11aa2) proteins could be solely responsible for exerting the 3A functions.

Having found that the 3A protein was not functionally hampered by the introduction of the GFP(S11)-tag, we generated a recombinant CVB3 that encodes 3A(S11aa2). Infections of this virus in BGM cells stably expressing GFP(S1-10) yielded discrete fluorescent signals. However, confirming that the fluorescent foci localize to virus-induced structures demands the higher resolution images

of sub-cellular structures, in the context of their surroundings, that EM can provide. Establishing this link with ultrastructure is particularly interesting in the case of enteroviruses, since their ROs can adopt various morphologies during infection (i.e. tubules, DMVs, and multilamellar structures) which, as observed by EM, often co-exist. In this study, CLEM was employed to confirm that the GFP fluorescent foci localize to ROs and to establish which subset of enterovirus RO morphologies this fluorescence corresponded to. CLEM revealed that the GFP fluorescence was present at bona fide ROs, which took the form of both tubular structures and DMVs resembling those observed previously with wt CVB3 in Vero cells (18). Split-GFP CLEM thus allows the unambiguous identification of RO morphologies underlying the 3A signal, and opens up new possibilities for a better understanding of the requirements for their development. This method also circumvents limitations inherent in other, similar approaches. For instance, while immuno-gold labeling of proteins is a popular technique that couples an electron-dense gold particle to the protein of interest, allowing it to be visualized by EM, its success depends largely upon the antibody used and the resilience of epitopes during EM sample preparation. In our experience, sample preparation procedures for immunolabeling of CVB3 3A that retain RO membranes unfortunately do so at the expense of viral epitope integrity, resulting in insufficient labeling of 3A (unpublished data).

Enterovirus ROs were imaged in living BGM(GFPS1-10) cells upon infection with CVB3-3A(S11aa2). As a proof of concept, we also expressed GM130-mCherry in these cells to visualize Golgi disassembly in real time. The onset of Golgi fragmentation was found to correspond to a period of rapid 3A accumulation in the Golgi region. Under the experimental conditions used, Golgi disruption was completed within 75-105 min after the first detection of 3A-GFP. Interestingly, while 3A accumulation occurred adjacent to the GM130 signal, 3A rarely co-localized with GM130-mCherry before and during Golgi disassembly. While this does not preclude the transient localization of 3A to the cis-Golgi, our findings suggest that ROs may be generated from another Golgi compartment not labeled by GM130, which is in line with previous observations that suggest that RO formation is initiated at the trans-Golgi (22).

Enteroviruses can infect both polarized and non-polarized cells. The use of CVB3 encoding split-GFP-tagged 3A in distinct cell types relies on the cellular expression of GFP(S1-10). As an alternative to delivering the GFP(S1-10) gene via transduction, we introduced the coding sequence of GFP(S1-10) into the viral genome together with 3A(S11aa2). This new recombinant CVB3 encoding both GFP fragments also induced GFP fluorescent foci that colocalized with 3A. While progeny virion production by this virus was delayed, the viral RNA levels were very similar to CVB3-3A(S11aa2) infection of BGM(GFPS1-10) cells, implying that the "two-fragment virus" retained its ability to form ROs. Hence, this virus would be suitable for studying enterovirus ROs in physiologically more relevant cell types, including pancreatic cells (14) and 3D-cultured CaCo-2 cells (63), without the need for ectopic expression of GFP(S1-10).

In conclusion, we have presented split-GFP tagged CVB3 as a new tool for the direct visualization of enterovirus ROs in living cells, which will allow the study of their dynamics. Furthermore, the combination of live-cell imaging with CLEM will enable us to establish a direct link between events observed by fluorescence microscopy and morphologically distinct ROs, which could shed light onto the possible differentiated roles of these different virus-induced structures in enterovirus infection. This system will therefore serve as a valuable tool for future studies on the origin and function of enterovirus ROs.

FUNDING INFORMATION

This work was supported by research grants from the Netherlands Organisation for Scientific Research (NWO-VENI-863.12.005 to HMvdS, NWO-VENI-722.012.066 to JRPMS, NWO-VICI-91812628 to FJMvK, NWO-MEERVOUD 863.10.003 to MB) and the European Union 7th Framework (EUVIRNA Marie Curie Initial Training Network, grant agreement number 264286 to FJMvK). The funders had no role in study design, data collection and interpretation, or the decision to submit the work for publication.

ACKNOWLEDGEMENTS

The authors thank the staff at the LUMC light microscopy facility their technical help.

EXPERIMENTAL PROCEDURES

Cells. HeLa R19, BGM (buffalo green monkey), and COS-1 cells were grown in Dulbecco's minimal essential medium (DMEM, Lonza) supplemented with 10% fetal bovine serum and penicillin and streptomycin at 37oC and 5% CO2.

Plasmids and infectious clones. The expression construct encoding wild-type (wt) 3A, i.e. p3A-myc, was described elsewhere (64). GFP(S11), i.e. the residues RDHMVLHEYVNAAGIT, were inserted after amino acid 2 in CVB3 3A to yield p3A(S11aa2)-myc. For this, a forward primer containing the GFP(S11)-tag was used in a PCR reaction with p3A-myc as a template to generate 3A(S11aa2) as a PCR product. Wt 3A in p3A-myc was replaced with this PCR product using standard DNA cloning techniques. The same strategy was used to introduce GFP(S11) or the StrepII-tag (i.e. residues SAWSHPQFEK) in the infectious clone of CVB3 (p53CB3/T7) described elsewhere (64), yielding p53CB3-3A(S11aa2)/T7 or p53CB3-3A(StrepIIaa2)/T7. The GFP(S1-10) expression construct pCMV-mGFP(S1-10) was purchased from Sandia Biotech. For the production of CVB3 encoding both GFP(S1-10) and 3A(S11aa2), the GFP(S1-10) gene followed by a 3CD cleavage site was placed directly upstream of the capsid coding region P1 in p53CB3-3A(S11aa2)/T7, similar to modifications previously described for CVB3 encoding luciferase (27). For the production of MLVs (Murine Leukemia Virus particles), our genes of interest were cloned into the retroviral vectors pQCXIP (for GFP(S1-10) or mCherry-P4M-SidM) or pRetroQ-mCherry (for GM130), both purchased from Clontech, with standard DNA cloning techniques. In the resulting plasmids, the gene of interest is followed by an IRES and a puromycin resistance gene for the production of stable cell lines.

Retroviral particles and the production of stable cell lines. For the delivery of genes (i.e. GFP(S1-10), mCherry-GM130, or mCherry-SidM-P4M) into cells, we used an MLV-based retroviral vector system (Clontech). MLV stocks were produced by co-transfecting HEK293T cells with the plasmid pCAGGS-VSV-G encoding vesicular stomatitis virus protein G (VSV-G), the plasmid pMLV-Gag/Pol encoding the capsid proteins, reverse transcriptase, and integrase proteins, and the plasmid pQCXIP or pRetroQ-mCherry containing the gene of interest. Four to five days post-transfection, supernatants were harvested and cleared of cell debris by centrifugation and filtration through a 0.45 µm pore size filter. Stocks were buffered with 10 mM HEPES, aliquoted, and frozen at −80°C for later use. Prior to transduction, the MLV particles were 5 to 10 times concentrated

using a 100 kD-concentrator (Millipore). For the generation of single-cell clones stably expressing GFP(S1-10), BGM and HeLa cells were transduced and grown in the presence of puromycin (2 µg/ml for HeLa; 30 µg/ml for BGM) to generate pools of GFP(S1-10)-expressing cells, which were subsequently used to prepare single-cell clones by limiting dilution. Expression of GFP(S1-10) was monitored during passaging by immunofluorescence microscopy using the GFP antibody.

Mammalian two-hybrid assay. pACT, pBIND, and pG5Luc vectors were from Promega. pBIND-GBF1 encoding the N-terminus of GBF1, pACT-3A, and pBIND-3A were described previously (38, 39). pACT-ACBD3 was a kind gift from dr. J. Sasaki (Fujita Health University School of Medicine, Aichi, Japan) (45). pACT-3A(S11aa2) and pBIND-3A(S11aa2) were cloned with a forward primer containing the GFP(S11)-tag using standard DNA cloning techniques. Subconfluent layers of COS-1 cells seeded in 24 well plates were transfected with 350 ng of pACT, pBIND, and pG5Luc plasmids using Fugene6 (Promega) according to the manufacturer's protocol. At 48 h post-transfection (p.t.) cells were lysed and Renilla and Firefly luciferase levels were measured using the Dual-Luciferase assay kit (Promega) following the manufacturer's protocol. Values were converted to Firefly/Renilla signal ratios to correct for transfection efficiencies.

Virus infection. The production of CVB3 from infectious clones was described previously (39). Virus titers were determined by endpoint titration according to the method of Reed and Muench and expressed as 50% cell culture infective doses (CCID50). BGM or HeLa cells were infected with virus for 30 min to 1 hour. Following removal of the inoculum, fresh medium was added to the cells. At indicated time points, cells were either fixed for immunolabeling, lysed to measure the amount of viral RNA by quantitative PCR, or frozen to determine the amount of infectious virus particles by titration analysis.

Quantitative PCR. RNA was isolated from infected cells using a Nucleospin RNA kit (Machery-Nagel). cDNA was synthesized using random hexamers as primers with a TaqMan reverse transcription reagents kit (Roche). The cDNA was used for quantitative PCR with the forward primer 5'-CGTGGGGCTACAATCAAGTT-3', the reverse primer 5'-TAACAGGAGCTTTGGGCATC-3', and the LightCycler 480 SYBR Green I master kit (Roche) for 45 cycles (5 s at 95°C, 10 s at 60°C, and 20 s at 72°C) on a LightCycler 480 (Roche).

Western Blot analysis. Proteins were separated with 10% gradient PAGE using the Gradi-Gel™ gradient analysis kit (Elpis biotech). Samples were transferred to nitrocellulose membranes (Bio-Rad). After cutting the membrane in two at the 15 kD band of the marker, one membrane (proteins larger than 15 kD) was incubated with primary antibodies against mouse monoclonal anti-βactin (Sigma) and rabbit polyclonal anti-GFP described previously (44), which also recognizes GFP(S1-10). The membrane with proteins smaller than 15 kD was incubated with rabbit polyclonal anti-3A described previously (44). Secondary antibodies included IRDye 680-conjugated goat anti-mouse or IRDye 800-conjugated goat anti-rabbit (LI-COR). Images of blots were acquired with Odyssey Imaging System LI-COR.

Immunofluorescence microscopy. BGM or HeLa cells were grown to subconfluency on coverslips in 24-well plates. Where indicated, cells were transfected with 200 ng of plasmid DNA using Fugene6 according to the manufacturer's protocol or infected with CVB3-3A(S11aa2) at an MOI of 1-10. At 24 h p.t. or 5-6 h post-infection (p.i.), cells were fixed with 4% paraformaldehyde for 20 min at room temperature, followed by permeabilization with PBS-0.1% Triton X-100 for 10 min. Cells were then incubated sequentially with primary and secondary antibodies diluted in PBS containing

2% normal goat serum. Cellular proteins were detected with primary antibodies against PI4KIIIB (Millipore), GBF1 (BD Biosciences), COP-I (provided by F. Wieland, Biochemie-Zentrum, Heidelberg, Germany). GFP(S1-10) was detected with a GFP antibody and CVB3 3A proteins with a 3A antibody, both described previously (44). Conjugated goat anti-rabbit and goat anti-mouse Alexa Fluor 488 or Alexa Fluor 594 (Molecular Probes) were used as secondary antibodies. Nuclei were stained using DAPI. Coverslips were mounted with FluorSave (Calbiochem). Images were acquired with an Olympus BX60 fluorescence microscope with a 40x (0.75 NA) dry objective or a Leica SPE-II DMI-4000 confocal laser scanning microscope equipped with a 100x (1.4 NA) oil immersion objective, and the confocal pinhole adjusted to 1 airy unit (AU).

Live-cell imaging. BGM(GFPS1-10) cells were seeded in glass-bottom 4-chamber 35-mm dishes (CELLviewTM) and grown to ~35% confluency before transduction with MLV mCherry-GM130 particles. Infection with CVB3-3A(S11aa2) was carried out 18-24 hours later. Cells were washed with Fluorobrite medium (Thermo Fisher Scientific) supplemented with 8% fetal calf serum (FCS) and 25 mM HEPES just prior to imaging. Imaging was performed with a Leica SP5 confocal microscope equipped with a HyD detector and a 63x (1.4 NA) oil immersion objective, and the confocal pinhole adjusted to 95.56 µm as standard, or 600 µm to approximate wide-field imaging. Cells were maintained in a live-cell imaging chamber at 37°C and 5% CO2. GFP and mCherry were excited using a 488 nm or 561 nm laser respectively and appropriate emission filters, and positions (xyz) were marked and imaged sequentially at 5 minute intervals. For the generation of movies, live-cell imaging data were processed in ImageJ and aligned using the StackReg plugin.

Correlative light electron microscopy. Asymmetrical guide marks were scratched into glass-bottom 8-well chamber µ-slides (Ibidi), upon which BGM(GFPS1-10) cells were grown to subconfluency and infected with CVB3-3A(S11aa2). Just prior to imaging, and to later aid in the correlation of fluorescent and EM images, cells were incubated with 100 nM Mitotracker® Deep Red FM for 30 minutes, then washed several times in Fluorobrite medium supplemented with 8% FCS and 25 mM HEPES. Imaging was carried out from ~2 hours p.i. with a Leica SP8 confocal microscope equipped with a HyD detector, in a live-cell chamber at 37°C and 5% CO2 and using a 63x (1.4 NA) oil immersion objective. For each position of interest, a low resolution tile-scan was taken of the surrounding area, including guide marks, to aid in later re-identification. Z-stacks were acquired using a 1 AU pinhole and Nyquist frequency sampling. Cells were then fixed with 4% paraformaldehyde and 2.5% glutaraldehyde in 0.1 M Sørenson's phosphate buffer (PB) and processed for electron microscopy. Post-fixation was carried out with 1% osmium tetroxide for 1 hour in PB then 1% tannic acid in PB for 30 minutes, after which cells were serially dehydrated in ethanol and infiltrated and embedded in LX 112 resin (Ladd Research Industries) before polymerisation at 60°C. Positions of interest imaged earlier were identified on the resin block surface through comparison with (horizontally flipped) tilescan images, appropriate block-faces were trimmed and serial thin sections cut and collected on copper slot grids covered with a carbon-coated formvar layer. After post-staining grids with lead citrate and uranyl acetate, image meshes spanning large areas of the grid were collected on an FEI Tecnai 20 FEG electron microscope operated at 120 kV with a 4k x4k pixel charge-couple device (CCD) camera (US4000, Gatan) with binning 2 and a final image pixel size of 1.94nm. These individual images were later combined into composite stitches (65). Cells of interest were digitally extracted from their raw image files using ImageJ and Aperio Imagescope software packages for light microscope and electron microscope images, respectively. These

images were then overlaid using Adobe Photoshop CS6. The mitochondrial pattern in the EM images was compared with the Mitotracker® Deep Red FM signal to find the right transformations to correlate both types of data. While the discrepancy in the axial resolution of light and electron microscopes limited the precision of the overlay, the use of this secondary marker was critical to determine the z-plane in the confocal data the best fit the EM cell section under analysis and for xy orientation of both images, thus providing an independent marker for an unbiased localization of the 3A signal.

REFERENCES

1. Tapparel C, Siegrist F, Petty TJ, Kaiser L. 2013. Picornavirus and enterovirus diversity with associated human diseases. Infect. Genet. Evol. 14:282–93.
2. den Boon JA, Ahlquist P. 2010. Organelle-like membrane compartmentalization of positive-strand RNA virus replication factories. Annu. Rev. Microbiol. 64:241–56.
3. Miller S, Krijnse-Locker J. 2008. Modification of intracellular membrane structures for virus replication. Nat. Rev. Microbiol. 6:363–74.
4. Romero-Brey I, Bartenschlager R. 2014. Membranous replication factories induced by plus-strand RNA viruses. Viruses 6:2826–57.
5. Belov GA, van Kuppeveld FJM. 2012. (+)RNA viruses rewire cellular pathways to build replication organelles. Curr. Opin. Virol. 2:740–7.
6. van der Linden L, Wolthers KC, van Kuppeveld FJM. 2015. Replication and Inhibitors of Enteroviruses and Parechoviruses. Viruses 7:4529–62.
7. Neufeldt CJ, Joyce MA, Van Buuren N, Levin A, Kirkegaard K, Gale M, Tyrrell DLJ, Wozniak RW. 2016. The Hepatitis C Virus-Induced Membranous Web and Associated Nuclear Transport Machinery Limit Access of Pattern Recognition Receptors to Viral Replication Sites. PLoS Pathog. 12:e1005428.
8. Overby AK, Popov VL, Niedrig M, Weber F. 2010. Tick-borne encephalitis virus delays interferon induction and hides its double-stranded RNA in intracellular membrane vesicles. J. Virol. 84:8470–83.
9. Bienz K, Egger D, Rasser Y, Bossart W. 1983. Intracellular distribution of poliovirus proteins and the induction of virus-specific cytoplasmic structures. Virology 131:39–48.
10. Bienz K, Egger D, Pasamontes L. 1987. Association of polioviral proteins of the P2 genomic region with the viral replication complex and virus-induced membrane synthesis as visualized by electron microscopic immunocytochemistry and autoradiography. Virology 160:220–6.
11. Wong J, Zhang J, Si X, Gao G, Mao I, McManus BM, Luo H. 2008. Autophagosome supports coxsackievirus B3 replication in host cells. J. Virol. 82:9143–9153.
12. Schlegel A, Giddings TH, Ladinsky MS, Kirkegaard K. 1996. Cellular origin and ultrastructure of membranes induced during poliovirus infection. J. Virol. 70:6576–88.
13. Suhy DA, Giddings TH, Kirkegaard K. 2000. Remodeling the endoplasmic reticulum by poliovirus infection and by individual viral proteins: an autophagy-like origin for virus-

induced vesicles. J. Virol. 74:8953–65.

14. Kemball CC, Alirezaei M, Flynn CT, Wood MR, Harkins S, Kiosses WB, Whitton JL. 2010. Coxsackievirus infection induces autophagy-like vesicles and megaphagosomes in pancreatic acinar cells in vivo. J. Virol. 84:12110–24.
15. Volle R, Archimbaud C, Couraud P-O, Romero IA, Weksler B, Mirand A, Pereira B, Henquell C, Peigue-Lafeuille H, Bailly J-L. 2015. Differential permissivity of human cerebrovascular endothelial cells to enterovirus infection and specificities of serotype EV-A71 in crossing an in vitro model of the human blood-brain barrier. J. Gen. Virol. 96:1682–95.
16. Alirezaei M, Flynn CT, Wood MR, Harkins S, Whitton JL. 2015. Coxsackievirus can exploit LC3 in both autophagy-dependent and -independent manners in vivo. Autophagy 11:1389–407.
17. Belov GA, Nair V, Hansen BT, Hoyt FH, Fischer ER, Ehrenfeld E. 2012. Complex dynamic development of poliovirus membranous replication complexes. J. Virol. 86:302–12.
18. Limpens RWAL, van der Schaar HM, Kumar D, Koster AJ, Snijder EJ, van Kuppeveld FJM, Bárcena M. 2011. The transformation of enterovirus replication structures: a three-dimensional study of single- and double-membrane compartments. MBio 2.
19. Jackson WT, Giddings TH, Taylor MP, Mulinyawe S, Rabinovitch M, Kopito RR, Kirkegaard K. 2005. Subversion of Cellular Autophagosomal Machinery by RNA Viruses. PLoS Biol. 3:e156.
20. Chen Y-H, Du W, Hagemeijer MC, Takvorian PM, Pau C, Cali A, Brantner CA, Stempinski ES, Connelly PS, Ma H-C, Jiang P, Wimmer E, Altan-Bonnet G, Altan-Bonnet N. 2015. Phosphatidylserine vesicles enable efficient en bloc transmission of enteroviruses. Cell 160:619–30.
21. Bird SW, Maynard ND, Covert MW, Kirkegaard K. 2014. Nonlytic viral spread enhanced by autophagy components. Proc. Natl. Acad. Sci. U. S. A. 111:13081–6.
22. Hsu N-Y, Ilnytska O, Belov G, Santiana M, Chen Y-H, Takvorian PM, Pau C, van der Schaar H, Kaushik-Basu N, Balla T, Cameron CE, Ehrenfeld E, van Kuppeveld FJM, Altan-Bonnet N. 2010. Viral reorganization of the secretory pathway generates distinct organelles for RNA replication. Cell 141:799–811.
23. Belov GA, Altan-Bonnet N, Kovtunovych G, Jackson CL, Lippincott-Schwartz J, Ehrenfeld E. 2007. Hijacking components of the cellular secretory pathway for replication of poliovirus RNA. J. Virol. 81:558–67.
24. Richards AL, Soares-Martins JAP, Riddell GT, Jackson WT. 2014. Generation of unique poliovirus RNA replication organelles. MBio 5:e00833–13.
25. Rust RC, Landmann L, Gosert R, Tang BL, Hong W, Hauri HP, Egger D, Bienz K. 2001. Cellular COPII proteins are involved in production of the vesicles that form the poliovirus replication complex. J. Virol. 75:9808–9818.
26. Schnell U, Dijk F, Sjollema KA, Giepmans BNG. 2012. Immunolabeling artifacts and the need for live-cell imaging. Nat. Methods 9:152–8.
27. Lanke KHW, van der Schaar HM, Belov G a, Feng Q, Duijsings D, Jackson CL, Ehrenfeld E, van Kuppeveld FJM. 2009. GBF1, a guanine nucleotide exchange factor for Arf, is crucial for coxsackievirus B3 RNA replication. J. Virol. 83:11940–9.
28. Shang B, Deng C, Ye H, Xu W, Yuan Z, Shi P-Y, Zhang B. 2013. Development and characterization of a stable eGFP enterovirus 71 for antiviral screening. Antiviral Res. 97:198–205.

29. Robinson SM, Tsueng G, Sin J, Mangale V, Rahawi S, McIntyre LL, Williams W, Kha N, Cruz C, Hancock BM, Nguyen DP, Sayen MR, Hilton BJ, Doran KS, Segall AM, Wolkowicz R, Cornell CT, Whitton JL, Gottlieb RA, Feuer R. 2014. Coxsackievirus B Exits the Host Cell in Shed Microvesicles Displaying Autophagosomal Markers. PLoS Pathog. 10:e1004045.
30. Belov G a, Feng Q, Nikovics K, Jackson CL, Ehrenfeld E. 2008. A critical role of a cellular membrane traffic protein in poliovirus RNA replication. PLoS Pathog. 4:e1000216.
31. Teterina NL, Levenson EA, Ehrenfeld E. 2010. Viable polioviruses that encode 2A proteins with fluorescent protein tags. J. Virol. 84:1477–88.
32. Teterina NL, Pinto Y, Weaver JD, Jensen KS, Ehrenfeld E. 2011. Analysis of poliovirus protein 3A interactions with viral and cellular proteins in infected cells. J. Virol. 85:4284–96.
33. de Jong AS, Melchers WJG, Glaudemans DHRF, Willems PHGM, van Kuppeveld FJM. 2004. Mutational analysis of different regions in the coxsackievirus 2B protein: requirements for homo-multimerization, membrane permeabilization, subcellular localization, and virus replication. J. Biol. Chem. 279:19924–35.
34. Cabantous S, Terwilliger TC, Waldo GS. 2005. Protein tagging and detection with engineered self-assembling fragments of green fluorescent protein. Nat. Biotechnol. 23:102–107.
35. Towner JS, Ho T V, Semler BL. 1996. Determinants of membrane association for poliovirus protein 3AB. J. Biol. Chem. 271:26810–8.
36. Pédelacq J-D, Cabantous S, Tran T, Terwilliger TC, Waldo GS. 2006. Engineering and characterization of a superfolder green fluorescent protein. Nat. Biotechnol. 24:79–88.
37. Teterina NL, Lauber C, Jensen KS, Levenson EA, Gorbalenya AE, Ehrenfeld E. 2011. Identification of tolerated insertion sites in poliovirus non-structural proteins. Virology 409:1–11.
38. Dorobantu CM, Ford-Siltz LA, Sittig SP, Lanke KHW, Belov GA, van Kuppeveld FJM, van der Schaar HM. 2015. GBF1- and ACBD3-Independent Recruitment of PI4KIIIB to Replication Sites by Rhinovirus 3A Proteins. J. Virol. 89:1913–1918.
39. Dorobantu CM, van der Schaar HM, Ford LA, Strating JRPM, Ulferts R, Fang Y, Belov G, van Kuppeveld FJM. 2013. Recruitment of PI4KIIIB to coxsackievirus B3 replication organelles is independent of ACBD3, GBF1, and Arf1. J. Virol.
40. Lee MCS, Miller EA, Goldberg J, Orci L, Schekman R. 2004. Bi-directional protein transport between the ER and Golgi. Annu. Rev. Cell Dev. Biol. 20:87–123.
41. Bonifacino JS, Glick BS. 2004. The mechanisms of vesicle budding and fusion. Cell 116:153–66.
42. Cornell CT, Kiosses WB, Harkins S, Whitton JL. 2006. Inhibition of protein trafficking by coxsackievirus b3: multiple viral proteins target a single organelle. J. Virol. 80:6637–47.
43. Doedens JR, Kirkegaard K. 1995. Inhibition of cellular protein secretion by poliovirus proteins 2B and 3A. EMBO J. 14:894–907.
44. Wessels E, Duijsings D, Niu T-K, Neumann S, Oorschot VM, de Lange F, Lanke KHW, Klumperman J, Henke A, Jackson CL, Melchers WJG, van Kuppeveld FJM. 2006. A viral protein that blocks Arf1-mediated COP-I assembly by inhibiting the guanine nucleotide exchange factor GBF1. Dev. Cell 11:191–201.
45. Sasaki J, Ishikawa K, Arita M, Taniguchi K. 2012. ACBD3-mediated recruitment of PI4KB to picornavirus RNA replication sites. EMBO J. 31:754–66.

46. Greninger AL, Knudsen GM, Betegon M, Burlingame AL, Derisi JL. 2012. The 3A protein from multiple picornaviruses utilizes the golgi adaptor protein ACBD3 to recruit PI4KIIIβJ. Virol. 86:3605–16.
47. Téoulé F, Brisac C, Pelletier I, Vidalain P-O, Jégouic S, Mirabelli C, Bessaud M, Combelas N, Autret A, Tangy F, Delpeyroux F, Blondel B. 2013. The Golgi protein ACBD3, an interactor for poliovirus protein 3A, modulates poliovirus replication. J. Virol.
48. Langereis MA, Rabouw HH, Holwerda M, Visser LJ, van Kuppeveld FJM. 2015. Knockout of cGAS and STING Rescues Virus Infection of Plasmid DNA-Transfected Cells. J. Virol. 89:11169–73.
49. de Boer P, Hoogenboom JP, Giepmans BNG. 2015. Correlated light and electron microscopy: ultrastructure lights up! Nat. Methods 12:503–13.
50. Gibson KH, Vorkel D, Meissner J, Verbavatz J-M. 2014. Fluorescing the electron: strategies in correlative experimental design. Methods Cell Biol. 124:23–54.
51. Mattion NM, Reilly PA, DiMichele SJ, Crowley JC, Weeks-Levy C. 1994. Attenuated poliovirus strain as a live vector: expression of regions of rotavirus outer capsid protein VP7 by using recombinant Sabin 3 viruses. J. Virol. 68:3925–33.
52. Brandenburg B, Zhuang X. 2007. Virus trafficking - learning from single-virus tracking. Nat. Rev. Microbiol. 5:197–208.
53. Wölk B, Büchele B, Moradpour D, Rice CM. 2008. A dynamic view of hepatitis C virus replication complexes. J. Virol. 82:10519–31.
54. Eyre NS, Fiches GN, Aloia AL, Helbig KJ, McCartney EM, McErlean CSP, Li K, Aggarwal A, Turville SG, Beard MR. 2014. Dynamic imaging of the hepatitis C virus NS5A protein during a productive infection. J. Virol. 88:3636–52.
55. Schramm B, de Haan CAM, Young J, Doglio L, Schleich S, Reese C, Popov A V, Steffen W, Schroer T, Locker JK. 2006. Vaccinia-virus-induced cellular contractility facilitates the subcellular localization of the viral replication sites. Traffic 7:1352–67.
56. Cotton S, Grangeon R, Thivierge K, Mathieu I, Ide C, Wei T, Wang A, Laliberté J-F. 2009. Turnip mosaic virus RNA replication complex vesicles are mobile, align with microfilaments, and are each derived from a single viral genome. J. Virol. 83:10460–71.
57. Hagemeijer MC, Verheije MH, Ulasli M, Shaltiël IA, de Vries LA, Reggiori F, Rottier PJM, de Haan CAM. 2010. Dynamics of coronavirus replication-transcription complexes. J. Virol. 84:2134–49.
58. Hagemeijer MC, Ulasli M, Vonk AM, Reggiori F, Rottier PJM, de Haan CAM. 2011. Mobility and interactions of coronavirus nonstructural protein 4. J. Virol. 85:4572–7.
59. van den Born E, Posthuma CC, Knoops K, Snijder EJ. 2007. An infectious recombinant equine arteritis virus expressing green fluorescent protein from its replicase gene. J. Gen. Virol. 88:1196–205.
60. Griffin BA, Adams SR, Tsien RY. 1998. Specific covalent labeling of recombinant protein molecules inside live cells. Science 281:269–72.
61. Adams SR, Campbell RE, Gross LA, Martin BR, Walkup GK, Yao Y, Llopis J, Tsien RY. 2002. New biarsenical ligands and tetracysteine motifs for protein labeling in vitro and in vivo: synthesis and biological applications. J. Am. Chem. Soc. 124:6063–76.
62. Avilov S V, Moisy D, Munier S, Schraidt O, Naffakh N, Cusack S. 2012. Replication-competent

influenza A virus that encodes a split-green fluorescent protein-tagged PB2 polymerase subunit allows live-cell imaging of the virus life cycle. J. Virol. 86:1433–48.

63. Drummond CG, Nickerson CA, Coyne CB. 2016. A Three-Dimensional Cell Culture Model To Study Enterovirus Infection of Polarized Intestinal Epithelial Cells. mSphere 1:e00030–15.

64. Wessels E, Duijsings D, Notebaart RA, Melchers WJG, van Kuppeveld FJM. 2005. A proline-rich region in the coxsackievirus 3A protein is required for the protein to inhibit endoplasmic reticulum-to-golgi transport. J. Virol. 79:5163–73.

65. Faas FGA, Avramut MC, van den Berg BM, Mommaas AM, Koster AJ, Ravelli RBG. 2012. Virtual nanoscopy: generation of ultra-large high resolution electron microscopy maps. J. Cell Biol. 198:457–69.

SUPPLEMENTAL FIGURES

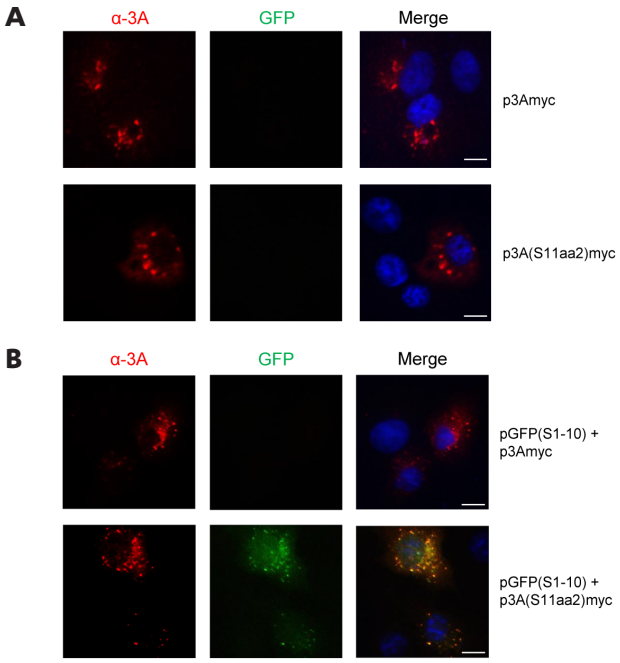


Figure S1. Co-expression of 3A(S11aa2) with GFP(S1-10) yields GFP fluorescence. A) Introduction of GFP(S11) into 3A does not alter its expression pattern. HeLa cells were transfected with plasmids encoding wild-type (wt) 3A (p3A-myc) or tagged 3A (p3A(S11aa2)-myc). One day later, the 3A protein was stained with an antibody directed against 3A and a secondary Alexa594-labeled antibody. B) GFP fluorescence is only detected when GFP(S1-10) is co-expressed with 3A(S11aa2). BGM cells were co-transfected with the plasmid encoding GFP(S1-10) (pGFP(S1-10)) and either p3A-myc or p3A(S11aa2)-myc. One day later, the 3A protein was stained with a primary antibody directed against 3A and a secondary Alexa594-labeled antibody. A, B) Nuclei were stained with DAPI. Wide-field images were acquired with an Olympus BX60 fluorescence microscope. Scale bars equal 10 µm.

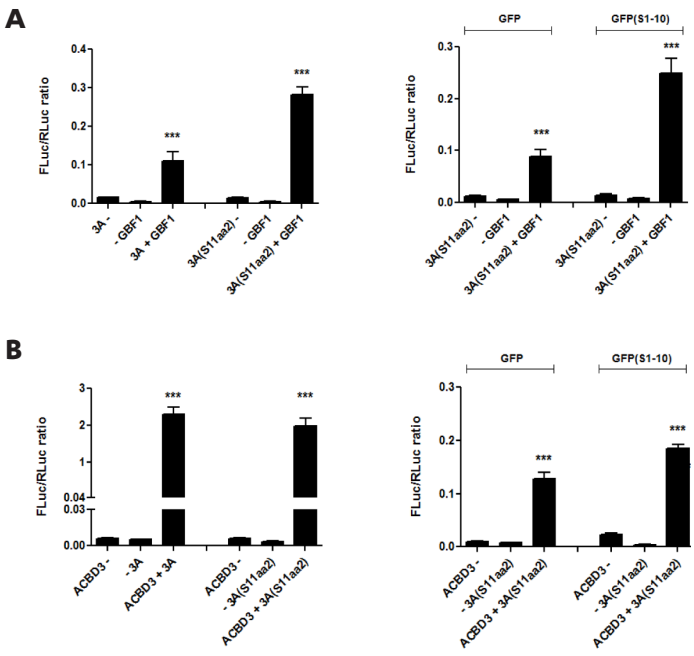


Figure S2. 3A(S11aa2) interacts with host factors GBF1 and ACBD3. A, B) A mammalian two-hybrid assay was used to determine the ability of 3A(S11aa2) to interact with the N-terminus of GBF1 (A) or ACBD3 (B). This assay was conducted in the absence of GFP(S1-10) (left graphs) or in the presence of GFP(S1-10) (right graphs) using full-length GFP as a transfection control. Bars represent the means of three samples ± standard deviations. Significant differences were calculated over the highest control sample by a paired Student t-test. ***, P<0.001

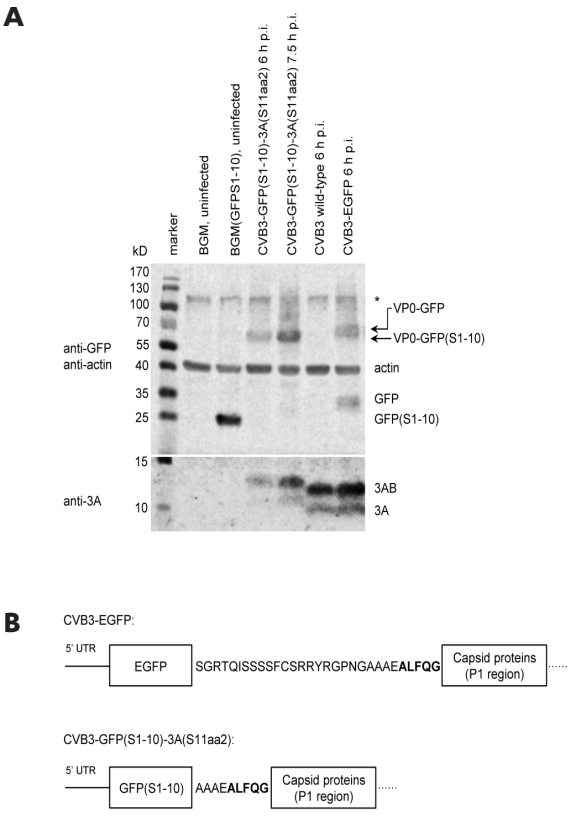


Figure S3. Processing of the artificial 3CD cleavage site between a foreign protein and P1 is suboptimal. A) BGM cells were infected with different CVB3 and lysates were prepared at the indicated time points. Cell lysates were subjected to Western Blot analysis using antibodies against actin (loading control), 3A (infection control), or GFP that also recognizes GFP(S1-10). An aspecific band is indicated with an asterisk. BGM cells that stably express GFP(S1-10) showed a band at around 25 kD, which is in accordance with the somewhat smaller size than full-length GFP (27 kD). BGM cells infected with CVB3-GFP(S1-10)-3A(S11aa2) accumulated a clear band at around 60 kD, which corresponds to the precursor VP0 (36 kD) fused to GFP(S1-10). Little, if any, GFP(S1-10) was detectable, indicating a defect in processing. We also examined CVB3-EGFP (27), which also is delayed in replication compared to wild-type CVB3, but not as severely as CVB3-GFP(S1-10)-3A(S11aa2). In these samples, GFP is detected as a fusion protein to VP0 as well as an individual protein. Both results demonstrate that processing of the artificial 3CD cleavage site is suboptimal. Why cleavage of full-length GFP from VP0 appeared more efficient than for CVB3-GFP(S1-10)-3A(S11aa2) remains to be determined. Since GFP(S1-10) folds differently than full-length EGFP, this may affect processing of the cleavage site. Also, EGFP is followed by a longer linker sequence upstream of the cleavage site (ALFQG, indicated in bold) compared to GFP(S1-10) (shown in B) due to cloning procedures, which may affect protein folding and processing.

Movie S1. Golgi disruption and 3A accumulation monitored over the course of CVB3 infection. Cropped view showing Golgi fragmentation at higher resolution (images are of cell shown in Figure 8B) from ~2 to 7.5 hours post infection. Fragmentation can be observed from approximately 3.5 hours post infection, and complete disassembly occurs within 30 minutes as evidenced by the punctate GM130 signal. Scale bar equals 10 µm, frame rate is 4 fps. Images were collected at 5 minute intervals.

Movie S2. The split-GFP system allows 3A to be monitored over the full course of CVB3 infection. Overview of a typical field of view during live-cell experiments from ~5 to 10 hours post infection (shown first with green, red and brightfield channels, then repeated with green and red channels only). Several phases of infection can be observed, including the developing 3A-GFP signal and associated disruption of Golgi morphology, and the accumulation of ROs in the cytoplasm leading ultimately to cell lysis. Scale bar equals 10 µm, frame rate is 4 fps. Images were collected at 5 minute intervals.

CHAPTER 3

ESCAPING HOST FACTOR PI4KB INHIBITION: ENTEROVIRUS GENOMIC RNA REPLICATION IN THE ABSENCE OF REPLICATION ORGANELLES

Charlotte E. Melia[1$], Hilde M. van der Schaar[2$], Heyrhyoung Lyoo[2], Ronald W.A.L. Limpens[1], Qian Feng[2†], Maryam Wahedi[2], Gijs J. Overheul[3], Ronald P. van Rij[3], Eric J. Snijder[4], Abraham J. Koster[1], Montserrat Bárcena[1&], Frank J.M. van Kuppeveld[2&]

Published in Cell Reports 2017. 21;3: 587-599
DOI: 10.1016/j.celrep.2017.09.068

[1] Department of Molecular Cell Biology, Leiden University Medical Center, Leiden, 2333 ZC, The Netherlands

[2] Department of Infectious Diseases & Immunology, Utrecht University, Utrecht, 3584 CL, The Netherlands

[3] Department of Medical Microbiology, Radboud Institute for Molecular Life Sciences, Nijmegen, 6525 GA, The Netherlands

[4] Department of Medical Microbiology, Leiden University Medical Center, Leiden, 2333 ZA, The Netherlands

[†]Current address: Institute of Biochemistry, ETH Zürich, 8093 Zürich, Switzerland

[$,&]These authors contributed equally

SUMMARY

Enteroviruses reorganize cellular endomembranes into replication organelles (ROs) for genome replication. Although enterovirus replication depends on phosphatidylinositol 4-kinase type III beta (PI4KB), its role, and that of its product PI4P, is only partially understood. Exploiting a mutant coxsackievirus resistant to PI4KB inhibition, we uncover that PI4KB activity has distinct functions in proteolytic processing of the viral polyprotein and in RO biogenesis. The escape mutation rectified a proteolytic processing defect imposed by PI4KB inhibition, pointing to a possible escape mechanism. Remarkably, under PI4KB inhibition the mutant virus could replicate its genome in the absence of ROs, using instead the Golgi apparatus. This impaired RO biogenesis provided an opportunity to investigate the proposed role of ROs in shielding enteroviral RNA from cellular sensors. Neither accelerated sensing of viral RNA nor enhanced innate immune responses were observed. Together, our findings challenge the notion that ROs are indispensable for enterovirus genome replication and immune evasion.

INTRODUCTION

Positive-strand RNA (+RNA) viruses comprise many human pathogens, such as hepatitis C virus, Zika virus, dengue virus, SARS- and MERS-coronavirus, and enteroviruses. Despite substantial genetic divergence across virus families, some features of replication are common to all +RNA viruses infecting eukaryotes. One of the most striking is the remodelling of host cell endomembranes into novel membranous compartments in the cytoplasm of the infected cell. These compartments serve as compositionally unique platforms upon which the components of the viral RNA synthesis machinery assemble, and whose micro-environments may facilitate efficient genome replication (reviewed in (1) and (2)). In addition, they have been postulated to play a role in the evasion of the innate antiviral host responses by shielding viral RNA products from cytosolic sensors such as MDA5 and RIG-I, which signal to activate the type I interferon (IFN-a/b) pathway, and protein kinase R (PKR), which activates an integral stress response (3, 4).

Members of the Enterovirus genus, belonging to the Picornaviridae family, include poliovirus, coxsackie A and B viruses, several numbered enteroviruses (e.g. EV-D68, EV-A71), and rhinoviruses, which are causative agents of various human diseases. Enteroviruses, like other positive-sense RNA viruses, modify host-cell membranes to form structures with novel morphologies. These modified membranes serve as platforms for viral replication, which we will refer to as replication organelles (ROs). At earlier stages of coxsackievirus B3 (CVB3) or poliovirus (PV) infection, ROs emerge as single-membrane tubules that appear to form at the expense of the Golgi apparatus. These tubules are interspersed with double-membrane vesicles (DMVs), which are believed to arise as tubules deform and enwrap small volumes of cytosol. In this way, most tubules transform into DMVs over the course of infection, and DMVs may be further enwrapped to form multilamellar vesicles (5, 6). Each stage of virus replication, including the transformation of cellular membranes into ROs, is dependent upon the interplay between viral proteins and host factors. The small, membrane-anchored enterovirus 3A protein has a key role in generating ROs (7), and is known to recruit host factors that are essential for genome replication. One of these factors is phosphatidylinositol 4-kinase type IIIβ (PI4KB) (8, 9). In uninfected cells PI4KB is a Golgi-resident enzyme that generates

phosphatidylinositol 4-phosphate (PI4P), while during enterovirus infection the viral 3A protein recruits PI4KB to ROs, enriching them in PI4P (8, 10).

The importance of PI4P in viral infections has been the subject of several recent investigations, both for the Picornaviridae, such as Aichivirus (genus Kobuviruses) and encephalomyocarditis virus (EMCV) (genus Cardiovirus) and for other +RNA viruses, such as hepatitis C virus (HCV) (reviewed in (11) and (12)). In uninfected cells, PI4P is involved in a multitude of functions, including signalling, membrane trafficking, regulation of Golgi apparatus organisation, and lipid homeostasis (reviewed in (13) and (14)). Of particular relevance for viruses that utilise PI4P is the counterflux of PI4P and cholesterol between Golgi apparatus and ER, which is mediated by the oxysterol-binding protein (OSBP). OSBP acts as a bridge between these two membrane compartments to generate a membrane contact site, using PI4P as a Golgi-based anchor and vesicle-associated membrane protein-associated protein A (VAP-A) as an ER anchor (15). During enterovirus infection, OSBP is diverted to create a novel type of membrane contact site between ROs and the ER. These sites mediate the exchange of PI4P for cholesterol, which is another essential lipid for enterovirus genome replication (16-18).

Recruitment of PI4KB by the viral 3A protein is critical for enterovirus genome replication (8, 9), but its exact role is unclear. The stage of genome replication in the enterovirus life cycle encompasses different processes, including proteolytic processing of the polyprotein, RO biogenesis, and RNA synthesis by the viral replication machinery. In this study, we used a CVB3 mutant resistant to PI4KB inhibition, i.e. CVB3 3A-H57Y (19), to further dissect the role of PI4KB and the PI4P-rich environment it generates during genome replication. We show that PI4KB activity facilitates efficient proteolytic processing of the CVB3 polyprotein. The 3A-H57Y substitution compensates for the impairment of polyprotein processing caused by PI4KB inhibition, which may represent the escape mechanism of this mutant virus. Distinct from its effect on polyprotein processing, we found that PI4KB inhibition also delayed RO formation. Remarkably, CVB3 3A-H57Y could replicate its genome in the absence of detectable ROs when PI4KB was inhibited. Under these conditions, viral RNA synthesis was observed instead at a cellular organelle, the Golgi apparatus, which challenges the notion that ROs are essential for the exponential phase of genome replication. Golgi disintegration and RO formation did eventually occur under PI4KB inhibition, which suggests that PI4KB activity is not fundamentally required for RO biogenesis, but expedites the process. The delay in RO formation under PI4KB inhibition was exploited to experimentally test the hypothesis that ROs shield viral RNA from cytoplasmic sensors of the innate immune system. Our results suggest that, in addition to being dispensable for viral RNA synthesis, enterovirus ROs do not play a pivotal role in suppression of the innate antiviral response pathways.

RESULTS

CVB3 3A-H57Y RO formation is impaired under PI4KB inhibition

First, we set out to study the morphology of the ROs induced by CVB3 3A-H57Y under conditions where PI4KB is not inhibited. Infected BGM cells were prepared for electron microscopy (EM) by high-pressure freezing and freeze-substitution at different times post-infection and analysed for the presence of membrane modifications. The first ROs induced by CVB3 3A-H57Y were detected at 5 hours post infection (hpi). At this stage single-membrane tubules were predominant,

interspersed with double-membrane vesicles (DMVs) (Fig. 1A). The emergence of ROs coincides with disintegration of the Golgi apparatus in wt infection (5) and, concordantly, the Golgi apparatus was not observed in cell sections that contained ROs at any time point in this analysis. Later in infection tubules had largely transformed into DMVs (Fig. 1A, 6 hpi) and into multilamellar structures (Fig. 1A, 7 hpi). This progression closely reflects observations of wt CVB3 RO development with regard to both the specific morphologies induced and the time frame over which they develop (5), (Fig. S1A). Together, these results indicate that the 3A-H57Y substitution does not affect RO development or their general architecture.

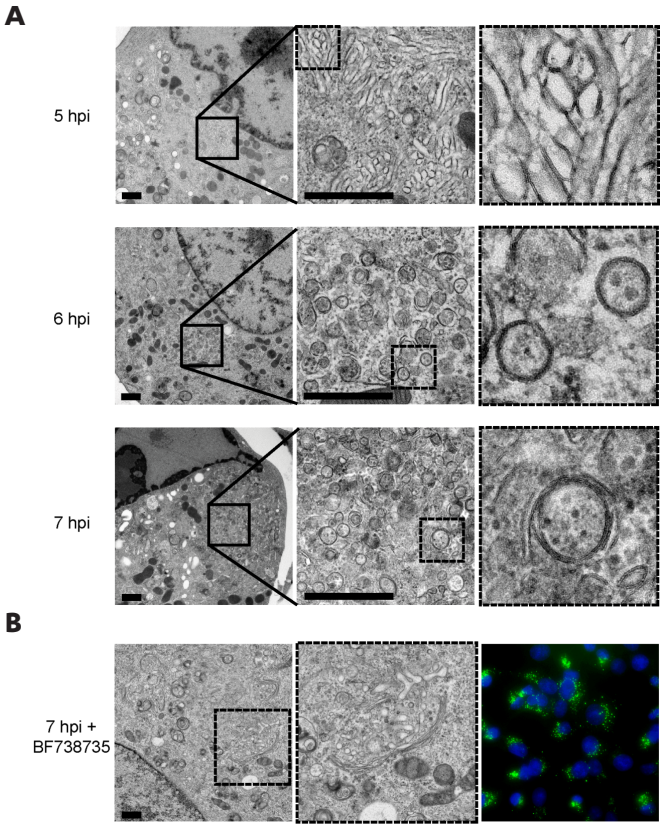


Figure 1. CVB3 3A-H57Y RO formation is impaired under PI4KB inhibition. A, B) BGM cells infected with CVB3 3A-H57Y (MOI 50). A) Cells fixed for EM analysis at early (5 hpi), intermediate (6 hpi) or late (7 hpi) stages of infection show the progression in RO development. B) ROs were not observed in EM cell sections (up to 8 hpi, n = 153) from cells treated with BF738735. (Left) An example of the Golgi apparatus in cells fixed at 7 hpi. (Right) Parallel immunofluorescence data (dsRNA (green) and nuclear stain (blue). Scale bars, 1 µm. See also Figs. S1 and S2.

Next, we investigated the effect of PI4KB inhibition on RO development during CVB3 3A-H57Y infection. To determine suitable time points for EM analysis of cells infected in the presence of a PI4KB inhibitor, we first measured viral replication in the presence of BF738735, a potent and specific PI4KB inhibitor without overt cytotoxicity (a.k.a. Compound 1; (9, 20)). Unlike CVB3 wt (Fig. S2A), CVB3 3A-H57Y was resistant to BF738735 (Fig. S2B), although its replication was nevertheless delayed and impaired in the presence of BF738735 with regard to both viral RNA (vRNA) and infectious

progeny virus. This is in agreement with observations using other PI4KB inhibitors (e.g. PIK93; (19)). To examine whether the impairment of replication upon PI4KB inhibition was the consequence of a decrease in the number of infected cells and/or a reduced level of vRNA replication, we collected cells infected with EGFP-CVB3 3A-H57Y at different time points post infection and analysed them with flow cytometry. PI4KB inhibition reduced the number of CVB3 3A-H57Y-infected cells (by ~3-fold), delayed replication (by ~1-2 h), and limited viral protein production, as reflected by reduced EGFP levels (Fig. S2C). These results indicate that the PI4KB inhibitor imposes a critical barrier to CVB3 3A-H57Y replication in a subpopulation of cells, and reduces the efficiency of replication in those cells where infection is established.

Based on the growth curve analysis, cells were fixed and processed for EM between 5 and 8 hpi, as this period encompasses the exponential phase of vRNA replication for CVB3 3A-H57Y under PI4KB inhibition. Remarkably, while ROs were detected at a frequency of ~50% in EM cell-sections from infections in the absence of PI4KB inhibitor (n = 43 cell-sections assessed at 6 hpi), neither archetypal enterovirus ROs (i.e. clusters of single-membrane tubules and/or DMVs) nor cellular membranes with atypical morphologies were detected in cells infected under PI4KB inhibition (n = 153 cell-sections), even at late time points (7-8 hpi, n = 47 cell-sections, example shown in Fig. 1B). Seemingly intact Golgi cisternae were apparent in these cells and were detected at a frequency similar to that of mock-infected or BF738735-treated cells (Fig. S1B and C respectively). Corresponding immunofluorescence microscopy data showed a high percentage of cells positive for dsRNA labelling, confirming that the lack of membrane modifications in the EM analysis was not simply due to a low number of infected cells (Fig. 1B, right). These data show that RO development is impaired by PI4KB inhibition, and suggest that replication may be taking place instead at a cellular organelle.

CVB3 3A-H57Y replicates its genome at the Golgi apparatus under PI4KB inhibition

As an initial indicator of the replication site under PI4KB inhibition, we performed immunofluorescence microscopy on infected cells (Fig. 2A). Cells were fixed at 5 hpi in the absence of inhibitor, and at 6 hpi in the presence of inhibitor given the delay in replication. Similar to findings for wt virus (8, 19), both 3A and dsRNA were detected throughout the cytoplasm in cells infected with CVB3 3A-H57Y in the absence of PI4KB inhibition (Fig. 2A, left panels). Golgi disassembly could be readily visualized through the signal reduction and dispersion of the cis-Golgi marker GM130 and the trans-Golgi network marker TGN46, whereas the PI4KB signal overlapped with the 3A labelling. Upon PI4KB inhibitor treatment however, 3A and dsRNA were primarily confined to the perinuclear region (Fig. 2A, right panels). In wide-field images, the strength and distribution of GM130 and TGN46 signals were largely maintained and overlapped with the viral 3A signal. These results suggested that both the 3A-H57Y protein and dsRNA reside at the Golgi apparatus in the presence of inhibitor. To confirm that these observations were due to specific inhibition of PI4KB, the localisation of 3A-GFP was assessed using different PI4KB inhibitors. Similar to BF738735, enviroxime, GW5074 or PIK93 treatment resulted the accumulation of 3A specifically at the Golgi region, although confocal imaging revealed that 3A did not directly co-localise with the cis-Golgi marker GM130 (Fig. 2B).

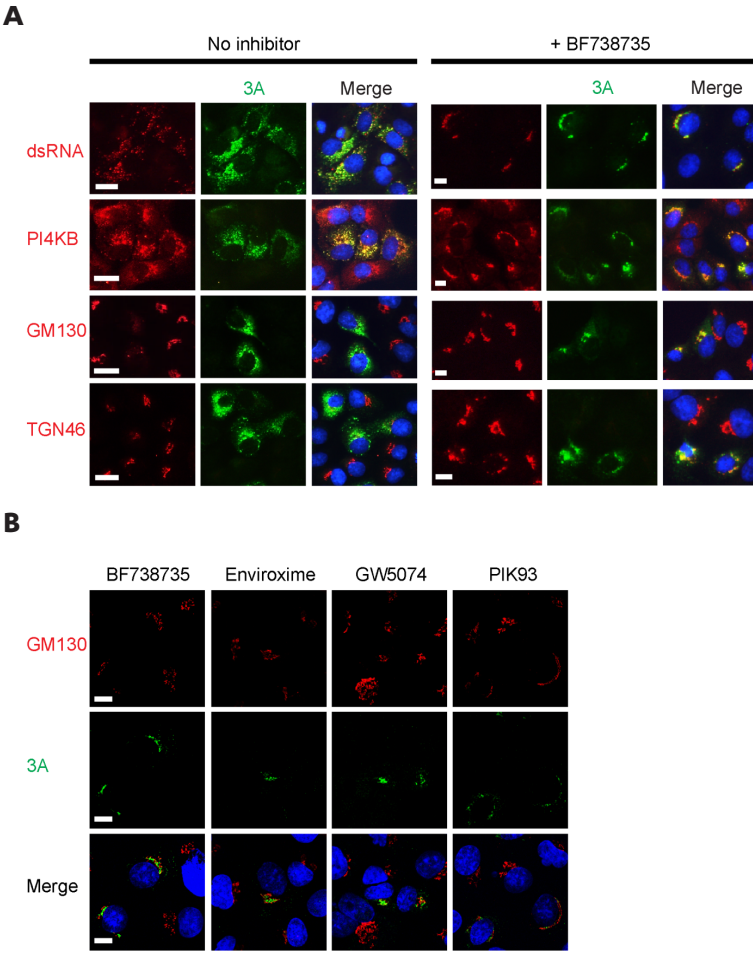


Figure 2. The 3A protein localises to the Golgi apparatus under PI4KB inhibition. A, B) BGM cells infected with CVB3 3A-H57Y (MOI 10). Untreated cells were fixed at 5 hpi ((A) left panels) and drug treated cells were fixed at 6 hpi ((A) right panels, and (B)). Fixed cells were labelled with the indicated antibodies and a nuclear stain (blue). Scale bars, 10 µm.

To unambiguously determine the subcellular location of the 3A-H57Y protein under PI4KB inhibitor treatment, correlative light and electron microscopy (CLEM) was performed. For this we employed the split-GFP system (21) to label the 3A-H57Y protein, in a similar approach to that previously reported for wt CVB3 (22). To produce a split-GFP CVB3 3A-H57Y mutant, the final beta sheet of GFP, i.e. strand 11, further referred to as GFP(S11), was introduced into the 3A-H57Y protein to produce CVB3 3A-H57Y(S11). Upon CVB3 3A-H57Y(S11) infection of BGM cells stably expressing the remaining portion of GFP (GFPS1-10), the two fragments of GFP self-assemble to produce GFP-tagged 3A-H57Y. GFP-tagged 3A-H57Y was then visualized by confocal microscopy before chemical fixation and processing for EM. Overlays of 3A-H57Y-GFP signal with the corresponding EM cell-sections fixed at 6 hpi revealed that the 3A protein localised specifically to the Golgi apparatus (Fig. 3A).
The presence of the 3A-H57Y protein at the Golgi apparatus suggested that vRNA replication occurs

at this compartment under PI4KB inhibition. To further investigate this, metabolic labelling was performed to detect newly synthesized vRNA in situ. Infected cells were pre-treated with 10 µg/ml dactinomycin to inhibit cellular transcription, and incubated with tritiated uridine for 45 minutes prior to fixation to label newly-synthesised vRNA. As a control, mock-infected cells underwent the same treatment. After processing for EM, radiolabelled uridine was detected by autoradiography (ARG). In cells infected with CVB3 3A-H57Y without PI4KB inhibition, abundant ARG signal was found in regions containing typical ROs (Fig. 3B). Although RO membranes in chemically fixed samples appeared somewhat distended in comparison to high-pressure frozen material (see Fig. 1), they were recognisable as clusters of single-membrane compartments (Fig. 3B, black arrowhead)

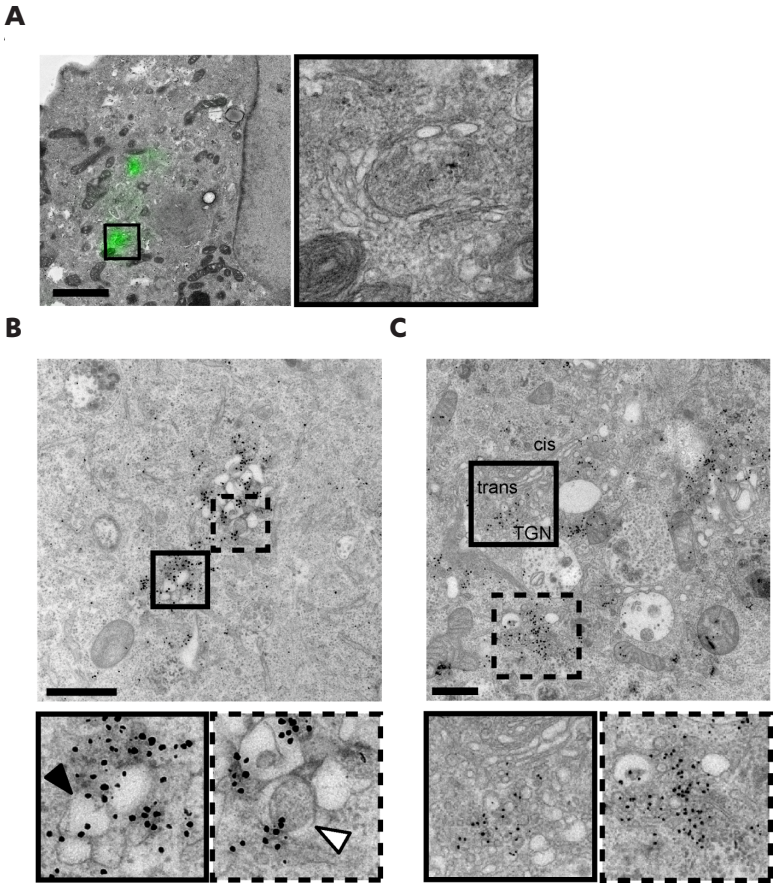


Figure 3. Replication under PI4KB inhibition occurs at the Golgi apparatus. A) BGM(GFPS1-10) cells infected with CVB3 3A-H57Y(S11) (MOI 7) monitored by live-cell LM, fixed at 6 hpi, and processed for CLEM. Overlay of the 3A-GFP signal at the time of fixation with the corresponding EM image (left). Inset highlights one of two 3A-GFP foci present in the image shown, both of which correspond to Golgi membranes. B, C) BGM cells infected with CVB3 3A-H57Y (MOI 50), metabolically labelled, fixed at 6 hpi (B) or 7 hpi (C), and processed for EM autoradiography to detect newly-synthesized vRNA (ARG). ARG signal is apparent as electron-dense grains. B) ROs positive for ARG signal were readily observed in the absence of BF738735. C) In cells treated with BF738735 ROs were not observed, and clusters of ARG signal were found exclusively at the Golgi apparatus. cis = Golgi apparatus cis face, trans = Golgi apparatus trans face, TGN = trans Golgi network. Scale bars, 2 µm (A) or 1 µm (B, C).

interspersed with DMVs (Fig. 3B, white arrowhead) that closely resemble the ROs observed in chemically fixed PV-infected (6, 23) or wt CVB3-infected cells (22). In CVB3 3A-H57Y-infected cells treated with PI4KB inhibitor and fixed at 7 hpi ROs were not observed (n = 148 cell sections), and abundant ARG signal was found at the Golgi apparatus (Fig. 3C), with the vast majority of signal localising to the trans-side of the Golgi apparatus and trans-Golgi network rather than the Golgi cisternae. This demonstrates that, under PI4KB inhibition, CVB3 3A-H57Y can replicate its genome

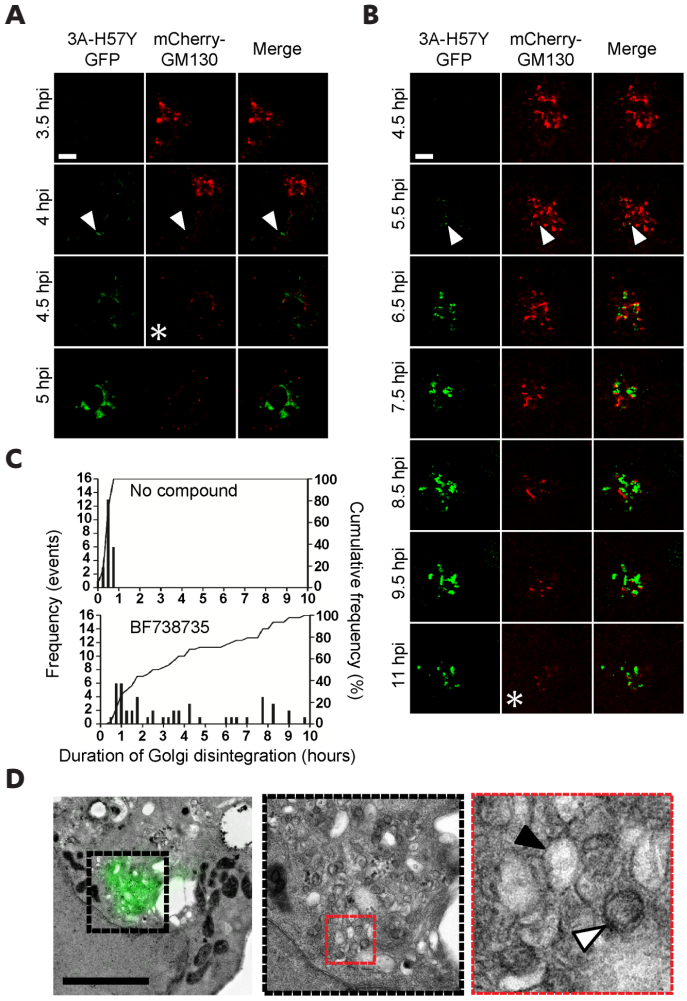


Fig. 4. Golgi disintegration during CVB3 3A-H57Y infection is prolonged under PI4KB inhibition, and ultimately results in RO formation. BGM(GFPS1-10) cells transduced with MLV mCherry-GM130, infected with CVB3 3A-H57Y(S11) (MOI 7) and imaged by live-cell confocal microscopy in the absence (A) or presence (B, D) of BF738735. Asterisks (A, B) denote completion of Golgi disintegration, evidenced by an entirely punctate mCherry-GM130 signal. A) Initial 3A-GFP signal was detected primarily at peripheral locations (arrowhead) and Golgi disintegration was typically complete within 25 minutes of its onset (C, upper graph n = 23 cells). B) In cells treated with BF738735, initial 3A-GFP signal was detected primarily at the Golgi apparatus (arrowhead). The Golgi disintegration duration was typically prolonged but highly variable (C, lower graph n = 48 cells). D) Cells were fixed for EM analysis at 9 hpi. The LM-EM overlay reveals single-membrane (black arrowhead) and double-membrane (white arrowhead) structures positive for 3A-GFP signal. Scale bars, 5 µm (D). See also Fig. S3.

in the absence of ROs on a seemingly intact Golgi apparatus.

Under PI4KB inhibition, ROs form late in CVB3 3A-H57Y-infected cells

Our results thus far show that, under PI4KB inhibition, CVB3 3A-H57Y replication is possible in association with an apparently intact cellular organelle. We next set out to establish whether PI4KB inhibition precludes Golgi disintegration and RO development entirely, or simply delays the process. Confocal microscopy of live cells expressing mCherry-GM130 was performed to monitor the Golgi apparatus across the course of CVB3 3A-H57Y(S11) infection, either with or without BF738735 treatment (Fig. 4A-C). In the absence of inhibitor, the process of Golgi fragmentation following CVB3 3A-H57Y(S11) infection was similar to that of wt split-GFP CVB3 infections (22). The onset of Golgi fragmentation occurred in conjunction with or even preceded 3A protein accumulation in the Golgi area, and Golgi disintegration was typically complete within 25 min (n = 23 cells) (Fig. 4A and C, upper graph). While in the absence of PI4KB inhibition early 3A signal was often located at peripheral foci (Fig. 4A arrowheads), under PI4KB inhibition the first 3A signal was often found in the Golgi region (Fig. 4B, arrowheads). Remarkably, the Golgi apparatus of most CVB3 3A-H57Y(S11) infected cells did disassemble during infections under PI4KB inhibition, but with markedly different dynamics. The onset of disintegration under these conditions did not coincide with 3A protein accumulation at the Golgi, but suffered a relative average delay of 30 minutes (n = 48 cells). Additionally, the time needed for Golgi disintegration was highly variable under PI4KB inhibition. In a minority of infected cells treated with BF738735 Golgi disassembly was as rapid as in untreated cells. However, in most cells the Golgi disintegration process was substantially prolonged (by up to 10 hours) under PI4KB inhibition (Fig. 4B and C, lower graph).

To determine whether Golgi disassembly under PI4KB inhibition was associated with the development of ROs, CLEM was performed on cells infected with split-GFP 3A-H57Y(S11) virus under BF738735 treatment and fixed at 9 hpi. While some cells retained seemingly intact Golgi membranes at this late stage in infection, in those cells lacking recognisable Golgi membranes the 3A-GFP signal was found at structures resembling typical early ROs (Fig. 4D, see Fig. 3A for comparison). As verified by immunofluorescence microscopy, PI4P did not accumulate in cells infected under PI4KB inhibition (Fig. S3), suggesting that the ROs that develop during CVB3 3A-H57Y infection under PI4KB inhibition do so independently of high PI4P levels.

PI4KB activity drives rapid Golgi disassembly and RO formation

RO formation is likely associated with the amount of viral protein produced in the cell, which in turn depends upon vRNA replication levels. Therefore, rather than the absence of high PI4P levels, the delay in CVB3 3A-H57Y vRNA replication under PI4KB inhibition could be solely responsible for impeding RO formation. Previously it was shown that replication-independent expression of PV non-structural proteins results in membranous structures reminiscent of ROs produced upon infection (24). Here, we engineered a replication-independent CVB3 expression system, which produces high amounts of viral proteins in the absence of vRNA replication. Hence, the inhibition of vRNA replication caused by PI4KB inhibition will not result in a delay in viral protein production in this setup. The system utilizes a CVB3 cDNA placed under the control of the bacteriophage T7 RNA polymerase, and is rendered replication-incompetent through modifications to the cloverleaf structure in the 5' untranslated region (UTR) of the viral genome that prevent replication via the

CVB3 polymerase (25). The 3A-H57Y substitution was introduced into this replication-incompetent CVB3 cDNA. Transfection of the CVB3 3A-H57Y cDNA plasmid in HuH-7/T7 cells, which stably express the T7 RNA polymerase, resulted in the expression of individual viral proteins whose amounts were not affected by the addition of PI4KB inhibitor (Fig. S4). Immunofluorescence analysis of transfected cells showed that the first 3A signal could be detected as early as 3 h post transfection (hpt), but without significant effects on the Golgi apparatus. In the absence of PI4KB inhibitor, Golgi disintegration was observed from 4 hpt onwards, as evidenced by the change in GM130 signal in transfected cells (Fig. 5A, upper panels). Under PI4KB inhibition Golgi disintegration was delayed by ~1 h (Fig. 5A middle and lower panels). While Golgi disintegration in the replication-independent system is more rapid than during infection (see Fig. 4), most likely because of the high protein expression levels generated with this system, these data nevertheless demonstrate that in cells with equal levels of viral proteins, PI4KB inhibition delays enterovirus-induced Golgi apparatus disassembly. To determine the contribution of the 3A-H57Y substitution to (delayed) Golgi disassembly, we examined whether the wt CVB3 cDNA could also induce Golgi disassembly under PI4KB inhibition in the replication-independent system. The results closely resembled those obtained for CVB3 3A-H57Y cDNA both with and without PI4KB inhibition (Fig. 5B). This demonstrates that the 3A-H57Y substitution does not affect Golgi disintegration.

Altogether, these findings strongly suggest that enterovirus RO biogenesis is driven by PI4KB activity.

The 3A-H57Y substitution rectifies a proteolytic polyprotein processing impairment induced by PI4KB inhibition

Another important step in the enterovirus replication cycle that relies on membranes is the proteolytic processing of the polyprotein by the viral proteases (26). Proteolytic polyprotein processing is a co- and post-translational event mediated by the viral proteinases 2Apro, 3Cpro, and 3CDpro. These proteinases catalyse a cascade of cleavages in cis and in trans that liberate individual capsid proteins, as well as replication proteins and their precursors (e.g. 2BC, 3AB and 3CD). Recent studies indicate that alterations to the lipid composition of membranes during PV infection impact polyprotein processing efficiency (27-29). Given that wt virus replication is abolished under PI4KB inhibition, we used the replication-independent CVB3 expression system to study the effects of PI4KB inhibition on polyprotein processing. Cells were lysed at 16 hours post transfection (hpt) and processed for Western blot analysis. PI4KB inhibition led to a relative accumulation of 3AB and a reduction in 3A for the wt polyprotein (Fig 5C, left). Remarkably, the 3A-H57Y substitution rectified this impaired polyprotein processing, as the relative levels of 3AB and 3A were not affected by PI4KB inhibition (Fig. 5C, right). PI4KB inhibition did not affect levels of 3CD or 3D. Together, these results demonstrate that PI4KB activity is important for proteolytic processing at the 3A-3B junction, but not at the 3C-3D junction (nor at the 2C-3A and 3B-3C junctions). The 3A-H57Y substitution restores processing to the level detected in the absence of inhibitor, which may point to a potential strategy of the mutant virus to escape PI4KB inhibition.

The delay in RO formation under PI4KB inhibition does not elicit a strong antiviral response

One of the proposed advantages of ROs is that they may shield vRNA products against viral RNA sensors present in the cytoplasm, such as MDA5, RIG-I, and PKR. Given that CVB3 3A-H57Y is

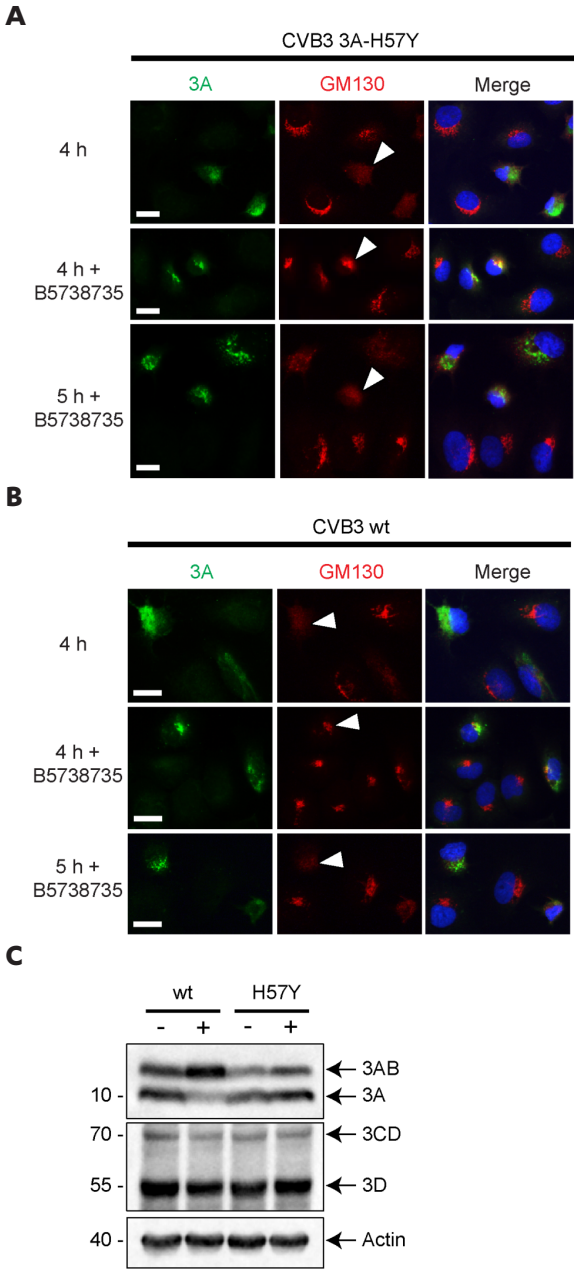


Figure 5. Effect of PI4KB inhibition on enterovirus-induced Golgi disintegration and proteolytic polyprotein processing in a replication-independent CVB3 system. HuH-7/T7 cells transfected with CVB3 3A-H57Y or wt CVB3 cDNA under the control of a T7 promoter, both rendered replication-incompetent by altering the 5'UTR of the genome. Where indicated, cells were treated with BF738735. A, B) Cells fixed at 4 h or 5 h post-transfection and labelled for 3A (green) and GM130 (red) alongside a nuclear stain (blue). Representative 3A-positive cells are indicated (arrowheads). Scale bars, 20 µm. C) Western blot analysis of lysates from cells at 16 h post-transfection using antibodies against 3A or 3D. Actin was used as a loading control. See also Fig. S4

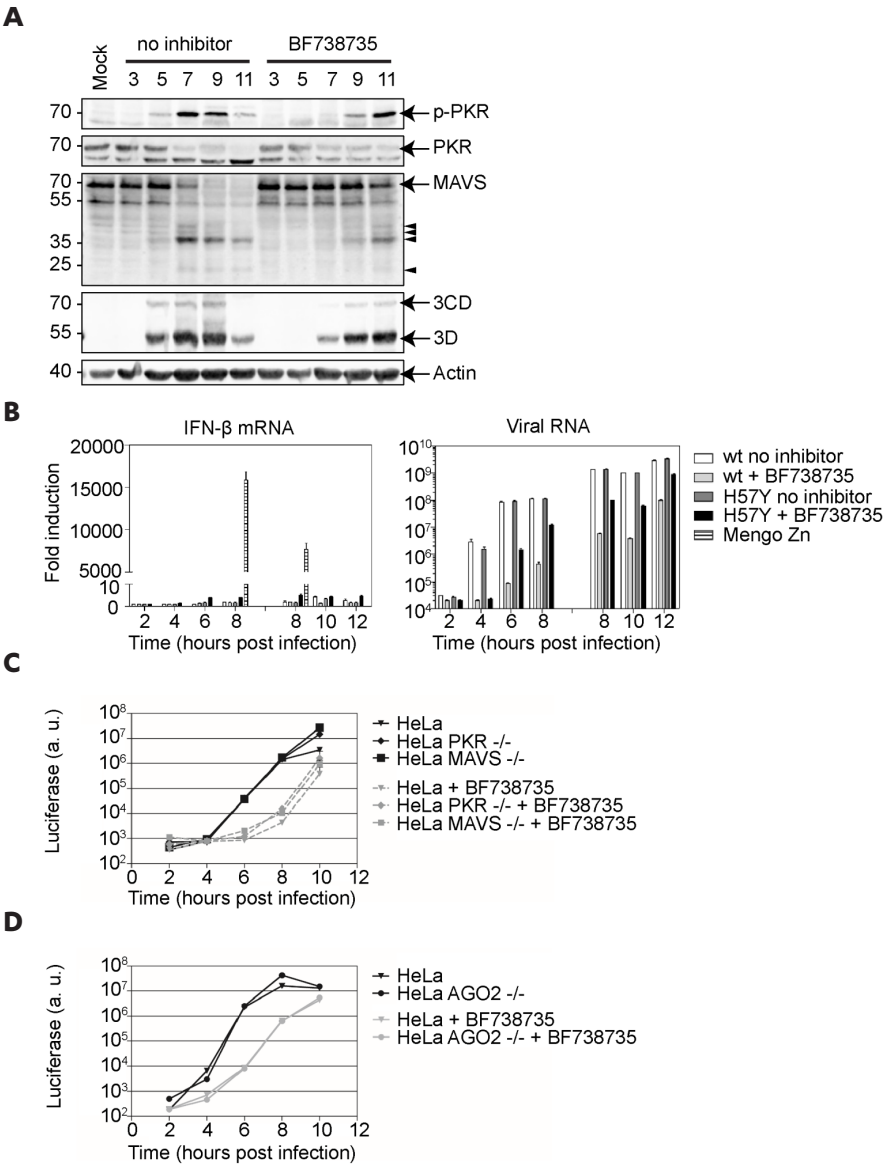


Fig. 6. Innate antiviral responses during CVB3 3A-H57Y infection. Cells infected and treated with BF738735 where indicated. A) HeLa cells infected with CVB3 3A-H57Y (MOI 50) were lysed for Western blot analysis at the indicated time points. Band sizes (in kDa), full-length proteins (arrows), and putative cleavage products (arrowheads) are indicated. B) HeLa cells infected with CVB3 wt or CVB3 3A-H57Y (MOI 10). Total RNA was isolated from cells and subjected to reverse transcription-quantitative PCR for interferon-b (IFN-b). Mengo Zn, whose L protein contains substitutions that render it unable to suppress IFN-b induction, was included as a positive control (left graph). Viral RNA levels were determined by quantitative RT-PCR (right graph). Data were normalized to actin mRNA levels. Results are expressed as fold induction relative to quantities in mock-infected cells. Two independent experiments are shown, ranging from 2-8 hpi and 8-12 hpi. C, D) Cells were infected with CVB3-Rluc 3A-H57Y (MOI 0.01) and lysed to determine the intracellular luciferase levels. Values represent mean values of triplicates ± standard error of the means. See also Figs. S5 and S6.

able to replicate its genome at the Golgi apparatus under PI4KB inhibition, vRNA products may be more accessible and better detected in this situation, thereby triggering an antiviral response that might limit or delay replication. To investigate whether viral dsRNA is better sensed under PI4KB inhibition, we studied the activation status of the cytoplasmic RNA sensor PKR. Western blot analyses were performed on infected cell lysates to assess viral protein levels in parallel with dsRNA-activated, phosphorylated PKR (p-PKR). The first appearance and the final levels of viral proteins were delayed and reduced respectively under PI4KB inhibition, which is in agreement with the observed reduction in the proportion of infected cells and the decrease in viral protein per cell (see Fig. S2C). Nevertheless, p-PKR emerged concomitantly with the accumulation of viral proteins both in the presence and absence of PI4KB inhibitor (Fig. 6A), suggesting that delayed RO formation under PI4KB inhibition does not lead to premature activation of PKR.

Another innate antiviral response that is activated upon sensing of vRNA products is the type I interferon (IFN-a/b) pathway. Enteroviruses counteract the transcription of IFN-a/b genes by cleaving components in the signalling pathways that control their activation, such as MDA5 (30) and its downstream adaptor MAVS (30, 31). The altered location of genome replication under PI4KB inhibition may influence the ability of the viral proteinases to cleave these components. However, we found that the appearance of MAVS degradation products in infected cell lysates coincided with the accumulation of viral proteins irrespective of the presence of PI4KB inhibitor (Fig. 6A). Furthermore, qPCR analysis showed that no substantial IFN-b response was triggered in infected cells in both conditions (Fig. 6B). Together, these results indicate that the delayed formation of ROs during infection does not accelerate cellular sensing of viral dsRNA, nor does it affect the ability of the viral proteinases to cleave MAVS.

As a complementary approach to investigate whether the delay in replication in the presence of PI4KB inhibitor is related to activation of innate antiviral responses, the level of CVB3 3A-H57Y replication was determined in cells lacking sensors of these pathways. Knock-out cells for PKR or MAVS, generated with CRISPR-Cas9 technology, were infected with CVB3 wt or 3A-H57Y that also encode Renilla luciferase as a sensitive measure to quantify the level of viral replication. In the absence of inhibitor, CVB3 3A-H57Y replicated to a similar extent in HeLa, HeLa PKR -/-, or HeLa MAVS-/- cells (Fig. 6C and S6). In the presence of PI4KB inhibitor, CVB3 3A-H57Y replication was delayed not only in HeLa cells, but also in PKR-/- or MAVS-/- cells. Thus, replication under PI4KB inhibition was not significantly increased in PKR-/- or MAVS-/- cells compared to parental HeLa cells. Similar results were obtained in U2OS cells, another human cell line (Fig. S5A and S6).

An alternative strategy employed by some eukaryotes, such as plants, worms, and insects, in response to viral infections is RNA interference (RNAi), although whether RNAi is an antiviral mechanism in mammalian cells remains controversial (32). In the RNAi pathway, the cytoplasmic sensor Dicer cleaves viral dsRNA into viral siRNAs, which are loaded by Argonaute-2 (AGO2) into the RNA-induced silencing complex (RISC) in order to degrade vRNA (33). Recently, it was reported that replication of the picornavirus EMCV was enhanced in mammalian somatic cells that lacked AGO2 (34). To investigate whether the delay in CVB3 3A-H57Y replication in the presence of PI4KB inhibitor is due to triggering of antiviral RNAi, we studied its replication kinetics in HeLa and HEK293T cells that lacked AGO2. Similar to our findings in MAVS and PKR knockout cell lines, the delay in replication under PI4KB inhibition was not alleviated in cells lacking AGO2 (Fig. 6D, S5B).

Altogether, these data suggest that the delay in CVB3 3A-H57Y replication under PI4KB inhibition

is not caused by premature triggering of innate antiviral responses as result of impaired RO biogenesis.

AUTHOR CONTRIBUTIONS

Conceptualization: CEM, HMvdS, MB, FJMvK; Investigation: CEM, HMvdS, HRL, RWALL, QF, MW, GJO, MB; Writing: CEM, HMS, MB, FJMvK; Reviewing and editing of the manuscript: CEM, HMS, RPvR, AJK, EJS, MB, FJMvK; Visualization: CEM, HMS; Supervision: HMS, EJS, AJK, RPvR, MB, FJMvK; Funding Acquisition: HMvdS, EJS, RPvR, AJK, MB, FJMvK.

ACKNOWLEDGEMENTS

The authors would like to thank Huib Rabouw for excellent assistance with flow cytometry, and the LUMC light microscopy facility. This work was supported by grants from the Netherlands Organisation for Scientific Research (NWO-VENI-863.12.005 to HMvdS, NWO-VICI-91812628 to FJMvK, ERASysApp project 'SysVirDrug' ALW project 832.14.003 to FJMvK, NWO-MEERVOUD 863.10.003 to MB, NWO-CW TOP 700.57.301 to EJS), and the European Union (7th Framework: EUVIRNA Marie Curie Initial Training Network grant agreement 264286 to FJMvK,; European Research Council Consolidator Grant CoG 615680 to RPvR, Horizon 2020: Marie Skłodowska-Curie ETN 'ANTIVIRALS' grant agreement 642434 to FJMvK). The funders had no role in study design, data collection and interpretation, or the decision to submit the work for publication.

EXPERIMENTAL PROCEDURES

Replication-independent system. HuH-7/T7 cells were seeded in 24-well plates containing glass coverslips. The next day, the cells were lipofectamine transfected with CVB3 cDNA rendered replication-deficient through modifications to the cloverleaf structure in the 5' untranslated region (UTR) of the viral genome (25). One hour later, the medium was replaced with fresh medium. At indicated hours post-transfection, cells were washed and either fixed for immunofluorescence or lysed for Western Blot analysis.

Live cell imaging. BGM(GFPS1-10) cells were grown in glass-bottom 4-chamber 35-mm dishes (CELLviewTM) to ~35% confluency and transduced with MLV mCherry-GM130 particles described before (see (22)). Infection with CVB3 3A-H57Y(S11) was carried out 18-24 hours later. Prior to imaging cells were washed with Fluorobrite medium (Thermo Fisher Scientific) supplemented with 8% fetal calf serum (FCS) and 25 mM HEPES. Cells were maintained in a live-cell imaging chamber at 37°C and 5% CO2. Imaging was carried out from ~2.5 (hpi) using a Leica SP5 confocal microscope. Positions of interest (xyz) were marked and imaged sequentially at 5 minute intervals.

High-pressure freezing and freeze substitution. BGM cells were grown on sapphire discs and infected with CVB3 or CVB3 3A-H57Y and refreshed at 1 hpi with medium supplemented with 25 mM HEPES buffer with or without 1 µm BF738735. Cells were high-pressure frozen using a Leica EM PACT2 at different time points post infection. The instruments and procedures used for freeze-substitution, epoxy resin infiltration and polymerisation were identical to those described in (5). Sections of 70 nm were then prepared for electron microscopy and post-stained with uranyl

acetate and lead citrate.

Correlative light and electron microscopy (CLEM) preparation. BGM (GFPS1-10) cells were cultured in gridded 8-well chamber µ-slides (Ibidi) ahead of infection with CVB3 3A-H57Y(S11). Just prior to imaging cells were treated with 100 nM Mitotracker® Deep Red FM for 30 minutes. Live-cell imaging was carried out to monitor the levels of 3A-H57Y-GFP. High resolution (1024x1024) z-stacks were collected of cells of interest just prior to fixation. To aid in the relocation of these cells for CLEM, tile scan overviews were taken and the positions of cells relative to nearby grid co-ordinates were recorded. Following imaging by live-cell light microscopy (LM), cells were prepared for electron microscopy as described previously (see (22)). EM images were collected of cells previously identified by LM. The EM and LM data for each cell were overlaid using the Mitotracker® Deep Red FM signal (LM images) and corresponding mitochondria (EM images) as a guide for image transformation.

Metabolic labelling and autoradiography. A subconfluent layer of BGM cells was grown in 35 mm dishes (Corning) and infected with CVB3 or CVB3 3A-H57Y at MOI 5. Cells were incubated with dactinomycin for 1 hour prior to a 45-minute labelling with tritiated uridine ([5-3H], 1 mCi/ml) (Perkin Elmer). Cells were processed for EM as described in (22). Sections of 50 nm were collected and post stained with lead citrate and uranyl acetate, then prepared for autoradiography (as described in (51)).

Electron microscopy. Images were collected on an FEI Tecnai12 BioTWIN or TWIN electron microscope at 120 kV using an Eagle 4k slow-scan CCD camera (FEI) or OneView 4k high frame-rate camera (Gatan) respectively. For the collection of larger EM datasets, meshes of overlapping areas across the grid were taken that were later stitched into a single composite image (as described in (52)).

REFERENCES

1. Romero-Brey I, Bartenschlager R. 2014. Membranous Replication Factories Induced by Plus-Strand RNA Viruses. Viruses-Basel 6:2826-2857.
2. Paul D, Bartenschlager R. 2013. Architecture and biogenesis of plus-strand RNA virus replication factories. World J Virol 2:32-48.
3. Schulz KS, Mossman KL. 2016. Viral Evasion Strategies in Type I IFN Signaling - A Summary of Recent Developments. Front Immunol 7:498.
4. White JP, Lloyd RE. 2012. Regulation of stress granules in virus systems. Trends in Microbiology 20:175-183.
5. Limpens RWAL, van der Schaar HM, Kumar D, Koster AJ, Snijder EJ, van Kuppeveld FJM, Barcena M. 2011. The Transformation of Enterovirus Replication Structures: a Three-Dimensional Study of Single- and Double-Membrane Compartments. mBio 2.
6. Belov GA, Nair V, Hansen BT, Hoyt FH, Fischer ER, Ehrenfeld E. 2012. Complex Dynamic Development of Poliovirus Membranous Replication Complexes. Journal of Virology

86:302-312.
7. Suhy DA, Giddings TH, Jr., Kirkegaard K. 2000. Remodeling the endoplasmic reticulum by poliovirus infection and by individual viral proteins: an autophagy-like origin for virus-induced vesicles. J Virol 74:8953-65.
8. Hsu NY, Ilnytska O, Belov G, Santiana M, Chen YH, Takvorian PM, Pau C, van der Schaar H, Kaushik-Basu N, Balla T, Cameron CE, Ehrenfeld E, van Kuppeveld FJM, Altan-Bonnet N. 2010. Viral Reorganization of the Secretory Pathway Generates Distinct Organelles for RNA Replication. Cell 141:799-811.
9. van der Schaar HM, Leyssen P, Thibaut HJ, de Palma A, van der Linden L, Lanke KH, Lacroix C, Verbeken E, Conrath K, Macleod AM, Mitchell DR, Palmer NJ, van de Poel H, Andrews M, Neyts J, van Kuppeveld FJ. 2013. A novel, broad-spectrum inhibitor of enterovirus replication that targets host cell factor phosphatidylinositol 4-kinase IIIbeta. Antimicrob Agents Chemother 57:4971-81.
10. Greninger AL, Knudsen GM, Betegon M, Burlingame AL, Derisi JL. 2012. The 3A protein from multiple picornaviruses utilizes the golgi adaptor protein ACBD3 to recruit PI4KIIIbeta. J Virol 86:3605-16.
11. Altan-Bonnet N, Balla T. 2012. Phosphatidylinositol 4-kinases: hostages harnessed to build panviral replication platforms. Trends Biochem Sci 37:293-302.
12. Dorobantu CM, Albulescu L, Harak C, Feng Q, van Kampen M, Strating JRPM, Gorbalenya AE, Lohmann V, van der Schaar HM, van Kuppeveld FJM. 2015. Modulation of the Host Lipid Landscape to Promote RNA Virus Replication: The Picornavirus Encephalomyocarditis Virus Converges on the Pathway Used by Hepatitis C Virus. Plos Pathogens 11.
13. Clayton EL, Minogue S, Waugh MG. 2013. Mammalian phosphatidylinositol 4-kinases as modulators of membrane trafficking and lipid signaling networks. Progress in Lipid Research 52:294-304.
14. De Matteis MA, Wilson C, D'Angelo G. 2013. Phosphatidylinositol-4-phosphate: the Golgi and beyond. Bioessays 35:612-22.
15. Mesmin B, Bigay J, Moser von Filseck J, Lacas-Gervais S, Drin G, Antonny B. 2013. A four-step cycle driven by PI(4)P hydrolysis directs sterol/PI(4)P exchange by the ER-Golgi tether OSBP. Cell 155:830-43.
16. Arita M. 2014. Phosphatidylinositol-4 kinase III beta and oxysterol-binding protein accumulate unesterified cholesterol on poliovirus-induced membrane structure. Microbiology and Immunology 58:239-256.
17. Strating JRPM, van der Linden L, Albulescu L, Bigay J, Arita M, Delang L, Leyssen P, van der Schaar HM, Lanke KHW, Thibaut HJ, Ulferts R, Drin G, Schlinck N, Wubbolts RW, Sever N, Head SA, Liu JO, Beachy PA, De Matteis MA, Shair MD, Olkkonen VM, Neyts J, van Kuppeveld FJM. 2015. Itraconazole Inhibits Enterovirus Replication by Targeting the Oxysterol-Binding Protein. Cell Reports 10:600-615.
18. Roulin PS, Lotzerich M, Torta F, Tanner LB, van Kuppeveld FJ, Wenk MR, Greber UF. 2014. Rhinovirus uses a phosphatidylinositol 4-phosphate/cholesterol counter-current for the formation of replication compartments at the ER-Golgi interface. Cell Host Microbe 16:677-90.
19. van der Schaar HM, van der Linden L, Lanke KH, Strating JR, Purstinger G, de Vries E, de

Haan CA, Neyts J, van Kuppeveld FJ. 2012. Coxsackievirus mutants that can bypass host factor PI4KIIIbeta and the need for high levels of PI4P lipids for replication. Cell Res 22:1576-92.
20. MacLeod AM, Mitchell DR, Palmer NJ, Van de Poel H, Conrath K, Andrews M, Leyssen P, Neyts J. 2013. Identification of a series of compounds with potent antiviral activity for the treatment of enterovirus infections. ACS Med Chem Lett 4:585-9.
21. Cabantous S, Terwilliger TC, Waldo GS. 2005. Protein tagging and detection with engineered self-assembling fragments of green fluorescent protein. Nature Biotechnology 23:102-107.
22. van der Schaar HM, Melia CE, van Bruggen JA, Strating JR, van Geenen ME, Koster AJ, Barcena M, van Kuppeveld FJ. 2016. Illuminating the Sites of Enterovirus Replication in Living Cells by Using a Split-GFP-Tagged Viral Protein. mSphere 1.
23. Dales S, Eggers HJ, Tamm I, Palade GE. 1965. Electron Microscopic Study of the Formation of Poliovirus. Virology 26:379-89.
24. Belov GA, Feng Q, Nikovics K, Jackson CL, Ehrenfeld E. 2008. A Critical Role of a Cellular Membrane Traffic Protein in Poliovirus RNA Replication. Plos Pathogens 4.
25. Langereis MA, Feng Q, Nelissen FH, Virgen-Slane R, van der Heden van Noort GJ, Maciejewski S, Filippov DV, Semler BL, van Delft FL, van Kuppeveld FJ. 2014. Modification of picornavirus genomic RNA using 'click' chemistry shows that unlinking of the VPg peptide is dispensable for translation and replication of the incoming viral RNA. Nucleic Acids Res 42:2473-82.
26. Molla A, Hellen CU, Wimmer E. 1993. Inhibition of proteolytic activity of poliovirus and rhinovirus 2A proteinases by elastase-specific inhibitors. J Virol 67:4688-95.
27. Ilnytska O, Santiana M, Hsu NY, Du WL, Chen YH, Viktorova EG, Belov G, Brinker A, Storch J, Moore C, Dixon JL, Altan-Bonnet N. 2013. Enteroviruses harness the cellular endocytic machinery to remodel the host cell cholesterol landscape for effective viral replication. Cell Host Microbe 14:281-93.
28. Ford Siltz LA, Viktorova EG, Zhang B, Kouiavskaia D, Dragunsky E, Chumakov K, Isaacs L, Belov GA. 2014. New small-molecule inhibitors effectively blocking picornavirus replication. J Virol 88:11091-107.
29. Arita M. 2016. Mechanism of Poliovirus Resistance to Host Phosphatidylinositol-4 Kinase III beta Inhibitor. Acs Infectious Diseases 2:140-148.
30. Feng Q, Langereis MA, Lork M, Nguyen M, Hato SV, Lanke K, Emdad L, Bhoopathi P, Fisher PB, Lloyd RE, van Kuppeveld FJ. 2014. Enterovirus 2Apro targets MDA5 and MAVS in infected cells. J Virol 88:3369-78.
31. Mukherjee A, Morosky SA, Delorme-Axford E, Dybdahl-Sissoko N, Oberste MS, Wang T, Coyne CB. 2011. The coxsackievirus B 3C protease cleaves MAVS and TRIF to attenuate host type I interferon and apoptotic signaling. PLoS Pathog 7:e1001311.
32. Luna JM, Wu X, Rice CM. 2016. Present and not reporting for duty: dsRNAi in mammalian cells. EMBO J 35:2499-2501.
33. tenOever BR. 2016. The Evolution of Antiviral Defense Systems. Cell Host Microbe 19:142-9.
34. Li Y, Basavappa M, Lu J, Dong S, Cronkite DA, Prior JT, Reinecker HC, Hertzog P, Han Y, Li WX, Cheloufi S, Karginov FV, Ding SW, Jeffrey KL. 2016. Induction and suppression of antiviral RNA interference by influenza A virus in mammalian cells. Nat Microbiol 2:16250.

35. van der Schaar HM, Dorobantu CM, Albulescu L, Strating JR, van Kuppeveld FJ. 2016. Fat(al) attraction: Picornaviruses Usurp Lipid Transfer at Membrane Contact Sites to Create Replication Organelles. Trends Microbiol 24:535-46.
36. Strating JR, van Kuppeveld FJ. 2017. Viral rewiring of cellular lipid metabolism to create membranous replication compartments. Curr Opin Cell Biol 47:24-33.
37. Xu K, Nagy PD. 2014. Expanding use of multi-origin subcellular membranes by positive-strand RNA viruses during replication. Curr Opin Virol 9:119-26.
38. Reghellin V, Donnici L, Fenu S, Berno V, Calabrese V, Pagani M, Abrignani S, Peri F, De Francesco R, Neddermann P. 2014. NS5A Inhibitors Impair NS5A-Phosphatidylinositol 4-Kinase III alpha Complex Formation and Cause a Decrease of Phosphatidylinositol 4-Phosphate and Cholesterol Levels in Hepatitis C Virus-Associated Membranes. Antimicrobial Agents and Chemotherapy 58:7128-7140.
39. Dorobantu CM, Albulescu L, Lyoo H, van Kampen M, De Francesco R, Lohmann V, Harak C, van der Schaar HM, Strating JR, Gorbalenya AE, van Kuppeveld FJ. 2016. Mutations in Encephalomyocarditis Virus 3A Protein Uncouple the Dependency of Genome Replication on Host Factors Phosphatidylinositol 4-Kinase IIIalpha and Oxysterol-Binding Protein. mSphere 1.
40. Reiss S, Rebhan I, Backes P, Romero-Brey I, Erfle H, Matula P, Kaderali L, Poenisch M, Blankenburg H, Hiet MS, Longerich T, Diehl S, Ramirez F, Balla T, Rohr K, Kaul A, Buhler S, Pepperkok R, Lengauer T, Albrecht M, Eils R, Schirmacher P, Lohmann V, Bartenschlager R. 2011. Recruitment and Activation of a Lipid Kinase by Hepatitis C Virus NS5A Is Essential for Integrity of the Membranous Replication Compartment. Cell Host & Microbe 9:32-45.
41. Albulescu L, Wubbolts R, van Kuppeveld FJ, Strating JR. 2015. Cholesterol shuttling is important for RNA replication of coxsackievirus B3 and encephalomyocarditis virus. Cell Microbiol 17:1144-56.
42. Burke JE, Inglis AJ, Perisic O, Masson GR, McLaughlin SH, Rutaganira F, Shokat KM, Williams RL. 2014. Structures of PI4KIIIbeta complexes show simultaneous recruitment of Rab11 and its effectors. Science 344:1035-8.
43. de Graaf P, Zwart WT, van Dijken RA, Deneka M, Schulz TK, Geijsen N, Coffer PJ, Gadella BM, Verkleij AJ, van der Sluijs P, van Bergen en Henegouwen PM. 2004. Phosphatidylinositol 4-kinasebeta is critical for functional association of rab11 with the Golgi complex. Mol Biol Cell 15:2038-47.
44. Dodd DA, Giddings TH, Jr., Kirkegaard K. 2001. Poliovirus 3A protein limits interleukin-6 (IL-6), IL-8, and beta interferon secretion during viral infection. J Virol 75:8158-65.
45. Cornell CT, Kiosses WB, Harkins S, Whitton JL. 2007. Coxsackievirus B3 proteins directionally complement each other to downregulate surface major histocompatibility complex class I. J Virol 81:6785-97.
46. Neufeldt CJ, Joyce MA, Van Buuren N, Levin A, Kirkegaard K, Gale M, Jr., Tyrrell DL, Wozniak RW. 2016. The Hepatitis C Virus-Induced Membranous Web and Associated Nuclear Transport Machinery Limit Access of Pattern Recognition Receptors to Viral Replication Sites. PLoS Pathog 12:e1005428.
47. Welsch S, Miller S, Romero-Brey I, Merz A, Bleck CK, Walther P, Fuller SD, Antony C, Krijnse-Locker J, Bartenschlager R. 2009. Composition and three-dimensional architecture of the

dengue virus replication and assembly sites. Cell Host Microbe 5:365-75.
48. Cortese M, Goellner S, Acosta EG, Neufeldt CJ, Oleksiuk O, Lampe M, Haselmann U, Funaya C, Schieber N, Ronchi P, Schorb M, Pruunsild P, Schwab Y, Chatel-Chaix L, Ruggieri A, Bartenschlager R. 2017. Ultrastructural Characterization of Zika Virus Replication Factories. Cell Rep 18:2113-2123.
49. Bienz K, Egger D, Pfister T, Troxler M. 1992. Structural and functional characterization of the poliovirus replication complex. J Virol 66:2740-7.
50. Lei X, Xiao X, Wang J. 2016. Innate Immunity Evasion by Enteroviruses: Insights into Virus-Host Interaction. Viruses 8.
51. Ginsel LA, Onderwater JJ, Daems WT. 1979. Resolution of a gold latensification-elon ascorbic acid developer for Ilford L4 emulsion. Histochemistry 61:343-6.
52. Faas FG, Avramut MC, van den Berg BM, Mommaas AM, Koster AJ, Ravelli RB. 2012. Virtual nanoscopy: generation of ultra-large high resolution electron microscopy maps. J Cell Biol 198:457-69.

SUPPLEMENTAL EXPERIMENTAL PROCEDURES

Cells. BGM, BGM(GFPS1-10) stably expressing GFP(S1-10) (described in (1)), HeLa R19, HEK293T, U2OS, and HuH-7-Lunet T7-BLR (HuH-7/T7) cells, and a cell pool stably expressing T7 RNA polymerase and blasticidin S-deaminase generously provided by R. Bartenschlager (University of Heidelberg, Heidelberg, Germany) ((2)), were maintained in Dulbecco's modified Eagle's medium (Gibco) supplemented with 10% fetal calf serum, penicillin, and streptomycin, and grown at 37°C in 5% CO2. The culture medium for HuH-77/T7 cells contained 10 µg/ml blasticidine, while that of BGM(GFPS1-10) cells contained 30 µg/ml puromycin.

Knock-out cells. HeLa PKR-/- cells have been described before (see (3)). U2OS PKR-/- were generated using the pCRISPR-hCas9-2xgRNA-Puro plasmid ((4)) with the same gRNAs as used for the HeLa PKR-/- cells, which target the kinase domain of PKR. To target human Ago2, gRNA encoding oligonucleotides cassettes (gRNA1: 5'-ACCGACCGCGTCTGCAATGTGACC-3' and 5'-AACGGTCACATTGCAGACGCGGTC-3', gRNA2: 5'-ACCGCCCATGTTTACAAGTCGGAC-3' and 5'-AACGTCCGACTTGTAAACATGGGC-3') were cloned into the SapI restriction sites of the pCRISPR-hCas9-2xgRNA-Puro plasmid. HEK293T Ago2-/- cells were kindly provided by K.W. Mulder (Radboud University Nijmegen Medical Center, Nijmegen, The Netherlands) and have been described previously (see (5)). To generate HeLa MAVS-/- and U2OS MAVS-/-, cells were co-transfected with two plasmids containing gRNA1 5'- GAATACCCTTCAGCGGCGGCC-3' and gRNA2 5'-GCTGTGAGCTAGTTGATCTCG-3'. Single-cell clones were generated using end-point dilutions. The knock-out was verified by sequence analysis of the genomic DNA and by Western Blot analysis (Fig. S7; HeLa Ago2-/- will be shown elsewhere by RPvR).

Viruses. Coxsackievirus B3 (CVB3) WT was obtained by transfecting in vitro-transcribed RNA derived from the p53CB3/T7 plasmid, which contains the cDNA of CVB3 strain Nancy driven by a T7 RNA polymerase promoter. The 3A-H57Y substitution was introduced in the cDNA clones of CVB3, Rluc-CVB3 and EGFP-CVB3 encoding Renilla luciferase or EGFP upstream of P1 ((6)), or the split-GFP-tagged CVB3 ((1)) using standard DNA cloning techniques. Virus titers were determined by end-

point titration analysis and expressed as 50% cell culture infectious dose (CCID50). A Mengovirus which lost its IFN-suppressing activities due to substitutions in the Zn-finger domain of the leader protein (Mengo Zn) has been described previously (see (7)). Virus titers were determined by end-point titration analysis and expressed as 50% cell culture infectious dose (CCID50).

Reagents. BF738735 (2-fluoro-4-(2-methyl-8-(3-(methylsulfonyl)benzylamino)imidazo[1,2-a] pyrazin-3-yl)phenol) ((8), (9)) was provided by Galapagos NV, used at a working concentration of 1 μM and added in all the experiments 1 hour after infection or mock-infection. Guanidine Hydrochloride (GuHCl) and GW5074 were purchased from Sigma and used at a working concentration of 30 μM and 2 mM respectively. Enviroxime has been previously described ((10)) and used at a concentration of 0.5 μg/ml (1.4 μM). PIK93 was provided by Dr K Shokat (University of California San Francisco, San Francisco, California, USA) and used at a concentration of 1 μM.

Antibodies. The rabbit antiserum and the mouse monoclonal antibody directed against the non-structural protein 3A were described previously (see (11), (12)). Rabbit antiserum against CVB3 3D was generously provided by C.E. Cameron (Pennsylvania State University, USA). Primary mouse monoclonal antibodies included anti-βactin (Sigma Aldrich), anti-GM130 (BD Biosciences), anti-dsRNA J2 (English & Scientific Consulting), and anti-PKR (Santa-Cruz). Primary rabbit polyclonal antibodies included anti-PI4KB (Millipore), anti-TGN46 (Novus Biologicals), anti-phospho-PKR (Abcam), and anti-MAVS (Cardif, Enzo Life Sciences). Alexa Fluor 594-conjugated goat-anti-rabbit IgG and Alexa Fluor 488-conjugated goat-anti-mouse IgG (Molecular Probes) were used as secondary antibodies for immunofluorescence microscopy. For Western Blot analysis, secondary antibody detection included IRDye goat anti-mouse or goat anti-rabbit (LI-COR).

Quantitative PCR. RNA was isolated from infected cells using a Nucleospin RNA kit (Machery-Nagel). cDNA was synthesized using random hexamers as primers with a TaqMan reverse transcription reagents kit (Roche). The cDNA was used for quantitative PCR with the forward primer 5'-CGTGGGGCTACAATCAAGTT-3', the reverse primer 5'-TAACAGGAGCTTTGGGCATC-3', and the LightCycler 480 SYBR Green I master kit (Roche) for 45 cycles (5 s at 95°C, 10 s at 60°C, and 20 s at 72°C) on a LightCycler 480 (Roche). Obtained Ct values were expressed as fold increase with the value at t = 2 h set as 1.

Flow cytometry. BGM cells were seeded in 24-well plates and infected with EGFP-CVB3 3A-H57Y the next day at different MOIs. Cells were released using trypsin, washed once in phosphate buffered saline (PBS), and fixed with 1% paraformaldehyde (PFA) in PBS. Cells were analyzed on FACS Canto (BD) using BD FACS Diva software.

Western Blot analysis. Virus-infected cells were collected in lysis buffer (50 mM TrisHCl pH 7.4, 150 mM NaCl, 1 mM EDTA, 1% Nonidet P-40, 0.05% SDS) and heated for 5 min at 95°C after addition of Laemmli sample buffer. Samples were run on polyacrylamide gels and transferred to a nitrocellulose membrane (Bio-Rad), which following blocking was incubated with primary antibodies overnight at 4˚C and secondary antibodies for 1 h at room temperature. Images of blots were acquired with Odyssey Imaging System (LI-COR).

Immunofluorescence microscopy. BGM cells grown on coverslips were infected with CVB3 WT or CVB3 3A-H57Y for 30-60 minutes, after which the inoculum was removed and fresh medium was added. At indicated time points post-infection, cells were fixed with paraformaldehyde and permeabilized with PBS containing 0.1% Triton X-100. Cells were then stained with primary and secondary antibodies and a nuclear stain (DAPI or Hoechst 33342). Wide-field imaging was

performed using either an Olympus BX60 or Leica DM5500 fluorescent microscope, and confocal imaging was performed with a Leica SpeII confocal microscope.

Replication-independent system. HuH-7/T7 cells were seeded in 24-well plates containing glass coverslips. The next day, the cells were transfected with cDNA of CVB3 rendered replication-deficient through modifications to the cloverleaf structure in the 5' untranslated region (UTR) of the viral genome ((4)) using Lipofectamine 2000 (Thermo Fisher Scientific) according to the manufacturer's protocol. One hour later, the medium was replaced with fresh medium. At indicated hours post-transfection, cells were washed and either fixed for immunofluorescence or lysed for Western Blot analysis.

Live cell imaging. BGM(GFPS1-10) cells were grown in glass-bottom 4-chamber 35-mm dishes (CELLviewTM) to ~35% confluency and transduced with MLV mCherry-GM130 particles described before ((1)). Infection with CVB3 3A-H57Y(S11) was carried out 18-24 hours later. In samples to be studied under PI4KB inhibition, infections were maintained in medium containing 1 µm BF735738 from 1 hpi and for the duration of imaging. Prior to imaging cells were washed with Fluorobrite medium (Thermo Fisher Scientific) supplemented with 8% fetal calf serum (FCS) and 25 mM HEPES. Imaging was carried out from ~2.5 (hpi) using a Leica SP5 confocal microscope equipped with a HyD detector and a 63x (1.4 NA) oil immersion objective, with the confocal pinhole adjusted to 1 airy unit for GFP emission (95.56 µm pinhole). Cells were maintained in a live-cell imaging chamber at 37°C and 5% CO2. Positions of interest (xyz) were marked and imaged sequentially at 5 minute intervals. Live-cell imaging data were processed in ImageJ and aligned using the StackReg plugin.

High-pressure freezing and freeze substitution. BGM cells were grown on sapphire discs and infected with CVB3 or CVB3 3A-H57Y and refreshed at 1 hpi with medium supplemented with 25 mM HEPES buffer. Cells were high-pressure frozen using a Leica EM PACT2 at different time points post infection. The instruments and procedures used for freeze-substitution, epoxy resin infiltration and polymerisation were identical to those described in (13). Briefly, samples were maintained in a Leica AFS2 at -90°C for 44h in a freeze substitution medium containing 10% H20, 2% osmium tetroxide and 1% anhydrous glutaraldehyde. The temperature was then raised to 0°C over a period of 22 hours through a series of controlled warming phases. Samples were washed with acetone, infiltrated with epoxy resin LX-112 (Ladd Research) and polymerised at 60°C. Sections of 70 nm were then prepared for electron microscopy and post-stained with uranyl acetate and lead citrate.

Correlative light and electron microscopy (CLEM). BGM(GFPS1-10) cells were cultured in gridded 8-well chamber µ-slides (Ibidi) ahead of infection with CVB3 3A-H57Y(S11). Cells were maintained in 1 µm BF735738 from 1 hpi in all incubation steps and for the duration of imaging. Just prior to imaging cells were treated with 100 nM Mitotracker® Deep Red FM for 30 minutes, then washed several times in Fluorobrite medium supplemented with 8% FCS and 25 mM HEPES. Images were collected using a Leica SP8 confocal microscope equipped with a HyD detector and using a 63x (1.4 NA) oil immersion objective, while cells were maintained in a live-cell chamber at 37°C and 5% CO2. High resolution (1024x1024) z-stacks were collected of cells of interest. To aid in the relocation of these cells for CLEM, tile scan ((14)) overviews were taken and the positions of cells relative to nearby grid co-ordinates were recorded. Following imaging by live-cell light microscopy (LM), cells were prepared for electron microscopy as described in (1). EM images were collected of cells previously identified by LM. To assess the correlation the EM and LM data for each cell were overlaid (Adobe Photoshop CS6) using the Mitotracker® Deep Red FM signal (LM images) and

corresponding mitochondria (EM images) as a guide for image transformation.

Metabolic labelling and autoradiography. Subconfluent layers of BGM cells were grown in 35 mm dishes (Corning) and infected with CVB3 3A-H57Y at MOI 5 for 1 hour, after which time the incubation medium was replaced with fresh culture medium. Cells were incubated with 10 µg/ml dactinomycin for 1 hour prior to a 45-minute labelling with tritiated uridine ([5-3H], 1 mCi/ml) (Perkin Elmer), after which cells were washed several times to remove unincorporated label and fixed for 1 hour in 1.5% glutaraldehyde in 0.1M cacodylate buffer.. Control samples consisting of uninfected BGM cells pre-treated with dactinomycin and incubated with tritiated uridine were also prepared. Cells were then post-fixed with 1% osmium tetroxide for 1 hour in 0.1M cacodylate buffer followed by a 30 minute incubation with 1% tannic acid in 0.1M cacodylate buffer, after which they were dehydrated in ethanol and infiltrated and embedded in LX 112 resin (Ladd Research Industries) before polymerisation at 60°C. Sections of 50 nm were collected on formvar-coated EM grids and post stained with lead citrate and uranyl acetate, then prepared for autoradiography. For the addition of the layer of photographic emulsion (ILFORD L4), grids were first attached to microscope slides by gently pressing the grid edge against a line of double sided sticky tape applied down the length of the slide, taking care to avoid contact between the tape and the formvar layer. A layer of carbon (~12 nm thick) was then evaporated onto the grids to prevent any direct interaction between the stained epon sections and photographic emulsion, which was subsequently placed on the grids with the help of a wire loop. Samples were developed for autoradiography as described in (15).

SUPPLEMENTAL REFERENCES

1. van der Schaar HM, Melia CE, van Bruggen JA, Strating JR, van Geenen ME, Koster AJ, Barcena M, van Kuppeveld FJ. 2016. Illuminating the Sites of Enterovirus Replication in Living Cells by Using a Split-GFP-Tagged Viral Protein. mSphere 1.
2. Backes P, Quinkert D, Reiss S, Binder M, Zayas M, Rescher U, Gerke V, Bartenschlager R, Lohmann V. 2010. Role of annexin A2 in the production of infectious hepatitis C virus particles. J Virol 84:5775-89.
3. Rabouw HH, Langereis MA, Knaap RC, Dalebout TJ, Canton J, Sola I, Enjuanes L, Bredenbeek PJ, Kikkert M, de Groot RJ, van Kuppeveld FJ. 2016. Middle East Respiratory Coronavirus Accessory Protein 4a Inhibits PKR-Mediated Antiviral Stress Responses. PLoS Pathog 12:e1005982.
4. Langereis MA, Feng Q, Nelissen FH, Virgen-Slane R, van der Heden van Noort GJ, Maciejewski S, Filippov DV, Semler BL, van Delft FL, van Kuppeveld FJ. 2014. Modification of picornavirus genomic RNA using 'click' chemistry shows that unlinking of the VPg peptide is dispensable for translation and replication of the incoming viral RNA. Nucleic Acids Res 42:2473-82.
5. van Eijl R, van den Brand T, Nguyen LN, Mulder KW. 2017. Reactivity of human AGO2 monoclonal antibody 11A9 with the SWI/SNF complex: A case study for rigorously defining

antibody selectivity. Sci Rep 7:7278.
6. Lanke KH, van der Schaar HM, Belov GA, Feng Q, Duijsings D, Jackson CL, Ehrenfeld E, van Kuppeveld FJ. 2009. GBF1, a guanine nucleotide exchange factor for Arf, is crucial for coxsackievirus B3 RNA replication. J Virol 83:11940-9.
7. Hato SV, Ricour C, Schulte BM, Lanke KH, de Bruijni M, Zoll J, Melchers WJ, Michiels T, van Kuppeveld FJ. 2007. The mengovirus leader protein blocks interferon-alpha/beta gene transcription and inhibits activation of interferon regulatory factor 3. Cell Microbiol 9:2921-30.
8. van der Schaar HM, Leyssen P, Thibaut HJ, de Palma A, van der Linden L, Lanke KH, Lacroix C, Verbeken E, Conrath K, Macleod AM, Mitchell DR, Palmer NJ, van de Poel H, Andrews M, Neyts J, van Kuppeveld FJ. 2013. A novel, broad-spectrum inhibitor of enterovirus replication that targets host cell factor phosphatidylinositol 4-kinase IIIbeta. Antimicrob Agents Chemother 57:4971-81.
9. MacLeod AM, Mitchell DR, Palmer NJ, Van de Poel H, Conrath K, Andrews M, Leyssen P, Neyts J. 2013. Identification of a series of compounds with potent antiviral activity for the treatment of enterovirus infections. ACS Med Chem Lett 4:585-9.
10. van der Schaar HM, van der Linden L, Lanke KH, Strating JR, Purstinger G, de Vries E, de Haan CA, Neyts J, van Kuppeveld FJ. 2012. Coxsackievirus mutants that can bypass host factor PI4KIIIbeta and the need for high levels of PI4P lipids for replication. Cell Res 22:1576-92.
11. Wessels E, Duijsings D, Niu TK, Neumann S, Oorschot VM, de Lange F, Lanke KHW, Klumperman J, Henke A, Jackson CL, Melchers WJG, van Kuppeveld FJM. 2006. A viral protein that blocks Arf1-mediated COP-I assembly by inhibiting the guanine nucleotide exchange factor GBF1. Developmental Cell 11:191-201.
12. Dorobantu CM, van der Schaar HM, Ford LA, Strating JRPM, Ulferts R, Fang Y, Belov G, van Kuppeveld FJM. 2014. Recruitment of PI4KIII beta to Coxsackievirus B3 Replication Organelles Is Independent of ACBD3, GBF1, and Arf1. Journal of Virology 88:2725-2736.
13. Limpens RWAL, van der Schaar HM, Kumar D, Koster AJ, Snijder EJ, van Kuppeveld FJM, Barcena M. 2011. The Transformation of Enterovirus Replication Structures: a Three-Dimensional Study of Single- and Double-Membrane Compartments. mBio 2.
14. Faas FG, Avramut MC, van den Berg BM, Mommaas AM, Koster AJ, Ravelli RB. 2012. Virtual nanoscopy: generation of ultra-large high resolution electron microscopy maps. J Cell Biol 198:457-69.
15. Ginsel LA, Onderwater JJ, Daems WT. 1979. Resolution of a gold latensification-elon ascorbic acid developer for Ilford L4 emulsion. Histochemistry 61:343-6.

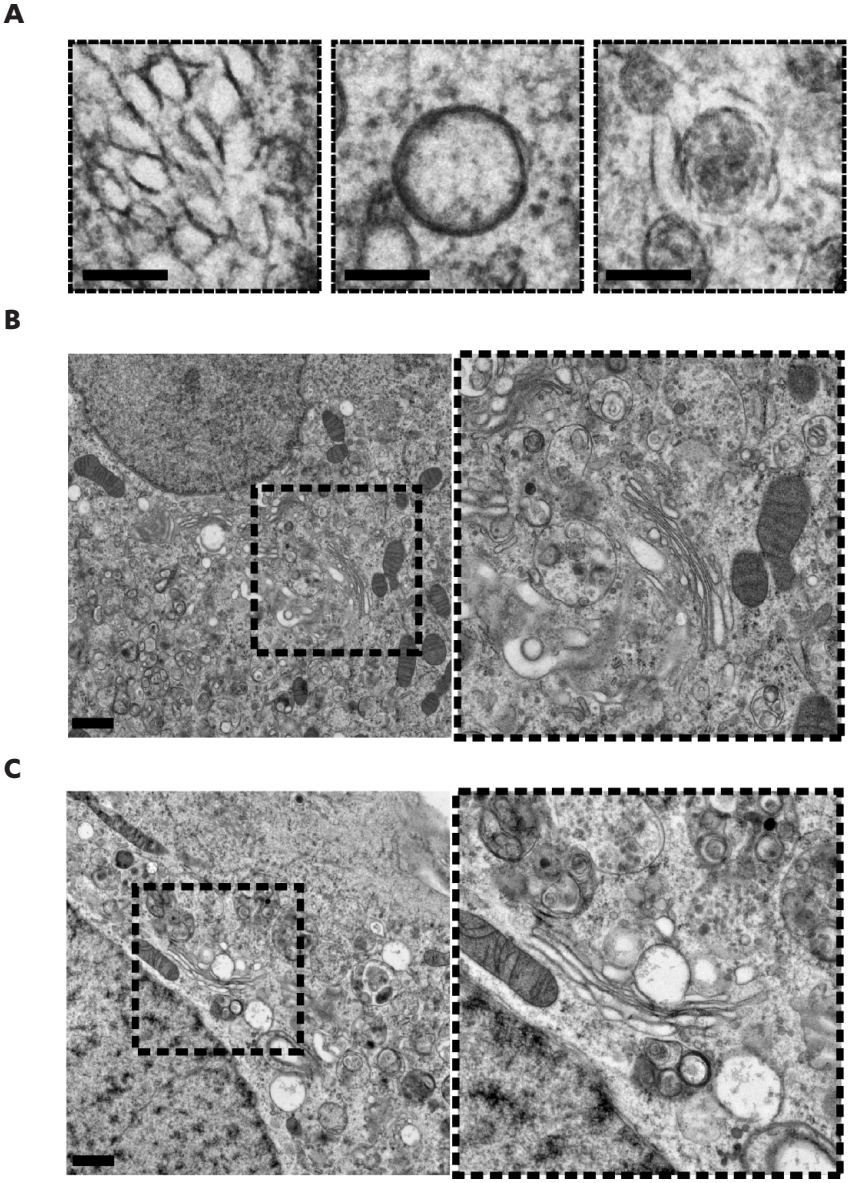


Figure S1. The morphologies of WT CVB3 and CVB3 3A-H57Y ROs in BGM cells are indistinguishable. BF738735 treatment does not affect Golgi apparatus architecture. A) BGM cells infected with WT CVB3 and prepared for EM by HPF-FS reveal typical enterovirus ROs, including single-membrane tubules, DMVs and multilamellar vesicles (left to right). B, C). BGM cells either untreated (B) or treated with BF738735 for 7 hours (C) were fixed for EM analysis. Representative images are shown illustrating that the morphology of the Golgi apparatus was unaffected by treatment. Scale bars, 200 nm (A) or 1 µm (B, C).

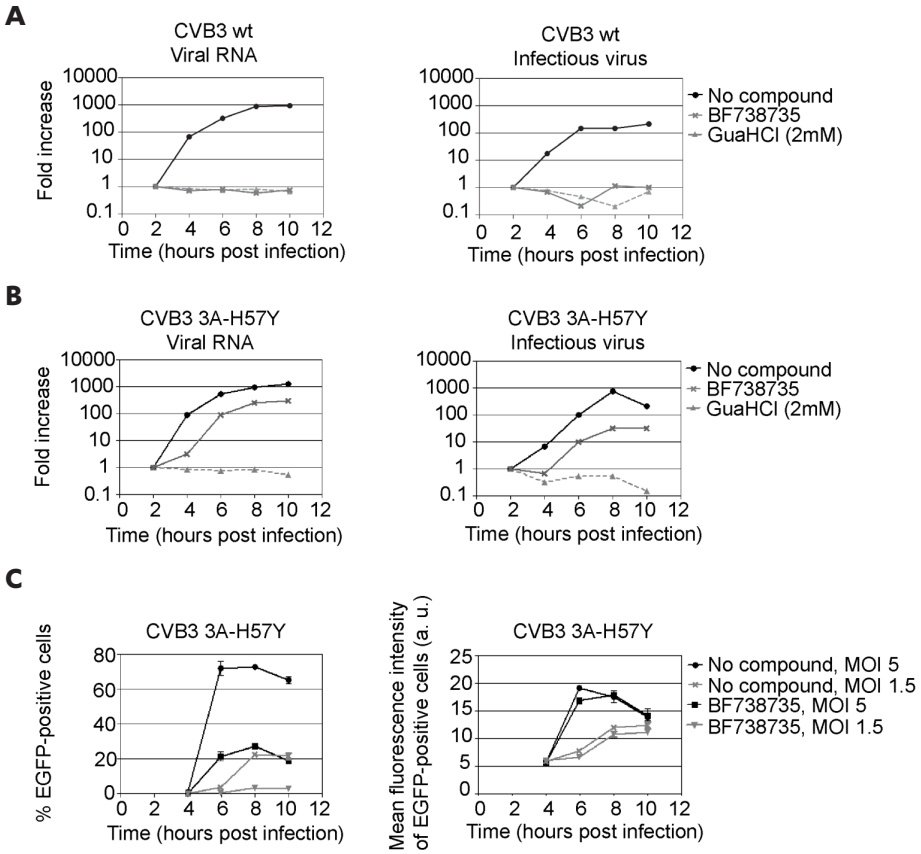


Figure S2. Replication kinetics of CVB3 3A-H57Y differ in the presence or absence of PI4KB inhibitor. A, B) Growth curve analysis. BGM cells were infected with CVB3 WT (A) or CVB3 3A-H57Y (B) and treated with compounds where specified. At the indicated time points, cells were either lysed to determine the intracellular level of viral RNA with quantitative RT-PCR (left graphs), or frozen to titrate the total amount of infectious virus produced (right graphs). Results are expressed as fold increase relative to the quantities at 2 hpi. C) Flow cytometry analysis. BGM cells were infected with EGFP-CVB3 3A-H57Y at different MOIs in the presence or absence of BF738735. At the indicated time points, cells were collected and fixed for flow cytometry analysis to determine the percentage of EGFP-positive cells (left graph) and the mean fluorescence intensity of the EGFP-positive cells (right graph) as an indicator of the level of viral proteins produced. Values represent mean values of triplicates ± standard error of the means.

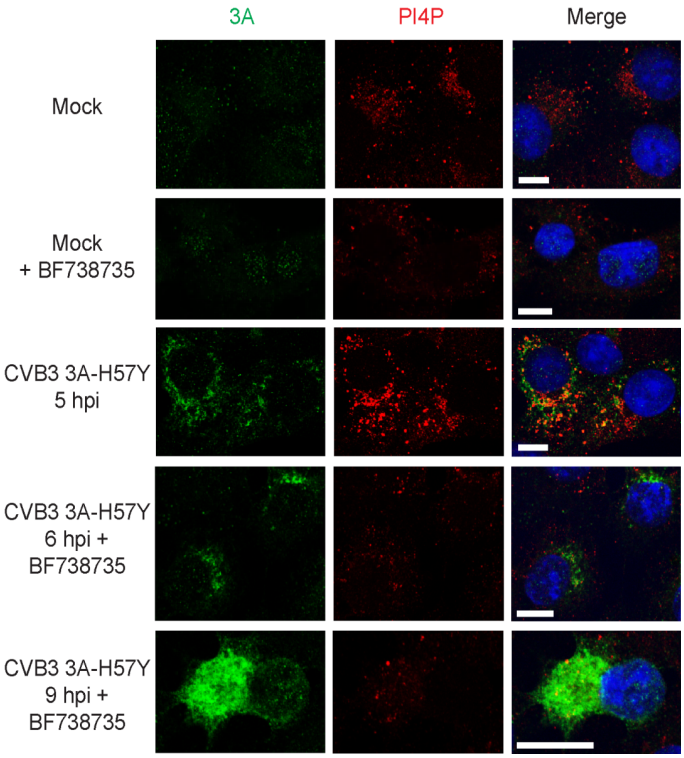


Figure S3. PI4P accumulation is not detected in cells infected with CVB3 3A-H57Y in the presence of PI4KB inhibitor. BGM cells were infected with CVB3 3A-H57Y at MOI 10 and treated with BF738735 where indicated. At the specified time points, cells were fixed and labelled with antibodies against 3A (green) or PI4P (red) alongside a nuclear stain (blue). Confocal images were acquired with a Leica SpeII confocal microscope. Without inhibitor, the level of PI4P signal was considerably elevated (saturated relative to background) in infected cells. In the presence of inhibitor no increase in PI4P was detected in infected cells, even at late time points (9 hpi). Scale bars, 10 µm

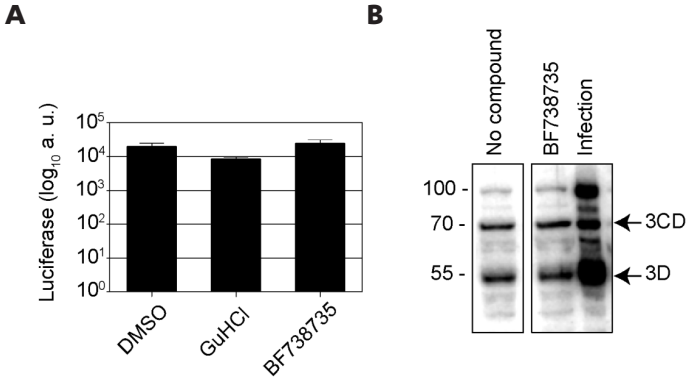


Figure S4. Viral protein production by the replication-independent expression system is not affected by PI4KB inhibition. HuH-7/T7 cells were mock-transfected or transfected with CVB3 3A-H57Y cDNA, which is under the control of a T7 promoter sequence and rendered replication-incompetent by altering the 5'UTR of the genome. cDNA used in (A) additionally encoded Renilla luciferase upstream of the P1 region as a sensitive measure for viral protein production. Cells were treated with BF738735 where indicated. A) At 6 h post transfection, cells were lysed to determine the intracellular luciferase amount. Guanidine Hydrochloride (GuHCl) (2 mM) was used as a positive control for protein production independent of viral RNA synthesis. Values represent mean values of triplicates ± standard error of the means. B) At 7 h post-transfection, cells were lysed and subjected to Western Blot analysis using an antibody against 3D. A lysate of CVB3-infected cells was used as a positive control. Marker bands of the indicated size (in kDa) are indicated.

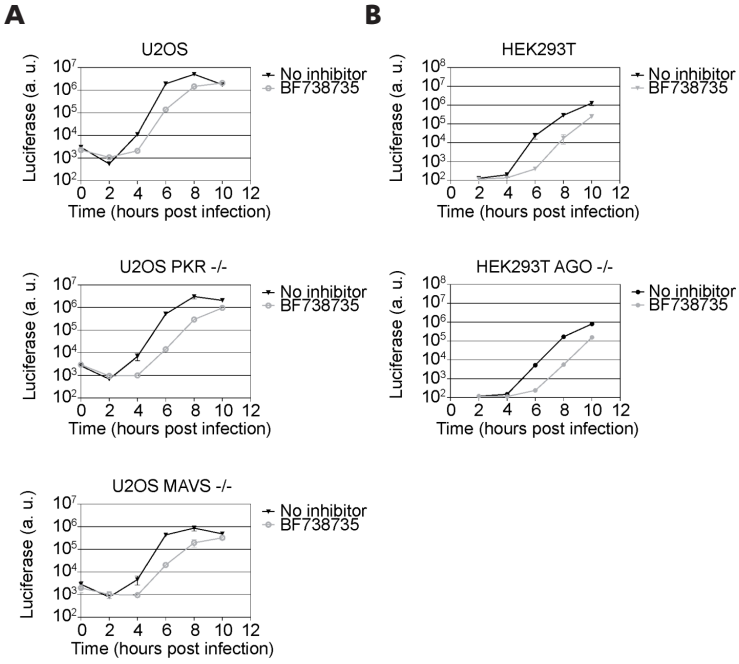


Figure S5. Innate antiviral responses during CVB3 3A-H57Y infection. U2OS or HEK293T cells (KO for PKR, MAVS and AGO where indicated) were infected with CVB3-Rluc 3A-H57Y at MOI 0.01. Following infection, the inoculum was removed and fresh medium with or without BF738735 inhibitor was added to the cells. Cells were lysed to determine the intracellular amounts of luciferase as a measure of genome replication. Values represent mean values of triplicates ± standard error of the means.

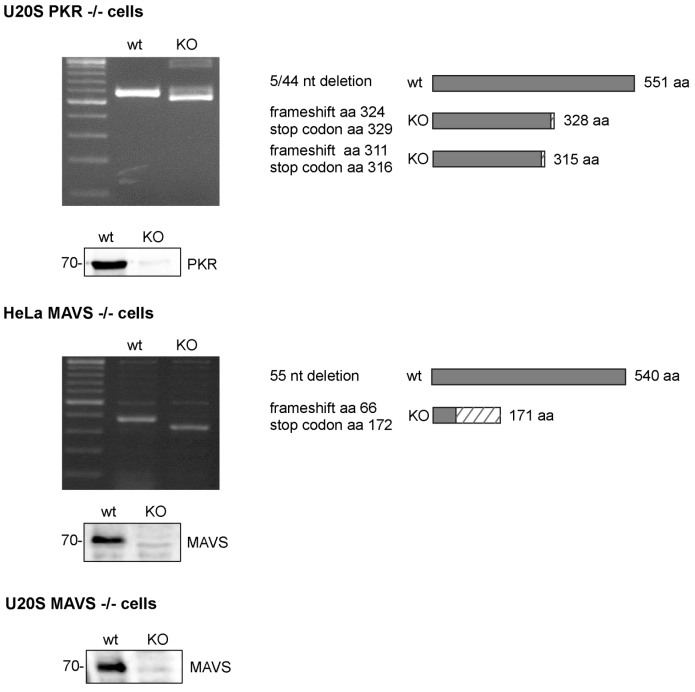


Figure S6. Generation of MAVS-/- and PKR-/- cells using the CRISPR-Cas9 system.
Single-cell clones of HeLa or U2OS cells were characterized by isolation of genomic DNA and PCR with gene-specific primers for PKR or MAVS, followed by sequence analysis (upper panels). All alleles contain a deletion resulting in a frame-shift event and a premature stop codon. The knock-out was confirmed by Western blot analysis of cell lysates (lower panels; marker bands of the indicated size in kDa are indicated on the left). U2OS MAVS-/- cells were only analysed by Western blot.

CHAPTER 4

THE EMERGENCE OF ENTEROVIRUS REPLICATION ORGANELLES CAPTURED BY WHOLE-CELL ELECTRON MICROSCOPY

C.E. Melia[1], C.J. Peddie[2], A.W.M. de Jong[1], E.J. Snijder[3], L.M. Collinson[2], A.J. Koster[1], H.M. van der Schaar[4,$], F.J.M. van Kuppeveld[4,$], M. Bárcena[1]

Submitted

[1] Section Electron Microscopy, Department of Cell and Chemical Biology, Leiden University Medical Center, Leiden, The Netherlands

[2] Electron Microscopy STP, The Francis Crick Institute, London, UK.

[3] Molecular Virology Laboratory, Department of Medical Microbiology, Center of Infectious Diseases, Leiden University Medical Center, Leiden, The Netherlands

[4] Virology Division, Faculty of Veterinary Medicine, Department of Infectious Diseases & Immunology, Utrecht University, Utrecht, The Netherlands

[$]These authors contributed equally

SUMMARY

Enterovirus genome replication occurs at virus-induced structures derived from cellular membranes and lipids. However, the origin of these replication organelles (ROs) remains shrouded in uncertainty. Direct ultrastructural evidence of the membrane donor is lacking, suggesting that the sites of its transition into ROs are rare or fleeting. To overcome this challenge, we combined live-cell imaging and serial block-face scanning electron microscopy of whole cells to capture emerging enterovirus ROs. The first foci of fluorescently-labelled viral protein correlated with ROs connected to the endoplasmic reticulum (ER) and preceded the appearance of ROs stemming from the trans-Golgi network. Whole-cell datasets further revealed striking contact regions between ROs and lipid droplets that may represent a route for lipid shuttling to facilitate RO proliferation and genome replication. Our data provide direct evidence that enteroviruses use ER then Golgi membranes to initiate RO formation, demonstrating the remarkable flexibility with which enteroviruses usurp cellular organelles.

INTRODUCTION

The production of novel membrane structures is an intriguing and highly conserved feature of positive-sense RNA (+RNA) virus infections. These modified host-cell membranes are increasingly referred to as viral replication organelles (ROs); distinct membrane structures that have been suggested to serve as platforms for viral RNA synthesis, by co-ordinating different stages of the viral replicative cycle and/or shielding viral products from innate immune sensors (1-3).

While the formation of ROs during infection is a hallmark of +RNA virus replication, the specific morphologies produced vary by virus. Some viruses (e.g. dengue virus (4) and Zika virus (5)) produce membrane invaginations, or 'spherules', in the membranes of cellular organelles. Other viruses (e.g. hepatitis C virus (6) and SARS coronavirus (7)) produce double-membrane vesicles (DMVs), which can be found in isolation or with outer-membrane connections to the endoplasmic reticulum (ER), from which they are derived. Identifying the cellular donor organelle for +RNA virus ROs provides important clues about the host factor requirements underlying viral replication. However, determining the donor is problematic when ultrastructural analyses fail to capture direct connections between cellular organelles and ROs. This is the case for the enteroviruses, a large genus of the Picornavirus family that includes important human pathogens like poliovirus, coxsackie-A and -B viruses, several numbered enteroviruses (e.g. EV-71 and EV-D68), and rhinoviruses.

Enterovirus ROs represent a compositionally and morphologically unique structure in the cells they infect. Their proliferation and utility as replication membranes are dependent on lipids like cholesterol and phosphatidylcholine, which are recruited to ROs via co-opted cellular lipid transport mechanisms, and whose levels are sustained by upregulated import, the lipolysis of lipid droplets (LDs) and lipid biosynthesis (8-11). During the earlier stages of infection, enteroviruses produce ROs with a single-membrane tubule (SMT) morphology, which transform into double-membrane vesicles (DMVs) and multi-lamellar vesicles as infection progresses (12, 13). These membrane morphologies parallel those found in cells infected with cardioviruses, another genus of Picornaviridae. Ultrastructural studies suggest that cardiovirus ROs are ER-derived, as connections between cardiovirus ROs and the ER have been found at early infection stages (14).

For enteroviruses, however, ROs have thus far been observed only as separate compartments that lack direct connections to any cellular organelle.

Establishing the cellular donor organelle for enterovirus RO formation by other means has proven challenging, as different studies and experimental approaches support different candidates (15). One of these candidates is the Golgi apparatus, which appears to be a suitable platform for early viral RNA (vRNA) synthesis. Under conditions where RO formation is arrested, sustained replication of a mutant enterovirus takes place at trans-Golgi membranes with a typical morphology (16). This aligns with fluorescence in-situ hybridisation studies of wt enterovirus infection, which have revealed colocalisation between a Golgi/trans-Golgi marker and early vRNA (17). In contrast, another study monitoring RNA incorporation found newly synthesised vRNA proximal to ER membranes early in infection (18), with no apparent involvement of the Golgi apparatus. Furthermore, co-localisation studies in cells, and biochemical analyses of isolated enterovirus-induced membrane structures, have revealed associations between putative ROs and numerous Golgi, ER and autophagy proteins (including PI4KB, GBF1, Arf1, Rab1, TGN46, GM130, PDI, P63, Sec31 and LC3 (17), (19), (20)). Rather than implicating the host membranes to which they localise in RO biosynthesis, host proteins may be recruited to ROs independently and differentially, according to infection stage, host cell or viral species studied.

While directly visualising membrane connections between donor organelle and nascent enterovirus ROs would help clarify whether the ER, Golgi apparatus or other membranes are utilised for RO formation, the lack of such connections in ultrastructural studies to date suggests that they are rare or transient and thus difficult to capture. We here utilise correlative light and electron microscopy (CLEM) and serial block-face scanning electron microscopy (SBF-SEM) to overcome this problem and explore the development of ROs at early and advanced stages of enterovirus infection. SBF-SEM is a recently developed technique that facilitates the reconstruction of large volumes (whole cells and tissues) but at the expense of resolution when compared to conventional TEM (21). First, we explored the resolving power of this technique on enterovirus-infected cells and extracted quantitative information about the abundance and volumes of RO clusters. We next set out to pinpoint the subcellular location of RO biogenesis. For this, we monitored infection until the emergence of the first ROs in live cells, exploiting a split-GFP-tagged coxsackievirus that illuminates the viral 3A protein (22). These emerging 3A foci correlated with nascent ROs in SBF-SEM reconstructions, which were further assessed for any association between cellular organelles and ROs. A close physical association was found between ROs and LDs, whose volumes decreased over the course of infection, suggesting that RO proliferation is supported by the formation of tight LD-RO contacts that facilitate lipid transfer. Importantly, we were able to locate and resolve membrane continuities between putative donor organelles and ROs. Our data provide a timeline that unites apparently disparate observations related to the origins of enterovirus ROs, revealing that RO formation starts at the ER, followed by biogenesis at the trans-Golgi network. These findings suggest a remarkable flexibility in virus membrane utilisation of different cellular organelles to form morphologically similar structures.

RESULTS

Cellular ultrastructure during enterovirus infection explored by large volume electron microscopy

To assess the resolving power of SBF-SEM on enterovirus-infected cell ultrastructure, Vero E6 cells were infected with CVB3 and fixed at 6 hours post infection (hpi). Our previous studies with electron tomography showed that enterovirus ROs with different morphologies (i.e. single-membrane tubules, double-membrane vesicles, and multi-lamellar vesicles) are present at this time point. After fixation, cells were prepared and imaged by SBF-SEM along with mock-infected cells for comparison. These data revealed expansive fields of ROs in infected cells, which dominated a large volume of the cell cytoplasm (Fig. 1 and Movie 1). Although the individual membranes of

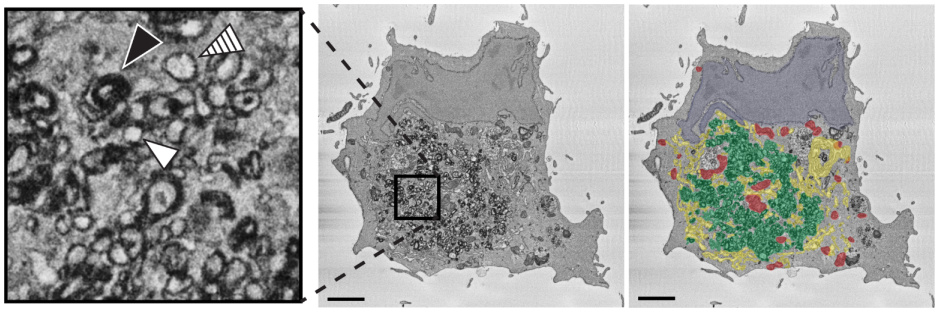


Figure 1. SBF-SEM imaging of CVB3-infected cells resolves ROs in their whole-cell context. Vero E6 cells were infected with CVB3 and fixed at 6 hours post-infection for SBF-SEM imaging. Left: a single slice from the SBF-SEM reconstruction of an infected cell. The cytosol is populated by clusters of ROs (example in boxed area) including single-membrane (white arrowhead), double-membrane (hatched arrowhead) and multi-lamellar ROs (black arrowhead). Right: cellular organelles, including mitochondria (red), the ER (yellow) and the nucleus (blue) can be resolved alongside ROs (green). Scale bar is 2 µm.

single- and double-membrane ROs were not resolvable by SBF-SEM under the imaging conditions used, single-membrane ROs (white arrowheads) were distinguishable from double-membrane (hatched arrowheads) or multi-lamellar (black arrowheads) ROs by their apparent thicknesses (Fig 1, left). To support this interpretation, SBF-SEM images were compared with higher resolution TEM images collected from the same type of samples (Fig. S1A), confirming that enterovirus ROs were discernible in the SBF-SEM data. Cellular organelles like the ER, lipid droplets, cis-Golgi cisternae and trans-Golgi network could be unambiguously identified in SBF-SEM reconstructions of mock-infected cells through comparisons with TEM images (Fig. S1B). In infected cells, prominent cellular organelles like the nucleus, ER and mitochondria were also identified (highlighted in Fig 1, right), while Golgi cisternae were absent throughout these cell volumes. This whole-cell visualisation confirms that Golgi apparatus cisternae disintegrate completely during enterovirus infection, as was previously inferred from live cell imaging studies monitoring Golgi markers, and 2D EM cell-sections (12, 16, 17, 23).

In order to obtain quantitative insights into the abundance and volumes of enterovirus ROs at this stage of infection, the 3D distribution of the viral ROs was highlighted by manual segmentation of the RO regions, nucleus and the cytoplasm in two reconstructed cells: Cell A (Figs. 1 and 2) and Cell B (Fig. 2). CVB3-induced RO clusters accounted for large parts of the cytoplasmic volume: 16% of in

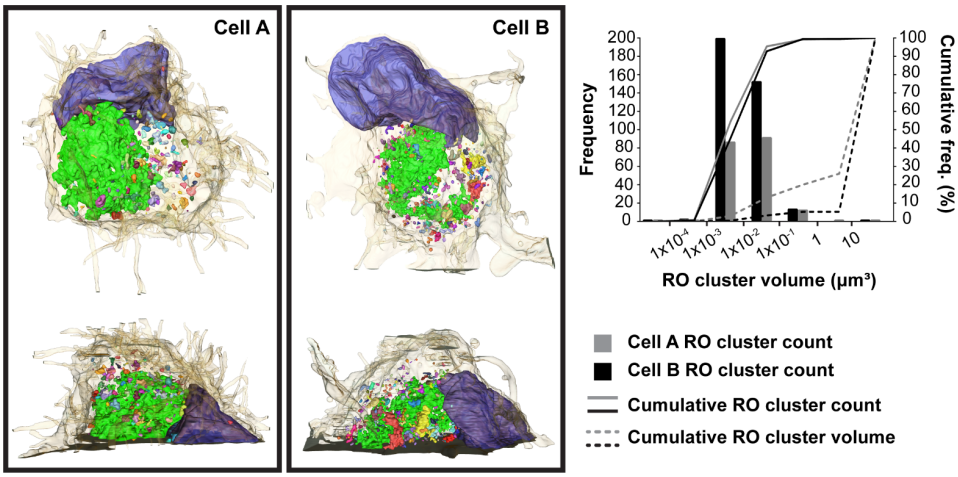


Figure 2. 3D analyses reveal the distribution of RO foci. Vero E6 cells were infected with CVB3 and fixed at 6 hours post-infection for SBF-SEM imaging. Segmentations of two infected cells (Cell A and Cell B) highlight the positions of individual ROs clusters (multi-coloured) and the nucleus (blue) within the cell volumes (beige, semi-transparent). The number of RO clusters and their respective volumes were quantified in these cells (graph), and the histogram of RO cluster sizes revealed a similar binary distribution in each cell, where the majority of RO volume in each cells falls within a single perinuclear cluster, while the majority of all other RO clusters are two orders of magnitude smaller. Cell A and Cell B were each collected over 163 sections (8.1 µm depth and total volume 3404 µm3 per cell).

cell A (104 µm3), and 6% in cell B (37 µm3). The difference likely reflects a more advanced infection stage in cell A, which is also supported by the large dilation of its ER (Fig. 1) that is associated with later stages of enterovirus infection (12, 24). The nanometer resolution achievable by SBF-SEM allowed RO clusters in close proximity to be segmented apart to analyse their size distribution (Fig. 2). For both cells, most of the ROs accumulated in a single large cluster (bright green segmented volumes, 98 µm3 in cell A, 27 µm3 in cell B), proximal to the nucleus. Most of the remaining RO clusters (coloured) were comparatively small, with more than 90% of the RO clusters smaller than 0.1 µm3 in both cells (Fig. 2, graph). The presence of numerous smaller RO foci at this late stage of infection could suggest that novel RO clusters emerge continuously throughout infection, which may eventually fuse with and contribute to the large perinuclear cluster. Alternatively, these small clusters may represent sites of early RO formation that fail to expand or fuse with the larger perinuclear cluster.

Enterovirus RO biogenesis occurs at distinct ER- or trans-Golgi network-derived foci

Our previous live-cell imaging data demonstrated that the onset of Golgi apparatus disintegration in CVB3 infection is concomitant with the accumulation of viral protein (e.g. 3A) in the Golgi region (16, 22). Intriguingly, the first foci of 3A protein arise in the cell periphery, often ahead of the dramatic 3A accumulation in the Golgi region that expands to dominate the cell cytoplasm as infection progresses (Movie 2, white and black arrowheads respectively). It is unknown whether both the peripheral and Golgi-proximal 3A foci that emerge during this phase represent developing ROs. One intriguing possibility is that the small peripheral 3A foci that form early in infection are replication-independent, and that these 3A accumulations are merely the result of translation of the incoming vRNA delivered by uncoating of virus particles. To test this, we inhibited vRNA synthesis

by treating infected cells with guanidine hydrochloride (GuHCl) and monitored these cells by live-cell imaging. The CVB3 3A was visualized by utilizing a split-GFP system (22). Neither peripheral nor any other 3A-GFP signal emerged under GuHCl inhibition, demonstrating that their formation is not a product of translation of only incoming vRNA, but depends upon vRNA replication (Fig S2). Next, we investigated whether virus-induced membrane structures could be detected at both peripheral and Golgi-associated 3A foci. To do so, we imaged living cells expressing mCherry-

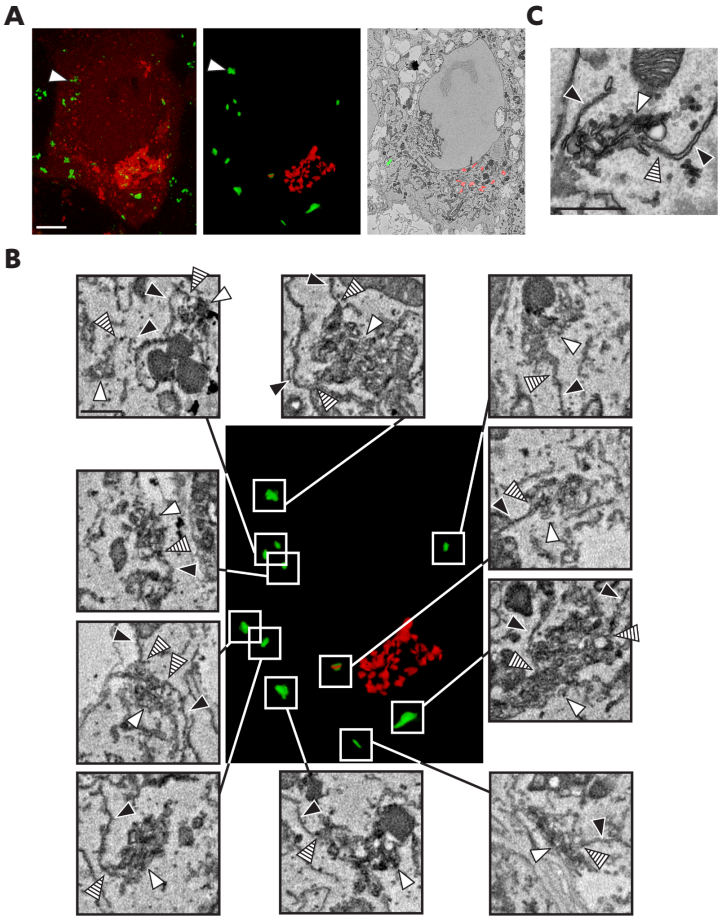


Figure 3. Correlative SBF-SEM and LM highlights the appearance of ROs connected to the ER early in infection. BGM(S1-10) cell transduced with mCherry-GM130 and infected with CVB3 3A(S11) and monitored by live-cell imaging until the first 3A-GFP puncta emerged. A final confocal z-stack of mCherry-G130 (red) and 3A-GFP (green) signals was taken prior to chemical fixation for SBF-SEM A) (Left) Volume rendering of the final confocal z-stacks prior to fixation and processing for SBF-SEM, (middle) 3D rendering of the ROs (green) and Golgi cisternae (red) segmented from the corresponding SBF-SEM volume, and (right) a representative SBF-SEM slice. The intense GM130 signal in confocal data corresponds to recognisable Golgi apparatus cisternae in SBF-SEM data. A good overall correspondence can also be established between 3A-GFP puncta and RO foci (e.g. white arrowheads), despite small discrepancies in their relative position that suggest limited migration of ROs in the delay between LM imaging and fixation. B) Membrane continuities (hatched arrowheads) between all the RO clusters in the cell (white arrowheads) and ER membranes (black arrowheads) could be observed. C) Continuities between the ER and ROs could also be found in high resolution 2D TEM data. Scale bars are 5 µm (A) and 500 nm (B and C).

GM130, a cis-Golgi marker, and infected them with CVB3 encoding split-GFP-tagged 3A (22). Confocal z-stacks were collected of cells with emerging 3A-GFP signal but at different stages of Golgi disassembly (~ 4.5 hpi), which were then fixed and prepared for SBF-SEM. Acquired SBF-SEM volumes were manually segmented to highlight Golgi cisternae and RO clusters based solely on morphological features, which could then be compared with 3D reconstructions of corresponding confocal data (Fig. 3A, workflow illustrated in Movie 3). A striking correspondence was found between 3A-GFP foci in the confocal data and the location of ROs highlighted by the SBF-SEM segmentation, although in some cases a shift in the relative positions of 3A-GFP foci and RO clusters was apparent (e.g. hatched arrowheads, Fig. 3A). This may be explained by migration of RO clusters in the delay between confocal z-stack acquisition and fixation (ca. 10 min for CLEM datasets), as peripheral 3A-GFP foci are often dynamic (Movie 2, hatched arrowheads).

The cell presented in Fig. 3 represents an early stage of infection encompassing the emergence of the first peripheral 3A-GFP foci. These foci are largely distal to the Golgi region, where minimal 3A-GFP signal is apparent. The Golgi apparatus appears relatively intact at this stage of infection, as recognisable Golgi cisternae could be detected. All RO clusters at this stage (Fig. 3B, white arrowheads) were observed in close contact with the ER (Fig. 3B, black arrowheads), with

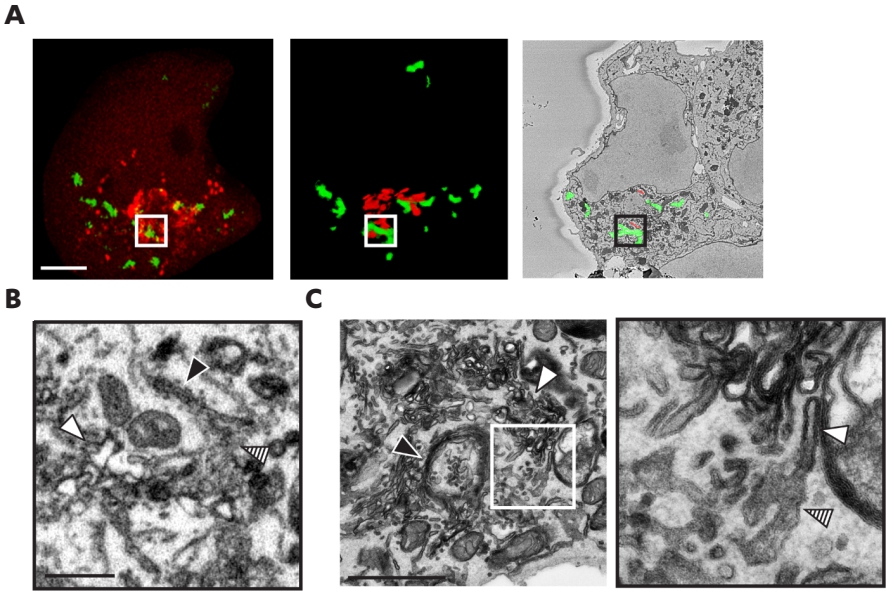


Figure 4. Correlative SBF-SEM and LM exposes RO clusters connected to the Golgi apparatus. BGM(S1-10) cell transduced with mCherry-GM130 and infected with CVB3 3A(S11) and monitored by live-cell imaging until 3A-GFP signal emerged in the Golgi region. A) (Left) Volume rendering of the confocal z-stacks (left) acquired prior to fixation and processing for SBF-SEM, (middle) 3D rendering of the ROs (green) and Golgi cisternae (red) segmented from the corresponding SBF-SEM volume, and (right) a representative SBF-SEM slice. The mCherry-GM130 and 3A-GFP signals correlated well with recognizable Golgi apparatus cisternae and RO clusters, respectively. B) Assessment of a region (boxed area in A) containing Golgi-proximal RO foci reveals a membranous region (hatched arrowhead) bridging ROs (white arrowhead) and the Golgi apparatus (black arrowhead). C) A similar region imaged using TEM reveals membrane continuities between RO clusters (white arrowhead) and the Golgi apparatus (black arrowhead). These continuities comprise tubules of the trans-Golgi network (hatched arrowhead) and single-membrane RO tubules (black arrowhead). Scale bars are 5 µm (A) and 1 µm (B and C).

apparent membrane continuities between them (Fig. 3B, hatched arrowheads). The existence of membrane connections between peripheral RO clusters and ER was confirmed in higher resolution TEM images of parallel samples (Fig. 3C). These data suggest that 3A foci that emerge in the cell periphery correspond with ROs that are derived from ER membranes.

Following the emergence of peripheral 3A signal, 3A-GFP accumulates in the Golgi region (Movie 2, white and black arrowheads respectively). An example of a cell fixed at this stage of infection is shown in Fig. 4A. The 3D confocal model reveals 3A-GFP signal in close proximity to mCherry-GM130 signal, which corresponded to ROs and Golgi cisternae respectively in SBF-SEM data (Fig. 4A). ROs in the Golgi region (e.g. Fig 4B, boxed region in 4A) were connected to membranous regions that bridged the trans-Golgi network (Fig. 4B, hatched arrowheads) and RO clusters (Fig. 4B, black arrowhead). ER-associated RO clusters were also found in the cell periphery (Fig. S3), demonstrating that both ER- and Golgi-associated ROs can coexist in infected cells and suggesting that ER-RO interactions persist at later stages of infection. To examine Golgi-associated ROs at

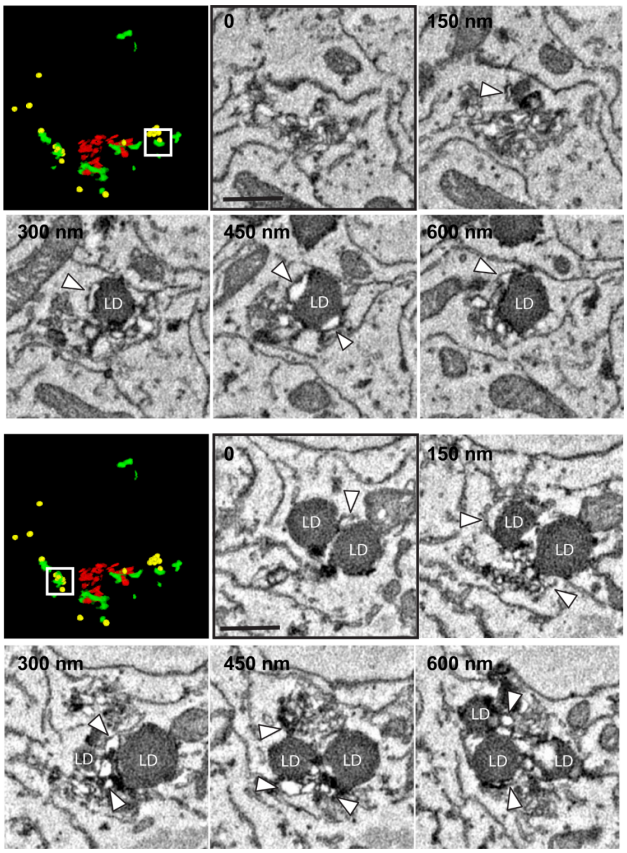


Figure 5. SBF-SEM and TEM data reveal extensive contact between ROs and LDs. Serial SBF-SEM sections from two regions of interest in the cell shown in Fig. 4 (boxed areas in the segmentation models; red, Golgi cisternae, green, ROs, yellow, lipid droplets) are presented, highlighting the association between RO tubules (white arrowheads) and lipid droplets (LD). Frame numbers (top left) indicate the relative depth from frame 0 through the SBF-SEM volume. Scale bars are 500 nm.

higher resolution, samples prepared for SBF-SEM were imaged in parallel by TEM (Fig 4C). In addition to Golgi cisternae (Fig. 4C, white arrowhead) and ROs (Fig. 4C, black arrowhead), TEM images revealed continuities between trans-Golgi network tubules and single-membrane ROs (Fig. 4C, hatched arrowhead). Altogether, these data suggest that early RO biogenesis occurs at seed points distributed across the ER, followed by RO formation at trans-Golgi membranes.

Beyond the ER- and Golgi-associated RO foci highlighted by the 3A-GFP signal, significant spatial relationships between ROs and other cellular organelles, including endosomes, lysosomes, autophagosomes and mitochondria, were not clearly apparent in any cells analysed. However, extensive contact regions could be found between RO clusters and lipid droplets (LDs), which in some cases appeared to be surrounded by ROs (Fig. 5, arrowheads). Interestingly, a qualitative analysis of the number of LDs in SBF-SEM cell reconstructions of cells fixed at late infection stages (n=6) hinted at a possible inverse correlation between the infection stage (assessed by RO abundance) and the LD content. A quantitative analysis of LDs, visualized with Oil Red O stain by light microscopy, confirmed that LDs were depleted across CVB3 infection in our experimental setup, and showed a particularly rapid drop early in infection (between 0 and 4 hpi) both in LD counts and total LD area per cell (Fig. S4). This result is in line with previous immunofluorescence data obtained during enterovirus infection (9, 25) Together, our results suggest that the extensive contact regions between ROs and LDs could be utilised for the transfer of critical lipids to ROs, supporting their formation and proliferation.

DISCUSSION

Establishing the origin of viral ROs reveals important clues about the host cell requirements for their formation. For enteroviruses, existing data suggest that components of the Golgi apparatus, ER, ER exit sites (ERES), autophagy pathway, endolysosomal compartments or any combination thereof may contribute to the development of ROs (17-19). Ultrastructural evidence of continuities between cellular organelles and ROs that would shed light on the membrane donor organelle has been lacking, however, suggesting that connections between enterovirus ROs and cellular organelles are rare, or that the association of ROs with their donor organelle is short-lived. To capture these events, we employed live-cell imaging to monitor the emergence of viral 3A protein using a split-GFP system. The resulting 3A-GFP signal was utilised as a correlative marker to highlight potential sites of interest in SBF-SEM cell volumes, which were further assessed for any association between cellular membranes and ROs.

Intriguingly, RO clusters were found both in the cell periphery and in the perinuclear region at early infection time-points. Close examination of SEM volumes revealed connections between peripheral RO clusters and ER membranes, and membranous regions that bridged perinuclear RO clusters and the trans-Golgi network. Higher resolution TEM images of similar regions confirmed the existence of membrane continuities between trans-Golgi tubules and ROs. Peripheral 3A-GFP foci, which were found to correspond to ER-derived ROs, largely emerge prior to those found in the Golgi region (22) (Movie 2). Thus, the ER in most cells is the initial site of enterovirus RO formation, followed by the appearance of Golgi-derived ROs. This chronological separation between ER and Golgi-associated ROs could account to some extent for disparate observations of Golgi- or ER-RO associations found in previous studies (13, 17, 19) and has intriguing implications for the

spatiotemporal organisation of enterovirus infection. Our data demonstrate that ER- and Golgi-associated enterovirus ROs are morphologically similar, require vRNA synthesis for their formation, and accumulate viral protein. While these sites may be utilised at different infection stages, this could suggest that both are suitable for viral replication, which aligns with existing data suggesting that enterovirus replication can occur at the Golgi or ER (17, 18).

Further analyses of SEM volumes did not highlight membrane connections between other cellular structures and ROs, but revealed a striking physical association between RO clusters and lipid droplets (LDs) (Fig. 5). While previous LM data showed that LDs are located in the vicinity of rhinovirus ROs (25), our high-resolution data revealed that ROs are not only often close to enterovirus LDs, but they also establish extensive contacts with them. In light of a recent study demonstrating the importance of LD-derived lipids for enterovirus replication and RO formation (11), it is tempting to speculate that ROs and LDs can form bona fide membrane contact sites (MCS) containing tethers and lipid transfer machinery. These MCSs could underlie an important route for the recruitment of critical lipids for enterovirus RO formation, like fatty acids and cholesterol (8, 26), which may contribute to LD depletion as ROs proliferate over the course of infection (Fig S4).

Despite differences in the lipid and protein composition of the ER and trans-Golgi network (27), these data demonstrate that apparently morphologically identical enterovirus ROs can be derived from both sites. This indicates that any core cellular components required for enterovirus RO formation are common to both the ER and Golgi apparatus or readily recruited by viral proteins. The enterovirus host factor phosphatidylinositol 4-phosphate (PI4P), which was recently shown to expedite the formation of ROs (16), may represent one example of this. While the beta isoform of phosphatidylinositol 4-kinase, PI4KB, is primarily responsible for PI4P production at the Golgi apparatus, the alpha isoform PI4KA produces PI4P at the ER, with particularly high levels of PI4P present at ERES (28). Together with the observed associations between viral proteins and ERES markers (17, 19), this could nominate PI4P-rich ERES as candidate nucleation points for developing ER-RO foci. However, PI4KA inhibition does not affect the final replication yield during enterovirus infection (29, 30) (31), suggesting that ER-derived ROs may confer a small benefit early in infection, but are ultimately expendable for replication. Another possibility is that the PI4P utilised for ER-derived RO formation is supplied by PI4KB, recruited by the enterovirus 3A protein (17). While peripheral 3A protein also accumulated early in the replication of a mutant enterovirus, this accumulation was abolished under PI4KB inhibition (16), which could support the notion that ER-derived ROs require PI4KB. In this way, the compositional requirements for RO formation and viral replication would be met by supplementing suitable but diverse donor membranes with recruited host factors. Altogether, these data extend the growing body of evidence suggesting that +RNA viruses are not constrained to utilising membranes from a single cellular source for their replication, which, in some cases, can even be redirected to membranes of a different cellular organelle (32). Flexible recruitment of membranes for replication would confer a remarkable level of adaptability to different conditions, providing +RNA viruses with an important evolutionary advantage.

ACKNOWLEDGEMENTS

The authors would like to thank Ronald W. A. L. Limpens (EM section, LUMC) for his help with the preparation of the figures and movies. This work was supported by research grants from the

Netherlands Organization for Scientific Research (NWO-VENI-863.12.005 to H.M.V.D.S., NWO-VICI-91812628 to F.J.M.V.K., and ERASysApp project "SysVirDrug" ALW project number 832.14.003 to F.J.M.V.K. and E.J.S.) and from the European Union (7th Framework, EUVIRNA Marie Curie Initial Training Network, grant agreement number 264286 to F.J.M.V.K. and E.J.S.). The Francis Crick Institute receives its core funding from Cancer Research UK (FC001999), the UK Medical Research Council (FC001999), and the Wellcome Trust (FC001999), and from the UK Medical Research Council, the Biotechnology and Biological Sciences Research Council (BBSRC) and the Engineering and Physical Sciences Research Council (EPSRC) under grant [MR/K01580X/1]. The study design, data collection and interpretation, and the decision to submit the work for publication were carried out without input from the above funding bodies.

EXPERIMENTAL PROCEDURES

Cell lines and reagents. Vero E6 or BGM cells were cultured using Dulbecco's modified Eagle's medium (Gibco) supplemented with 10% fetal calf serum, penicillin, and streptomycin, and maintained at 37°C in 5% CO2. BGM(S1-10) cells, which express GFP(S1-10) and the puromycin resistance gene (Pac), have been described in (22). BGM(S1-10) cell culture medium was supplemented with an additional 30 µg/ml puromycin as a selection agent.

Viruses and infection. CVB3 3A(S11aa2), which encodes a 3A with the S11 region of GFP inserted after amino acid position 2, has been described in (22). CVB3 wt (strain Nancy) was generated as described in (16). For infection, cells were inoculated for 1 hour with CVB3 wt or CVB3 3A(S11) at MOI 50 and 5 respectively, after which the inoculum was removed and fresh medium was added. At specified time-points after infection cells were imaged by light microscopy and/or prepared for electron microscopy by chemical fixation or high-pressure freezing and freeze substitution.

Live cell imaging. BGM(S1-10) cells were grown to ~35% confluency in glass-bottom 4-chamber 35-mm dishes (CELLviewTM) and transduced with MLV mCherry-GM130 particles (described in (22)). Transduced cells were infected with CVB3 3A(S11) 18-24 hours later. Cells were washed with Fluorobrite medium (Thermo Fisher Scientific) supplemented with 8% fetal calf serum (FCS) and 25 mM HEPES just prior to imaging. LM data were collected using a Leica SP5 confocal microscope equipped with a HyD detector and a 63x (1.4 NA) oil immersion objective, with the confocal pinhole adjusted to 1 airy unit for GFP emission (95.56 µm pinhole). For time-series imaging, positions of interest (xyz) were marked and imaged sequentially at 5 minute intervals. For the duration of all imaging, cells were maintained at 37°C and 5% CO2 in a live-cell chamber. For correlative light and electron microscopy, cells were grown in glass-bottom MatTek dishes with an etched alphanumeric co-ordinate system (MatTek Corporation) to facilitate the relocation of the regions identified during light microscopy. Cells were monitored until the point of interest, at which time a confocal z-stack was acquired, after which samples were immediately fixed for electron microscopy. To minimise the time between the first image acquisition of each z-stack and fixation (ca. 10 minutes total), one field of view was imaged per sample.

Lipid droplet visualization and quantification. Vero E6 cells grown on coverslips were infected with CVB3 wt (MOI 100) and fixed with 3% paraformaldehyde for 1 hour at different infection times. Mock-infected cells were also fixed as a control. After washing with PBS, the coverslips were incubated for 1 h at room temperature with a freshly prepared mixture of Oil Red O (Sigma)

(0.5 % w/v in isopropanol) and double-distilled water (6:10) to stain LDs, washed with PBS and incubated with the nuclear stain Hoechst. The samples were then imaged in a Leica DM6 wide-field microscope with a 40x oil immersion objective using both differential interference contrast (DIC) and fluorescence imaging modes. LDs appeared as darkly stained circular profiles in the DIC images that were absent in unstained samples and could be also detected in fluorescent images using a Texas red excitation filter (540-580 nm) (33). A total of 25 cells per condition were randomly selected from the DIC images, and the LDs contained in those cells were counted and manually segmented from the fluorescent images using Amira 6.0.1 (Thermo Fisher), which was further used to compute the LD area per cell.

Electron microscopy

Preparation of chemically-fixed samples. Sample fixation, staining and embedding procedures were adapted from (34). Cells were fixed with 2.5% gluteraldehyde and 4% formaldehyde in 0.15 M cacodylate buffer for 60 minutes at room temperature. Initial post-fixation was carried out using a solution of 2% osmium tetroxide and 1.5% potassium ferricyanide in 0.15 M cacodylate for 60 minutes on ice. Samples were then treated with 1% aqueous thiocarbohydrazide for 20 minutes, followed by 2% aqueous osmium tetroxide for 30 minutes, and were finally incubated overnight at 4°C in 1% aqueous uranyl acetate. Samples were then stained using Walton's lead aspartate at 60°C for 30 minutes ahead of stepwise dehydration in ethanol. Samples were infiltrated with resin initially using a 50:50 mixture of propylene oxide and Durcupan ACM resin (Ladd research) for 60 minutes. Where MatTek dishes were used, coverslips were excised from the surrounding culture dish using a razor blade and removed to a container resistant to propylene oxide ahead of this step. Samples were then infiltrated with fresh undiluted Durcupan for 90 minutes, before covering regions of interest with inverted resin-filled BEEM capsules (Ted Pella) and polymerisation for 48 hours at 60°C. For TEM, sections of 70 nm were cut from the sample block for imaging and post-stained with uranyl acetate and lead citrate. For SEM, sample blocks were prepared as described in (35). Briefly, small portions of the cell monolayers were mounted on pins using conductive epoxy resin (Circuitworks CW2400), trimmed to form an approximately 400 x 400 x 150 µm pillar, ensuring that regions of interest were retained in the block-face for correlative samples, and coated with a 2 nm layer of platinum ahead of imaging.

Electron microscopy imaging. TEM images were collected in an FEI Tecnai12 BioTWIN using an Eagle 4k slow-scan CCD camera (FEI) or an FEI TWIN at 120 kV with OneView 4k high frame-rate camera (Gatan), both in binning mode 2. Serial block-face scanning electron microscopy (SBF SEM) data was collected using a 3View2XP (Gatan, Pleasanton, CA) attached to a Sigma VP SEM (Zeiss, Cambridge). Backscattered electron images were acquired using the 3VBSED detector. The SEM was operated at a chamber pressure of 5 pascals, with high current mode inactive. Variable pressure imaging conditions, which reduce the final resolution, aided in the suppression of charging resulting from the large regions of bare resin surrounding single cells. For CLEM data the 30 µm aperture was used with an accelerating voltage of 2 kV, a dwell time of 3 µs (10 nm reported pixel size, horizontal frame width of 81.9 µm) and 40 nm slice thickness. Two collection setups were used for samples fixed at 6 hpi infection, using either the 30 or 20 µm aperture and an accelerating voltage of 2 or 3 kV respectively. The imaging dwell time was 3 µs (5 nm reported pixel size; horizontal frame width of

20.5 µm) or 10 µs (6 nm reported pixel size; horizontal frame width of 24.6 µm), with a slice thickness of 50 or 30 nm.

SBF-SEM image processing and segmentation. SBF-SEM image stacks were acquired as dm3 files and converted to 32 bit TIFs for initial batch processing. Images were Gaussian filtered (1 pixel), followed by two rounds of unsharp mask and grey level normalisation (Adobe Photoshop). Image stacks were then converted to 8 bit TIFs and aligned using the virtual align slices plugin (Fiji). Segmentation of features within SBF-SEM data was carried out in a semi-automatic threshold-based way for the cell cytoplasm and manually for the viral ROs, nuclei and LDs using or Segmentation Editor (Fiji) or Amira 6.0.1 (Thermo-Fisher), which was then also employed to extract volume information on the different RO clusters.

REFERENCES

1. Paul D, Bartenschlager R. 2013. Architecture and biogenesis of plus-strand RNA virus replication factories. World J Virol 2:32-48.
2. Harak C, Lohmann V. 2015. Ultrastructure of the replication sites of positive-strand RNA viruses. Virology 479-480:418-33.
3. Egger D, Teterina N, Ehrenfeld E, Bienz K. 2000. Formation of the poliovirus replication complex requires coupled viral translation, vesicle production, and viral RNA synthesis. J Virol 74:6570-80.
4. Welsch S, Miller S, Romero-Brey I, Merz A, Bleck CKE, Walther P, Fuller SD, Antony C, Krijnse-Locker J, Bartenschlager R. 2009. Composition and Three-Dimensional Architecture of the Dengue Virus Replication and Assembly Sites. Cell Host & Microbe 5:365-375.
5. Cortese M, Goellner S, Acosta EG, Neufeldt CJ, Oleksiuk O, Lampe M, Haselmann U, Funaya C, Schieber N, Ronchi P, Schorb M, Pruunsild P, Schwab Y, Chatel-Chaix L, Ruggieri A, Bartenschlager R. 2017. Ultrastructural Characterization of Zika Virus Replication Factories. Cell Reports 18:2113-2123.
6. Romero-Brey I, Merz A, Chiramel A, Lee JY, Chlanda P, Haselman U, Santarella-Mellwig R, Habermann A, Hoppe S, Kallis S, Walther P, Antony C, Krijnse-Locker J, Bartenschlager R. 2012. Three-Dimensional Architecture and Biogenesis of Membrane Structures Associated with Hepatitis C Virus Replication. Plos Pathogens 8.
7. Knoops K, Kikkert M, van den Worm SHE, Zevenhoven-Dobbe JC, van der Meer Y, Koster AJ, Mommaas AM, Snijder EJ. 2008. SARS-coronavirus replication is supported by a reticulovesicular network of modified endoplasmic reticulum. Plos Biology 6:1957-1974.
8. Nchoutmboube JA, Viktorova EG, Scott AJ, Ford LA, Pei Z, Watkins PA, Ernst RK, Belov GA. 2013. Increased long chain acyl-Coa synthetase activity and fatty acid import is linked to membrane synthesis for development of picornavirus replication organelles. PLoS Pathog 9:e1003401.
9.. Ilnytska O, Santiana M, Hsu NY, Du WL, Chen YH, Viktorova EG, Belov G, Brinker A, Storch J, Moore C, Dixon JL, Altan-Bonnet N. 2013. Enteroviruses harness the cellular endocytic

machinery to remodel the host cell cholesterol landscape for effective viral replication. Cell Host Microbe 14:281-93.

10. van der Schaar HM, Dorobantu CM, Albulescu L, Strating J, van Kuppeveld FJM. 2016. Fat(al) attraction: Picornaviruses Usurp Lipid Transfer at Membrane Contact Sites to Create Replication Organelles. Trends Microbiol 24:535-546.
11. Viktorova EG, Nchoutmboube JA, Ford-Siltz LA, Iverson E, Belov GA. 2018. Phospholipid synthesis fueled by lipid droplets drives the structural development of poliovirus replication organelles. PLoS Pathog 14:e1007280.
12. Limpens RWAL, van der Schaar HM, Kumar D, Koster AJ, Snijder EJ, van Kuppeveld FJM, Barcena M. 2011. The Transformation of Enterovirus Replication Structures: a Three-Dimensional Study of Single- and Double-Membrane Compartments. mBio 2.
13. Belov GA, Nair V, Hansen BT, Hoyt FH, Fischer ER, Ehrenfeld E. 2012. Complex Dynamic Development of Poliovirus Membranous Replication Complexes. Journal of Virology 86:302-312.
14. Melia CE, van der Schaar HM, de Jong AWM, Lyoo HR, Snijder EJ, Koster AJ, van Kuppeveld FJM, Barcena M. 2018. The Origin, Dynamic Morphology, and PI4P-Independent Formation of Encephalomyocarditis Virus Replication Organelles. MBio 9.
15. Richards AL, Soares-Martins JAP, Riddell GT, Jackson WT. 2014. Generation of Unique Poliovirus RNA Replication Organelles. mBio 5.
16. Melia CE, van der Schaar HM, Lyoo H, Limpens R, Feng Q, Wahedi M, Overheul GJ, van Rij RP, Snijder EJ, Koster AJ, Barcena M, van Kuppeveld FJM. 2017. Escaping Host Factor PI4KB Inhibition: Enterovirus Genomic RNA Replication in the Absence of Replication Organelles. Cell Rep 21:587-599.
17. Hsu NY, Ilnytska O, Belov G, Santiana M, Chen YH, Takvorian PM, Pau C, van der Schaar H, Kaushik-Basu N, Balla T, Cameron CE, Ehrenfeld E, van Kuppeveld FJ, Altan-Bonnet N. 2010. Viral reorganization of the secretory pathway generates distinct organelles for RNA replication. Cell 141:799-811.
18. Bienz K, Egger D, Pasamontes L. 1987. Association of Polioviral Proteins of the P2-Genomic Region with the Viral Replication Complex and Virus-Induced Membrane Synthesis as Visualized by Electron-Microscopic Immunocytochemistry and Autoradiography. Virology 160:220-226.
19. Rust RC, Landmann L, Gosert R, Tang BL, Hong WJ, Hauri HP, Egger D, Bienz K. 2001. Cellular COPII proteins are involved in production of the vesicles that form the poliovirus replication complex. Journal of Virology 75:9808-9818.
20. Schlegel A, Giddings TH, Jr., Ladinsky MS, Kirkegaard K. 1996. Cellular origin and ultrastructure of membranes induced during poliovirus infection. J Virol 70:6576-88.
21. Peddie CJ, Collinson LM. 2014. Exploring the third dimension: Volume electron microscopy comes of age. Micron 61:9-19.
22. van der Schaar HM, Melia CE, van Bruggen JA, Strating JR, van Geenen ME, Koster AJ, Barcena M, van Kuppeveld FJ. 2016. Illuminating the Sites of Enterovirus Replication in Living Cells by Using a Split-GFP-Tagged Viral Protein. mSphere 1.
23. Dales S, Eggers HJ, Tamm I, Palade GE. 1965. Electron Microscopic Study of the Formation of Poliovirus. Virology 26:379-89.

24. Belov GA, Sztul E. 2014. Rewiring of cellular membrane homeostasis by picornaviruses. J Virol 88:9478-89.
25. Roulin PS, Lotzerich M, Torta F, Tanner LB, van Kuppeveld FJM, Wenk MR, Greber UF. 2014. Rhinovirus Uses a Phosphatidylinositol 4-Phosphate/Cholesterol Counter-Current for the Formation of Replication Compartments at the ER-Golgi Interface. Cell Host & Microbe 16:677-690.
26. Strating JR, van der Linden L, Albulescu L, Bigay J, Arita M, Delang L, Leyssen P, van der Schaar HM, Lanke KH, Thibaut HJ, Ulferts R, Drin G, Schlinck N, Wubbolts RW, Sever N, Head SA, Liu JO, Beachy PA, De Matteis MA, Shair MD, Olkkonen VM, Neyts J, van Kuppeveld FJ. 2015. Itraconazole inhibits enterovirus replication by targeting the oxysterol-binding protein. Cell Rep 10:600-15.
27. van Meer G, de Kroon AI. 2011. Lipid map of the mammalian cell. J Cell Sci 124:5-8.
28. Blumental-Perry A, Haney CJ, Weixel KM, Watkins SC, Weisz OA, Aridor M. 2006. Phosphatidylinositol 4-phosphate formation at ER exit sites regulates ER export. Dev Cell 11:671-82.
29. Dorobantu CM, Albulescu L, Harak C, Feng Q, van Kampen M, Strating JR, Gorbalenya AE, Lohmann V, van der Schaar HM, van Kuppeveld FJ. 2015. Modulation of the Host Lipid Landscape to Promote RNA Virus Replication: The Picornavirus Encephalomyocarditis Virus Converges on the Pathway Used by Hepatitis C Virus. PLoS Pathog 11:e1005185.
30. Dorobantu CM, Harak C, Klein R, van der Linden L, Strating JR, van der Schaar HM, Lohmann V, van Kuppeveld FJ. 2016. Tyrphostin AG1478 Inhibits Encephalomyocarditis Virus and Hepatitis C Virus by Targeting Phosphatidylinositol 4-Kinase IIIalpha. Antimicrob Agents Chemother 60:6402-6.
31. van der Schaar HM, van der Linden L, Lanke KH, Strating JR, Purstinger G, de Vries E, de Haan CA, Neyts J, van Kuppeveld FJ. 2012. Coxsackievirus mutants that can bypass host factor PI4KIIIbeta and the need for high levels of PI4P lipids for replication. Cell Res 22:1576-92.
32. Xu K, Nagy PD. 2014. Expanding use of multi-origin subcellular membranes by positive-strand RNA viruses during replication. Curr Opin Virol 9:119-26.
33. Koopman R, Schaart G, Hesselink MK. 2001. Optimisation of oil red O staining permits combination with immunofluorescence and automated quantification of lipids. Histochem Cell Biol 116:63-8.
34. Deerinck TJ, Bushong E, Thor A, Ellisman M. 2010. NCMIR methods for 3D EM: A new protocol for preparation of biological specimens for serial block face scanning electron microscopy.
35. Russell MRG, Lerner TR, Burden JJ, Nkwe DO, Pelchen-Matthews A, Domart MC, Durgan J, Weston A, Jones ML, Peddie CJ, Carzaniga R, Florey O, Marsh M, Gutierrez MG, Collinson LM. 2017. 3D correlative light and electron microscopy of cultured cells using serial blockface scanning electron microscopy. Journal of Cell Science 130:278-291.

SUPPLEMENTAL FIGURES

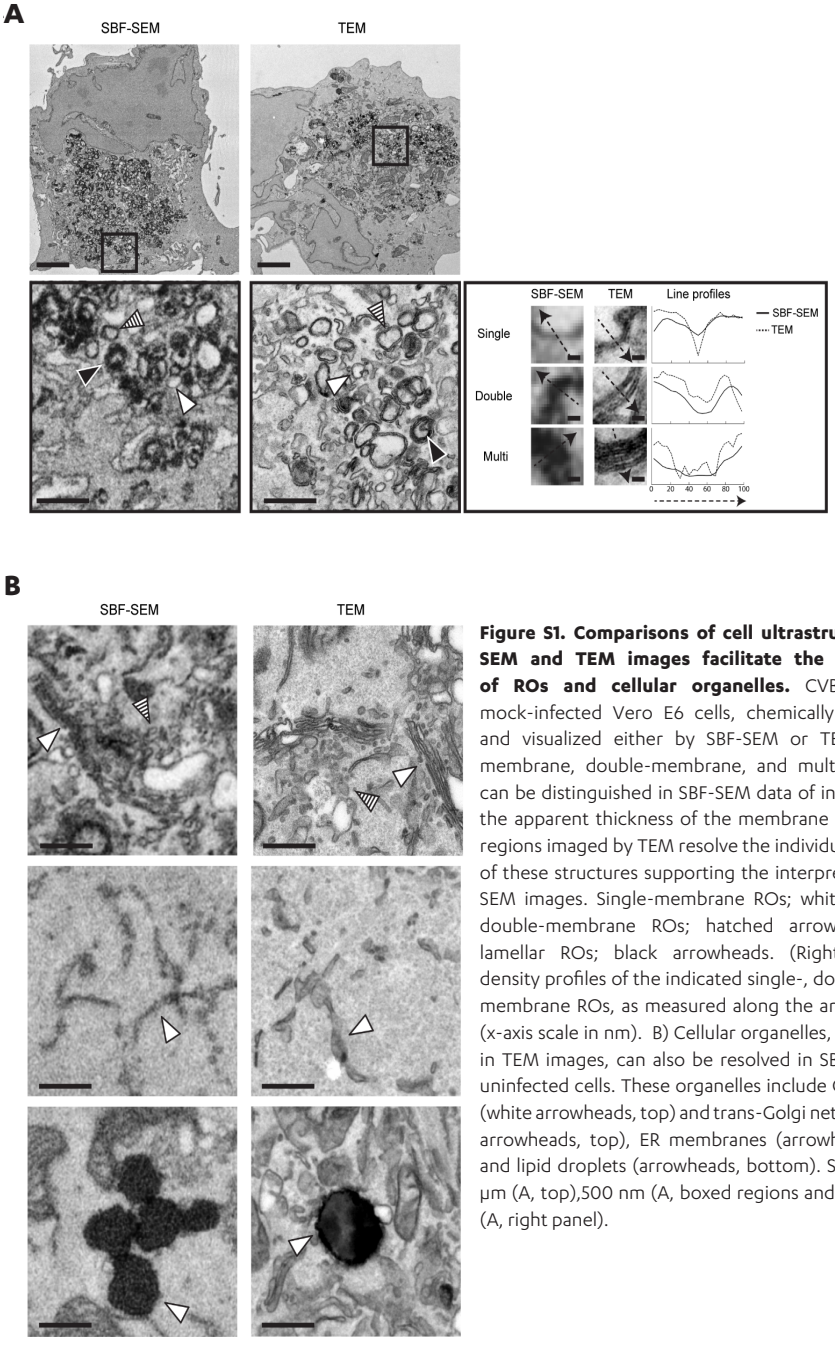


Figure S1. Comparisons of cell ultrastructure in SBF-SEM and TEM images facilitate the identification of ROs and cellular organelles. CVB3-infected or mock-infected Vero E6 cells, chemically fixed for EM and visualized either by SBF-SEM or TEM A) Single-membrane, double-membrane, and multi-lamellar ROs can be distinguished in SBF-SEM data of infected cells by the apparent thickness of the membrane profile. Similar regions imaged by TEM resolve the individual membranes of these structures supporting the interpretation of SBF-SEM images. Single-membrane ROs; white arrowheads, double-membrane ROs; hatched arrowheads, multi-lamellar ROs; black arrowheads. (Right panel) Line density profiles of the indicated single-, double- or multi-membrane ROs, as measured along the arrow directions (x-axis scale in nm). B) Cellular organelles, clearly distinct in TEM images, can also be resolved in SBF-SEM data in uninfected cells. These organelles include Golgi cisternae (white arrowheads, top) and trans-Golgi network (hatched arrowheads, top), ER membranes (arrowheads, middle) and lipid droplets (arrowheads, bottom). Scale bars are 2 µm (A, top),500 nm (A, boxed regions and B), and 20 nm (A, right panel).

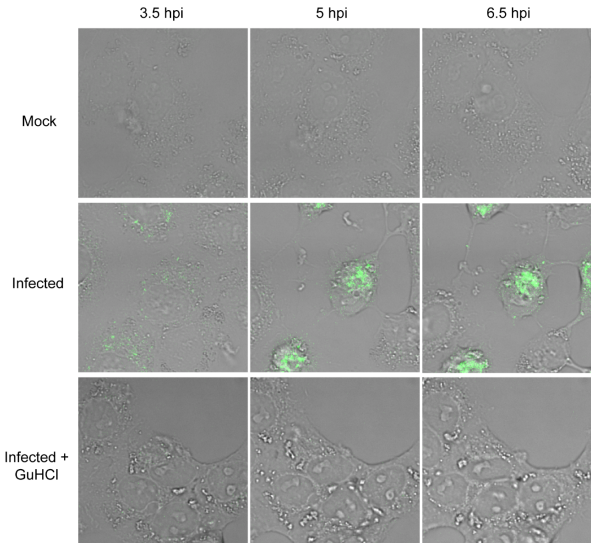


Figure S2. The appearance of 3A-GFP foci in the cell periphery requires viral replication. BGM(S1-10) cells were infected or mock-infected with CVB3 3A(S11). The addition of guanidine hydrochloride from 1 hpi, which blocks viral replication, prevented the formation of both peripheral and Golgi-associated 3A-GFP puncta.

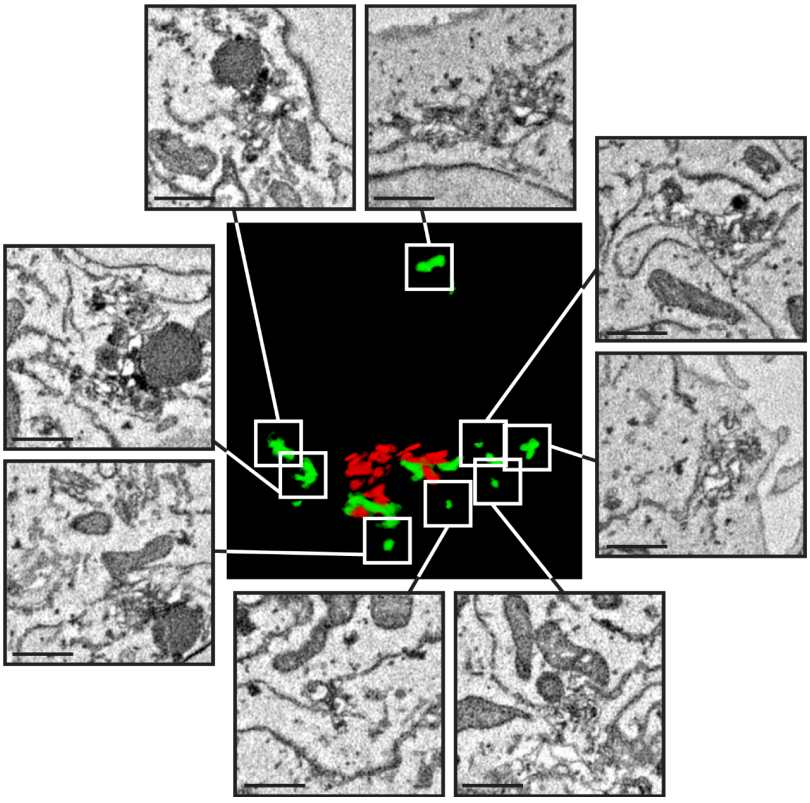


Figure. S3. Both ER-connected and Golgi-derived ROs co-exist in CVB3-infected cells. Analysis of the peripheral RO clusters detected in the SBF-SEM reconstruction of the cell shown in Fig. 4, which was fixed at an early stage of CVB3 infection. The analysis shows that these clusters (boxed regions) correspond to ER-associated ROs that can be formed in addition to the Golgi-derived ROs (see Fig. 4) observed in the same cell. Scale bars are 500 nm.

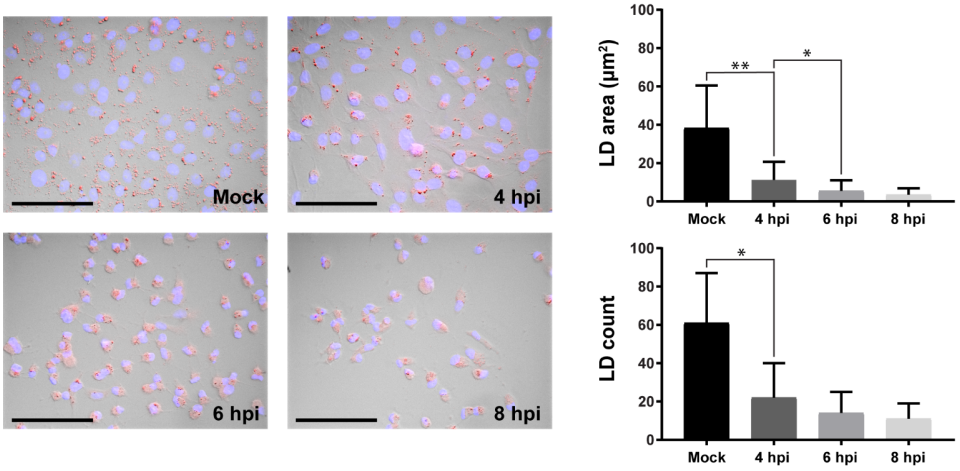


Figure. S4. Both ER-connected and Golgi-derived ROs co-exist in CVB3-infected cells. Analysis of the peripheral RO clusters detected in the SBF-SEM reconstruction of the cell shown in Fig. 4, which was fixed at an early stage of CVB3 infection. The analysis shows that these clusters (boxed regions) correspond to ER-associated ROs that can be formed in addition to the Golgi-derived ROs (see Fig. 4) observed in the same cell. Scale bars are 500 nm.

Movie S1. Large volume 3D reconstruction of CVB3-infected cells by SBF-SEM. Consecutive slices through SBF-SEM and segmentation volumes of a Vero E6 cell infected with CVB3 (cell shown in figure 1 and as cell A in figure 2, 6 hpi), highlighting the distribution of RO clusters (green) in their cellular context (nucleus, blue and cytoplasm, beige). Total reconstructed volume: 3404 µm3.

Movie S2. Live-cell imaging of CVB3-infected cells highlights peripheral and Golgi-associated viral 3A foci. BGM(S1-10) cells were transduced with mCherry-GM130 and infected with CVB3 3A(S11) (system described in (22)). As it is typically the case, the first 3A-GFP foci appear in the cell periphery (e.g., white arrowhead, ~4 hpi), shortly before 3A-GFP signal starts accumulating in the Golgi region (e.g. black arrowhead, ~4.5 hpi). The disintegration of the Golgi apparatus, apparent by the dispersion and loss of mCherry-GM130 signal, occurred from ~4.5 hpi through to ~5.5 hpi. Hatched arrowheads illustrate 3A-GFP foci migration between ~ 5 hpi and ~6 hpi. Scale bar is 10 µm.

Movie S3. The correlative light and serial block-face scanning electron microscopy workflow. BGM(S1-10) cells were transduced with mCherry-GM130 and infected with CVB3 3A(S11). Confocal z-stacks encompassing the volume of cells of interest were collected, followed by chemical fixation for EM processing and SBF-SEM. ROs, Golgi cisternae, and lipid droplets were manually segmented from the SBF-SEM volume and rendered in green, red and yellow respectively. Comparing both 3D renderings side by side allows establishing the correspondence between LM signal and specific structural motifs.

CHAPTER 5

THE ORIGIN, DYNAMIC MORPHOLOGY, AND PI4P-INDEPENDENT FORMATION OF ENCEPHALOMYOCARDITIS VIRUS REPLICATION ORGANELLES

C.E. Melia[1], H.M. van der Schaar[2], A.W.M. de Jong[1], H. R. Lyoo[2], E.J. Snijder[3], A.J. Koster[1], F.J.M. van Kuppeveld[2,&], M. Bárcena[1,&]

Published in mBio 2018. 9;2: e00420-18
DOI: 10.1128/mBio.00420-18

[1] Department of Cell and Chemical Biology, Section Electron Microscopy, Leiden University Medical Center, Leiden, The Netherlands

[2] Department of Infectious Diseases & Immunology, Virology Division, Faculty of Veterinary Medicine, Utrecht University, Utrecht, The Netherlands

[3] Department of Medical Microbiology, Molecular Virology Laboratory, Leiden University Medical Center, Leiden, The Netherlands

[&]These authors contributed equally

SUMMARY

Picornaviruses induce dramatic rearrangements of endomembranes in the cells that they infect to produce dedicated platforms for viral replication. These structures, termed replication organelles (ROs), have been well characterized for the Enterovirus genus of the Picornaviridae. However, it is unknown whether the diverse RO morphologies associated with enterovirus infection are conserved among other picornaviruses. Here, we use serial electron tomography at different stages of infection to assess the three-dimensional architecture of ROs induced by encephalomyocarditis virus (EMCV), a member of the Cardiovirus genus of the family of picornaviruses that is distantly related. Ultrastructural analyses revealed connections between early single-membrane EMCV ROs and the endoplasmic reticulum (ER), establishing the ER as a likely donor organelle for their formation. These early single-membrane ROs appear to transform into double-membrane vesicles (DMVs) as infection progresses. Both single- and double-membrane structures were found to support viral RNA synthesis, and progeny viruses accumulated in close proximity, suggesting a spatial association between RNA synthesis and virus assembly. Further, we explored the role of phosphatidylinositol 4-phosphate (PI4P), a critical host factor for both enterovirus and cardiovirus replication that has been recently found to expedite enterovirus RO formation rather than being strictly required. By exploiting an EMCV escape mutant, we found that low-PI4P conditions could also be overcome for the formation of cardiovirus ROs. Collectively, our data show that despite differences in the membrane source, there are striking similarities in the biogenesis, morphology, and transformation of cardiovirus and enterovirus ROs, which may well extend to other picornaviruses.

IMPORTANCE

Like all positive-sense RNA viruses, picornaviruses induce the rearrangement of host cell membranes to form unique structures, or replication organelles (ROs), that support viral RNA synthesis. Here, we investigate the architecture and biogenesis of cardiovirus ROs and compare them with those induced by enteroviruses, members of the well-characterized picornavirus genus Enterovirus. The origins and dynamic morphologies of cardiovirus ROs are revealed using electron tomography, which points to the endoplasmic reticulum as the donor organelle usurped to produce single-membrane tubules and vesicles that transform into double-membrane vesicles. We show that PI4P, a critical lipid for cardiovirus and enterovirus replication, is not strictly required for the formation of cardiovirus ROs, as functional ROs with typical morphologies are formed under phosphatidylinositol 4-kinase type III alpha (PI4KA) inhibition in cells infected with an escape mutant. Our data show that the transformation from single-membrane structures to double-membrane vesicles is a conserved feature of cardiovirus and enterovirus infections that likely extends to other picornavirus genera.

INTRODUCTION

The cardioviruses comprise an important genus of the Picornaviridae family of positive-sense RNA (+RNA) viruses. The type species Cardiovirus A, or encephalomyocarditis virus (EMCV), ostensibly infects mice, but is capable of infecting a range of mammals including humans. Severe disease in

wild or farm animals occurs primarily in swine (1, 2), but concerns for human safety have followed from studies demonstrating the potential for pig to human EMCV transmission during organ xenotransplantation (3, 4), which will become more imminent as the technique matures. The Cardiovirus B species is represented by Theiler's murine encephalomyocarditis virus (TMEV), the study of which has led to critical contributions to our understanding of demyelinating diseases (reviewed in (5)). Unlike TMEV, the closely related Saffold virus is capable of infecting humans. Saffold virus was discovered only recently in a patient with a fever of unknown origin (6), but appears to be widespread and commonly found in co-infections with other viruses. Among these co-infected viruses are the enteroviruses (7, 8), another genus of picornaviruses that includes poliovirus, the coxsackieviruses, rhinoviruses, and enteroviruses A71 and D68. Although the consequences of enterovirus and Saffold virus infections in co-infected patients are entwined, there are suggestions that Saffold virus could cause or contribute to diseases as diverse as gastroenteritis, encephalitis, myocarditis and non-polio acute flaccid paralysis (reviewed in (9)), which are typically associated with enterovirus infections.

Understanding the conserved requirements for picornavirus replication is an important strategy for developing broadly acting antiviral therapies. Currently, vaccines are available to prevent infections with hepatitis A virus, poliovirus, and EV71 (only available in China), but there are no approved antiviral therapies to treat picornavirus infections. Substantial efforts have been invested in developing directly-acting antivirals that target viral proteins, but the spectrum of antiviral activity of these agents is limited (10-12). Another strategy, for which interest has been growing in recent years, is the development of inhibitors targeting host factors that are conserved amongst different genera (13). One host factor required for the replication of both enteroviruses and cardioviruses is the lipid phosphatidylinositol-4 phosphate PI4P. Cellular production of PI4P is orchestrated by phosphatidylinositol-4 kinases (PI4Ks), which reside in various subcellular compartments and generate local pools of PI4P (reviewed in (14) and (15)). Enteroviruses rely upon the III beta class of PI4K (PI4KB) (16, 17), which predominantly localises to the Golgi apparatus, while cardioviruses require the largely ER-based III alpha class of PI4K (PI4KA) (18). Interestingly, like for cardioviruses and enteroviruses, PI4P is also required by the more distantly-related hepatitis C virus (HCV), which depends upon PI4KA for its replication (19).

A role for PI4P in expediting the formation of enterovirus replication organelles (ROs) has recently been described (20), which could in part explain its importance during viral replication. ROs are virus-induced membrane rearrangements formed during infections of all eukaryote-infecting +RNA viruses. These structures serve as a hub for viral replication in the cell, and their unique properties are believed to confer intrinsic benefits to the viruses that generate them. The expansion of membranes that support the viral RNA synthesis machinery may increase replication efficiency, while the unique morphology of some ROs could serve to compartmentalise this process or its products, and limit host innate immune sensing. The 3D morphology of enterovirus ROs is well characterised. Early in infection enteroviruses induce the formation of single-membrane tubular ROs that gradually transform into double-membrane vesicles and multilamellar vesicles over the course of infection (21, 22). Our understanding of cardiovirus ROs, however, is more limited. Different studies have identified single- or double-membrane structures using 2D electron microscopy (EM) of chemically fixed samples (23-25), and it is unclear whether these disparate observations reflect differences in sample preparation or truly distinct structures, perhaps found at different stages

of infection. It remains to be established how membrane modifications arise and develop across cardiovirus infection, what their 3D morphology is, which structures are capable of supporting RNA synthesis and, furthermore, whether PI4KA plays a role in cardiovirus RO formation.

Here, we use serial electron tomography (ET) to unravel the 3D morphology of EMCV ROs across an extensive time course that encompasses their formation and development. Samples were prepared using high-pressure freezing and freeze substitution (HPF-FS) as an alternative to chemical fixation, which better preserves structures sensitive to artefacts. We provide evidence that early EMCV ROs consist of single-membrane tubules and vesicles that emerge from the ER. These single-membrane structures, which emerge during the exponential phase of viral RNA synthesis, appear to serve as the primary platform for genome replication. However, double-membrane vesicles (DMVs), which largely emerge later in infection, were also capable of supporting RNA synthesis. Remarkably, putative transition states between single-membrane tubules and DMVs were found that mirror the transformation intermediates observed for enterovirus ROs (21). This chronological progression of RO morphology contextualises the previous observations of single- or double-membrane EMCV ROs, and represents a striking parallel between cardiovirus and enterovirus DMV formation that may represent a conserved mechanism amongst picornaviruses. Given this cohesion in RO morphology between enteroviruses and EMCV, we then investigated whether PI4KA plays a role in the formation of EMCV ROs, like PI4KB does for enterovirus ROs (20). To this end, we studied the effects of PI4KA inhibition on an EMCV mutant that harbours a single substitution in its 3A protein (3A-A32V), which confers resistance to PI4KA inhibitors (26). Intriguingly, PI4KA inhibition neither affected RO morphology nor significantly delayed RO formation. This indicates that, similarly to enteroviruses, a lack of high PI4P levels does not pose an unsurmountable barrier for cardiovirus RO formation.

RESULTS

EMCV-induced membrane rearrangements with different morphologies arise over the course of infection

We first set out to determine the relationship between EMCV replication and the emergence of ROs. Samples for qPCR, viral titer determination, immunofluorescence analysis and electron microscopy (chemical fixation) were generated within a single experiment. HeLa cells infected with EMCV (strain Mengovirus) at MOI 50 were processed every hour up to 9 hours post-infection (hpi) for quantitative PCR (qPCR) of viral RNA and for the determination of viral titer. Samples for immunofluorescence and electron microscopy (EM) analyses were fixed between 3 and 9 hpi. While data from these chemically fixed EM samples were assessed to quantify the emergence of ROs, representative images are presented from a subsequent experiment using an improved sample preparation method (high-pressure freezing and freeze substitution) that more faithfully preserves RO morphology. The exponential phase of RNA synthesis spanned 3 to 6 hpi, while the increase in viral titer lagged by ~2 hours (Fig. 1A). These RNA replication dynamics aligned well with increasing dsRNA immunofluorescence signal, which provides a secondary indication of viral replication. The first fluorescent signal was detected at 4 hpi and levels increased steadily each hour before reaching a plateau at 7 hpi. Between 4 and 5 hpi, dsRNA signal was found at small foci distributed throughout the cytoplasm, which became larger and more clustered as infection

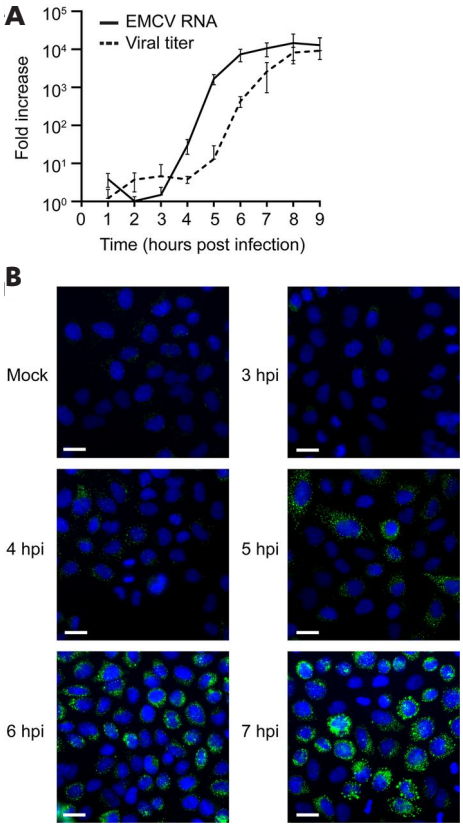


Figure 1. The kinetics of EMCV replication and progeny virus production. HeLa cells were infected or mock-infected with EMCV. A) Cells were lysed every hour between 1 and 9 hpi to determine viral RNA levels by qPCR or to determine viral titer by titration. Values, converted to fold increase, represent the mean of triplicates (± std. error). B) The subcellular distribution of dsRNA (green) relative to the cell nucleus (blue) was assessed by immunofluorescence analysis every hour between 3 and 9 hpi (3 to 7 hpi shown). Scale bars are 20 µm.

progressed (Fig. 1B).

The first virus-induced membrane modifications were detected in EM cell-sections of cells fixed at 5 hpi, revealing a complex but sparse assortment of virus-induced single-membrane structures (Fig. 2A, arrowheads) and, very occasionally, double-membrane structures (Fig. 2A, asterisk). From 6 hpi membrane modifications became increasingly clustered into large regions that dominated the cytosol, and the abundance of double-membrane structures increased (Fig. 2B, asterisks), although single-membrane structures persisted (Fig. 2B, arrowheads). Late in infection double-membrane vesicles became more dominant (Fig. 2C, white asterisks), and multi-lamellar structures were also found (Fig. 2C, black asterisks and inset). Between 5 and 8 hpi, the RO density in the cytoplasm greatly increased (from 0.11 to 0.63 ROs per µm2), and the proportion of DMVs (as a percentage of total ROs) grew from less than 1% to an average of 35%, although in some cells DMVs rather than single-membrane structures were the predominant RO morphology (Fig. 2D). A number of cells with evident signs of lysis (e.g. disrupted plasma membrane, extracted cytosolic content) could also be found later in infection, which may explain the lack of immunofluorescence labelling in some cells by 7 hpi.

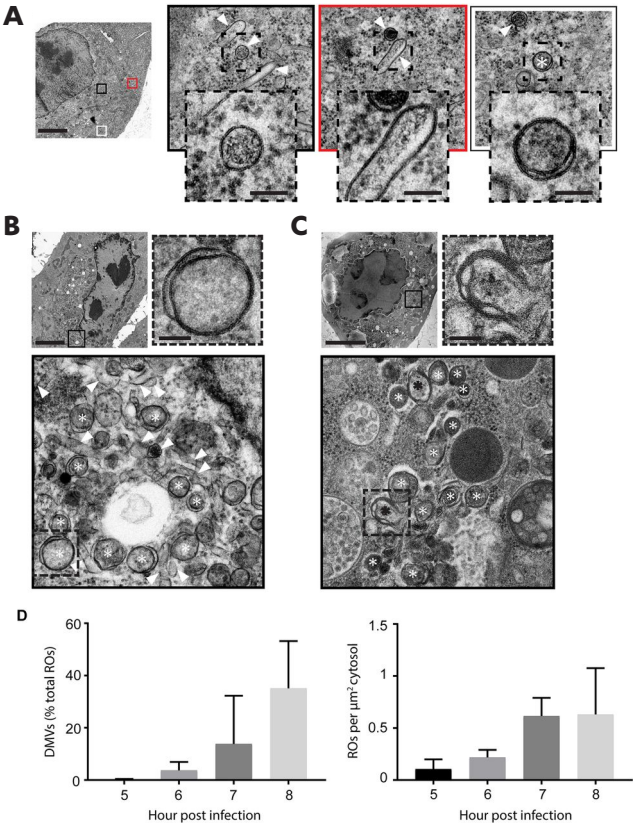


Figure 2. 2D EM reveals single-, double-membrane and multilamellar structures. An initial 2D EM analysis to assess the emergence and development of EMCV ROs was performed using chemically fixed HeLa cells processed in parallel with samples described in Fig. 1 (Fig. 2D). Corresponding structures in high-pressure frozen and freeze-substituted samples are shown (Fig. 2A-C). Single-membrane structures are indicated with arrowheads. Double-membrane structures are marked with a white asterisk. A) Membrane rearrangements found at early infection time points (~5 hpi) were primarily single-membrane structures, but some double-membrane structures were also observed. B) Later in infection (~6 hpi) the membrane rearrangements became more clustered and the relative abundance of double-membrane structures increased. C) At late infection time points (~7 hpi) double-membrane structures were predominant and multilammellar membrane structures were found (black asterisks). D) The relative abundance of double-membrane vesicles in EMCV-infected chemically-fixed cells was analysed between 5-8 hpi (left). Increase in total ROs over this period expressed as RO counts per µm2 of cytoplasm (right). Total RO count from 5-8 hpi = 4365, 5 cell sections randomly selected and analysed per time point. The bars represent standard deviations. A, B, C) Scale bars are 5 µm (unboxed images) or 100 nm (dashed-line boxed images).

Electron tomography reveals the 3D architecture and transformation of ROs

One drawback of 2D EM cell-section analysis is the similarity in cross-section between vesicles and tubules running perpendicular to the section plane. Additionally, features like membrane connections or small openings may be obscured by the superposition of structures in a 2D projection image. To more unambiguously characterise the morphology of EMCV ROs, cells at early and late stages of infection were prepared for electron tomography (ET). Tomograms from serial cell-sections of the same region of interest were combined to form large 3D volumes for analysis.

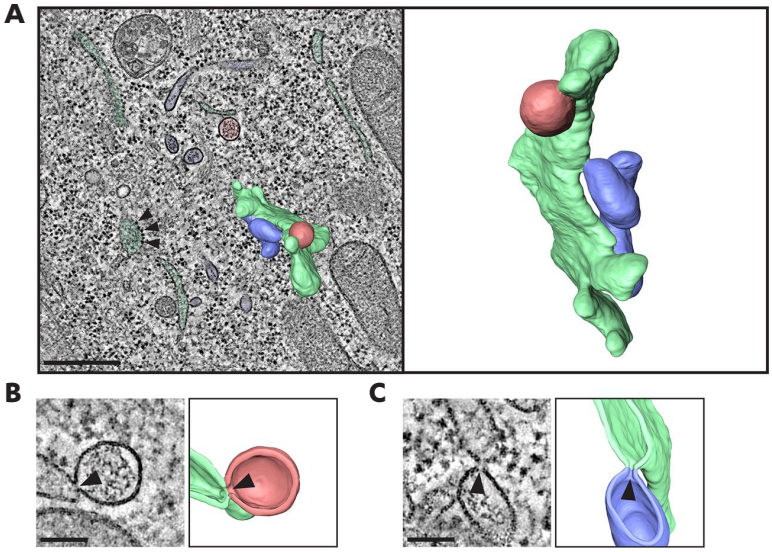


Figure 3. Tomography of EMCV infected cells at 5 hpi reveals connections between single-membrane ROs and ER. HeLa cells were infected with EMCV and high-pressure frozen at 5 hpi for EM processing and serial tomography. Shown are different features observed in a serial tomogram comprising five consecutive sections of 200 nm thickness from a representative cell. A) Section through the tomogram volume showing SMVs in red, SMTs in blue and ER in green, recognisable by the membrane-associated ribosomes (arrowheads), with a segmentation of a sub-region of the volume superimposed (left) and in isolation (right). B, C) Sections through the tomogram alongside their corresponding 3D model cutaway reveal connections between SMVs (red) and ER (green) (B), and SMTs (blue) and ER (C). The site of the connection is indicated with a black arrowhead. Scale bars are 500 nm (A) or 100 nm (B and C).

Single-membrane structures identified in the 2D analysis at early times post-infection were found to comprise a mixed population of single-membrane vesicles (SMVs) and single-membrane tubules (SMTs) (Fig. 3A, red and blue respectively, Movie S1). Unlike the tubules formed during enterovirus infections, EMCV SMTs did not form tightly packed clusters. Both SMVs and SMTs were smooth-membrane structures, and were frequently found connected to rough ER (green) by neck-like membrane connections (Fig. 3B and C, arrowheads), like the ER-derived ROs of nidoviruses (27-29) and HCV (30). In contrast, DMVs, which were predominantly found at late stages of infection, appeared in all instances to be separate compartments, with no membrane connections to other structures (Fig. 4A, yellow, Movie S2). Some DMVs appear to be partially enwrapped by additional cisternae late in infection (Fig. 4B, purple), to form multilamellar structures. Virus particles were also detectable in the EM data as dense hexagonal profiles of ~25 nm (Fig. 4C, arrowhead), which were frequently found in the cytosol within 30 nm of ROs (Fig. S1). These particles (Fig. 4D, black arrowhead) were distinguishable from ribosomes (Fig. 4D, white arrowhead) by their symmetry and well-defined edges. A closer spatial association was found between virus particles and RO membranes (SMVs, SMTs or DMVs) than between randomly generated co-ordinates and RO membranes (Fig S1, $p < 0.001$). This could reflect localised clustering of virions following their formation, or a spatial connection between RNA synthesis and virion assembly.

Ultrastructural investigations of enterovirus ROs have revealed putative transition structures that may represent the transformation of SMTs into DMVs. This process appears to involve the pairing of membrane tubules to form flattened cisternae, which curve to enwrap a small volume of cytosol,

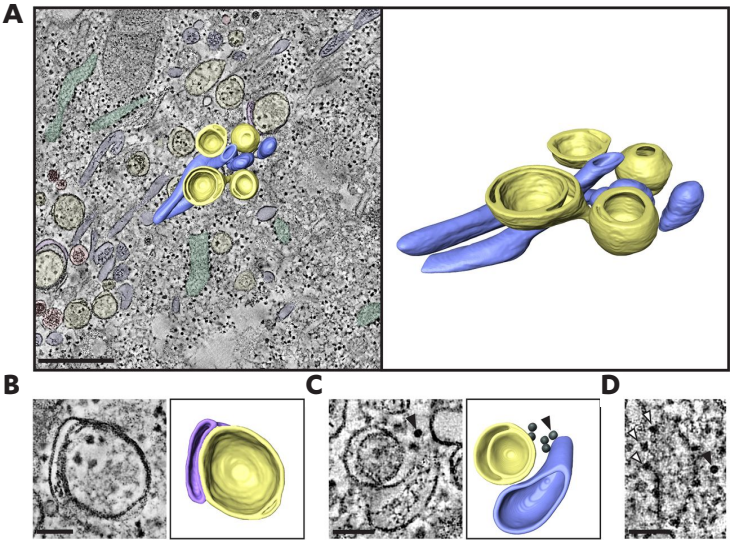


Fig. 4. Tomography of EMCV infected cells at 7 hpi highlights virions proximal to DMVs and multilamellar vesicles. HeLa cells were infected with EMCV and high-pressure frozen at 7 hpi for EM processing and tomography. Shown are structures observed in a serial tomogram comprising two consecutive sections of 200 nm thickness from a representative cell at this time point. A) Section through the tomogram and corresponding model showing SMTs in blue, SMVs in red, ER in green, DMVs in yellow and cisternae enwrapping DMVs in purple, with a segmentation of a sub-region of the volume superimposed (left) and in isolation (right) highlighting SMTs and DMVs. B, C) Sections through tomograms and corresponding models showing a multilamellar vesicle, which consists of a closed DMV (yellow) enwrapped by a flattened cisterna (purple) (B), and highlighting the proximity of viral particles (black) in the cytosol to ROs (yellow and blue) (C). Virus particles are indicated with an arrowhead. D) Comparison of ribosome (white arrowheads) and virus particle (black arrowhead) morphology in a single tomogram section. Scale bars, 500 nm (A) or 100 nm (B, C and D).

ultimately forming an open DMV in a vase-like configuration. The opening then seals to form a complete, closed DMV (21, 22). Similar structures were found in tomograms of EMCV infected cells, including paired and highly curved tubules (Fig. 5A i. and ii., white arrowheads), which could represent an early stage of DMV formation from SMTs, and DMVs with small openings (Fig. 5A iii., arrowhead). Tubular extensions of the outer membranes of DMVs were also found (Fig. 5B, indicated by white arrowheads in consecutive sections) that could represent the partial transformation of SMTs to DMVs. Supporting this idea, similar electron-dense material was observed both in the lumen of single-membrane structures (Fig. 5A black arrowheads), and within the inter-membrane space created by these tubular extensions (Fig. 5B, black arrowhead). To further examine the possibility of a single- to double-membrane structure transformation, the surface areas of SMVs, SMTs and DMVs were estimated using the measured average diameter for each structure (Fig. 5C, top). These figures provide a guide as to whether SMTs or SMVs are likely candidate precursor structures for DMVs (as described in (21)) as, unless other lipid sources contribute to DMV membranes, any precursor structure should have at least the same surface area than the DMV that forms from it. The estimated surface areas generated allow for a scenario where DMVs are formed by SMTs (Fig. 5C, bottom), and are compatible with the possibility that some (smaller) DMVs could also be derived from SMVs. In this scenario, the multilamellar vesicles seen at late time points may arise from SMTs that enwrap or partially enwrap existing DMVs, rather than enwrapping the cytosol

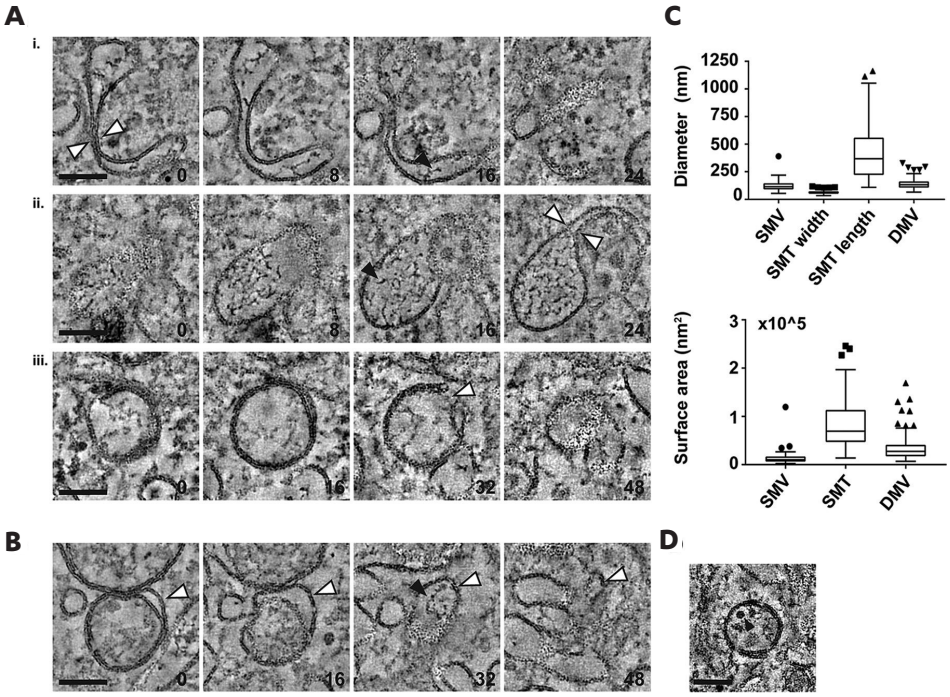


Fig. 5. Intermediate structures suggest that single-membrane structures transform into DMVs. Intermediate structures found in EMCV-infected HeLa cells at 7 hpi. The slice thickness is 1.24 nm, and the slice spacing (A, B) is indicated in the lower right corner of consecutive images. Black arrowheads indicate electron-dense material present in the lumen of SMTs and between the inner and outer membranes of DMVs. A) Membrane curving and pairing of single membrane structures (white arrowheads, i. and ii.), and a DMV with an opening to the cytosol (white arrowhead, iii.). B) DMV with a tubular extension of its outer membrane (indicated by white arrowheads). C) Tukey plots showing the distribution of diameters (left) and surface areas (right) of ROs. Median diameter values (nm) are 115 (SMV, n = 90), 62 (SMT width, n = 90), 368 (SMT length, n = 90) and 132 (DMV, n = 130). D) Example of a virus particle (black arrowhead) enclosed within a DMV. Scale bars are 100 nm.

to form a new DMV. DMVs were occasionally found to contain virions in samples analysed at 7 hpi (pooled data from four tomograms, example shown in Fig. 5D), but at a low frequency (7% of 68 DMVs), and particles within DMVs represented a small fraction of total virus particles detected (2% of 339 particles). An enwrapping mechanism of SMT-to-DMV transformation could explain the presence of virus particles within a subset of DMVs, as virions may be enclosed by chance during their formation.

RNA synthesis occurs at virus-induced single- and double-membrane structures

To investigate whether all or some of these virus-induced membrane modifications support RNA synthesis, metabolic labelling and EM autoradiography (31) was performed. Cells were infected with EMCV and fixed at 5 or 7 hpi. During the 2 hours prior to fixation, cells were incubated with 10 µg/ml dactinomycin to limit cellular transcription. During the 45 minutes prior to fixation, cells were additionally treated with tritiated uridine to label newly-synthesised RNA. After chemical fixation and preparation for EM, sections were prepared for autoradiography.

While only larger clusters of electron-dense grains are good indicators of underlying viral RNA

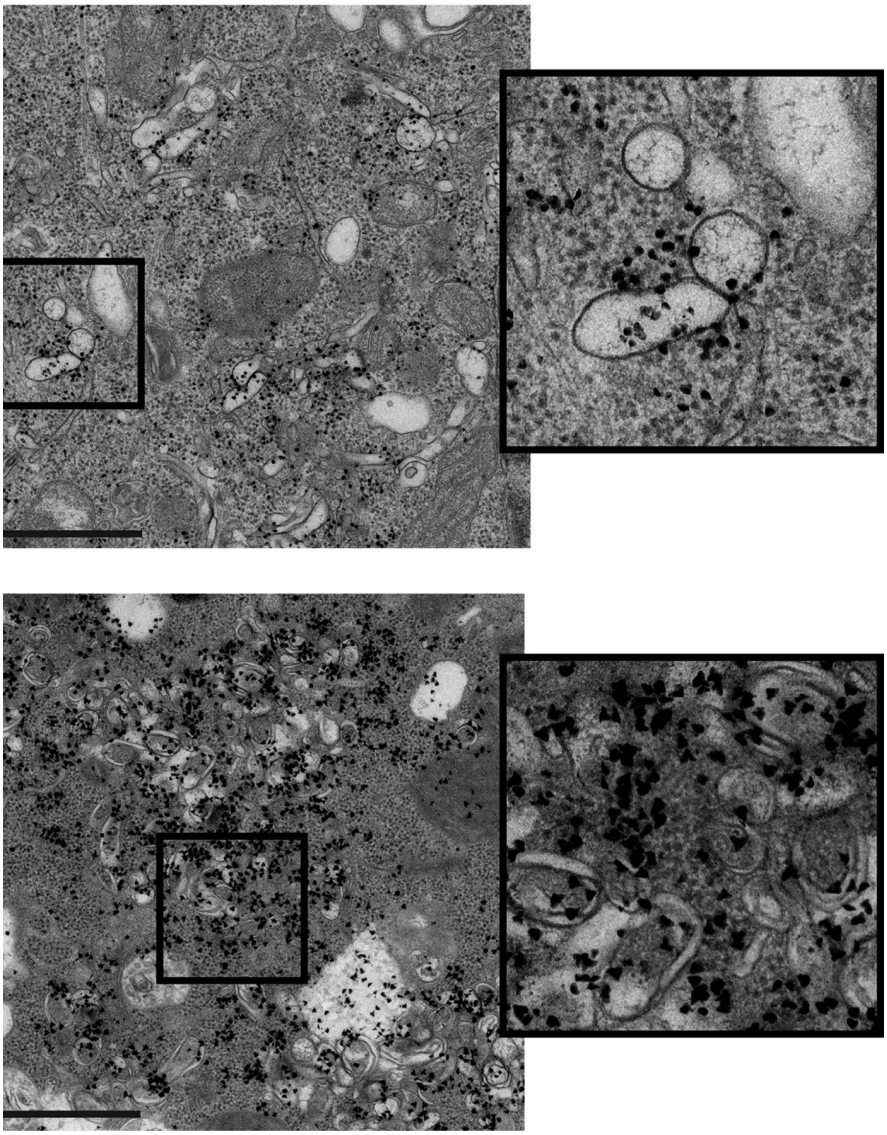


Fig. 6. RNA synthesis occurs at single- and double-membrane structures. HeLa cells were infected with EMCV, metabolically labelled with tritiated uridine in the presence of dactinomycin, chemically fixed at 7 hpi and processed for EM-autoradiography to detect the subcellular location of newly-synthesised viral RNA in 2D EM cell-sections. A) Cells at early stages of infection revealed autoradiography signal (electron-dense grains) clustered around areas with single-membrane structures. B) In cells at late stages of infection autoradiography signal was found at RO clusters primarily comprised primarily of double-membrane structures. Scale bar is 2 µm.

synthesis given the limited resolution of EM autoradiography (32), substantial autoradiography signal could be found clustered around areas containing exclusively single-membrane tubules and vesicles (Fig. 6A). This demonstrates their ability to support viral RNA synthesis. Newly-synthesised RNA was also evident at RO foci comprised predominantly of DMVs at later stages of infection (Fig.

6B), indicating that the transformation from single-membrane structure to DMV does not impede continued genome replication.

PI4KA inhibition of a PI4K-resistant EMCV mutant does not alter RO development or morphology

While there may be divergence in the origins of enterovirus and cardiovirus ROs, the development of SMTs that transform into DMVs appears to be a common feature of both. We next investigated whether common requirements for RO biogenesis might also exist between enteroviruses and cardioviruses. Specific roles for the enterovirus host factor PI4KB, a PI4P-generating kinase, have recently been identified. In addition to facilitating efficient polyprotein processing (20, 33-35), PI4KB

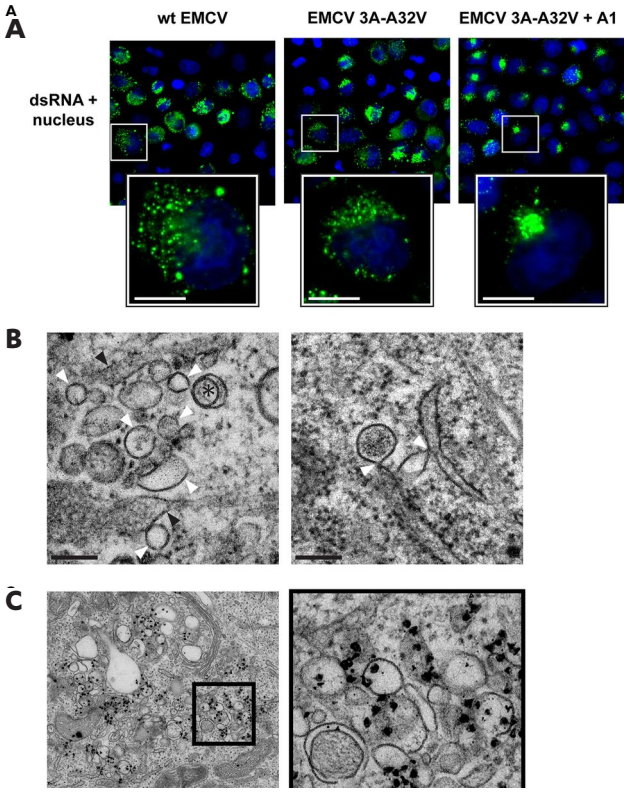


Fig. 7. RO development during EMCV 3A-A32V infection under PI4KA inhibition. HeLa cells were infected with wt EMCV or EMCV 3A-A32V and chemically fixed at 5 or 7 hpi. A) Immunofluorescence labelling reveals a dense perinuclear distribution of dsRNA in cells infected with EMCV 3A-A32V and treated with a PI4KA inhibitor A1, compared to wt EMCV or EMCV 3A-A32V infections without inhibition. Cells were fixed at 7 hpi. Nuclei (blue) and dsRNA distributions (green) are shown. B) Single membrane structures (white arrowheads) and double-membrane structures (asterisk) could be found in infections of EMCV 3A-A32V under PI4KA inhibition that resembled those of wt EMCV (left, 7 hpi). Connections between single-membrane ROs and the ER (arrowheads) could also be found (right, 5 hpi). C) Cells were infected with EMCV 3A-A32V, treated with PI4KA inhibitor, metabolically labelled, chemically fixed at 7 hpi and processed for EM-autoradiography to detect the subcellular location of newly-synthesised viral RNA in 2D EM cell-sections. Autoradiography signal (electron-dense grains) accumulated at RO clusters, similar to observations of wt EMCV infection. Scale bars are 10 µm (A) 200 nm (B) or 1 µm C).

accelerates the formation of enterovirus ROs (20). To investigate possible roles during EMCV RO formation of PI4KA, an essential PI4P-generating kinase for cardiovirus replication, we utilised the 3A-A32V mutant (26). This mutant, generated through serial passaging of wt EMCV in cells with a stable knock down of PI4KA, is capable of establishing replication even in the presence of the PI4KA inhibitor A1. At a concentration of 10 nM this compound potently inhibits wt EMCV replication in HeLa cells, with no effect on cell viability (26).

In the absence of A1 treatment, infections of the EMCV 3A-A32V mutant in HeLa cells produced ROs whose morphology was indistinguishable from those of wt EMCV (Fig. S2). SMTs and SMVs predominated at earlier time points, while DMVs were found only occasionally (Fig. S2A, asterisk). Later in infection, DMVs proliferated and ROs became more clustered (Fig. S2B, DMVs indicated by asterisks). Together, these results indicate that the 3A-A32V substitution does not affect RO development or their general architecture. PI4KA inhibition under A1 treatment led to a more clustered, perinuclear dsRNA signal compared to uninhibited infections of EMCV 3A-A32V or wt EMCV (Fig. 7A) (26). Despite this different staining pattern under PI4KA inhibition, the morphology of ROs and time post-infection at which ROs were first detected were not affected. EMCV 3A-A32V infection under PI4KA inhibition produced single- and double-membrane cardiovirus ROs (Fig. 7B, left, white arrowheads and asterisks respectively), typically in proximity to the ER (black arrowheads). Importantly, while the clustered dsRNA signal found under inhibition partially localized in the perinuclear Golgi region (Fig S3), connections between single-membrane ROs and the ER were still found (Fig. 7B, right, white arrowheads), and ROs produced under PI4KA inhibition also retained their ability to support RNA synthesis (Fig. 7C). Taken together, our data demonstrate that, while PI4KA/PI4P availability may govern the subcellular location of EMCV ROs, it does not significantly affect their emergence, morphology, or ability to serve as platforms for viral RNA synthesis.

DISCUSSION

Here we reveal the 3D morphology of cardiovirus ROs, and present a comprehensive overview of their formation and development throughout infection. At early stages of EMCV infection virus-induced SMTs and SMVs were found, which appear to transform into DMVs over the course of infection. This progression bears a striking resemblance to that of enterovirus ROs, suggesting a universal mechanism for DMV formation in picornaviruses. Despite differences in the cellular origins of enterovirus and cardiovirus ROs, our data establish that escape mutants from both genera are able to bypass any role of PI4P in RO formation.

Single-membrane ROs predominated at early stages of EMCV infection, which were capable of supporting viral RNA synthesis. Interestingly, while enteroviruses invariably produce SMTs early in infection (21, 22), also in HeLa cells (22), EMCV produced both SMTs and SMVs. These structures were of different sizes, and did not form packed clusters like the SMTs of enteroviruses. Many of the SMTs and SMVs visualised at early stages of infection were also found connected to the ER, providing compelling evidence that cardiovirus ROs are ER-derived. This finding is supported by the reported reliance of cardioviruses on ER-associated proteins like PI4KA, and the observed co-localisation of calreticulin and RO-associated viral proteins (18). Unlike cardioviruses, enteroviruses depend on Golgi-based proteins like PI4KB and GBF1 (16, 17, 36), and likely utilise membranes of

the Golgi apparatus to generate their ROs. Interestingly, membrane connections between donor organelle and enterovirus ROs were not detected in the tomographic characterisation studies (21, 22), suggesting that the process of initial enterovirus RO budding and release from the donor organelle is rapid compared to that of cardioviruses.

Despite these divergences in origin and morphology, our findings suggest that the transformation of single-membrane ROs into DMVs is conserved amongst enteroviruses and cardioviruses. For both genera, DMV formation appears to occur via membrane pairing of single-membrane ROs to form curved cisternae that ultimately enwrap small volumes of cytosol (21, 22). Given that transport from the DMV interior to the cell cytosol across the double membrane of a closed DMV is problematic, these structures may represent a means of sequestering viral products at late stages of infection. Interestingly, a small population of DMVs were also found with openings to the cytosol. While these open DMVs could reflect an intermediate step in their transformation from single-membrane structures to closed DMVs, it is also possible that a small population of DMVs retain openings to the cytosol for the duration of infection. Given that viral replication is likely to occur on the cytosolic face of early single-membrane ROs (37, 38), the interior of open DMVs could represent a shielded environment for replication at later stages of infection, with access to the cytosol for virion packing and/or export. A similar mechanism could also underlie the formation of the sparse double-membrane structures among abundant single-membrane structures identified in 2D EM investigations of foot and mouth disease virus infection (genus Apthovirus) (39), and may represent the means by which DMVs form during infections of Picornaviridae more broadly. Evidence for a similar mechanism for DMV biogenesis has been presented for the arterivirus equine arteritis virus and MERS coronavirus (order Nidovirales), which in this case would not occur through single-membrane intermediate ROs but by direct pairing and curving of the ER membranes (40, 41). While this enwrapping mechanism could represent a general route for DMV RO formation in +RNA viruses, it is intriguing that DMV formation is possible both via enwrapping of Golgi- or ER-derived single-membrane ROs in the case of picornaviruses, or via direct enwrapping of cytosol by ER membranes in the case of nidoviruses. The formation of DMVs from these diverse progenitor membranes could suggest that their development depends primarily on viral machinery or recruited host factors. The cellular functions of these host factors may also provide clues about their functions during infection. For instance, LC3 has been found in conjunction with enterovirus ROs (42, 43). In uninfected cells, lipidated LC3 is hypothesised to induce the membrane curvature underlying omegasome formation during autophagy (44), and its recruitment to enterovirus ROs could suggest a similar role in the formation of DMVs, whose development appears to resemble that of autophagosomes.

While direct actors have yet to be established, it is likely that cardiovirus RO formation is dependent upon specific, membrane-associated host factors. PI4P is an essential lipid for the replication of picornaviruses (16, 18, 45) and is generated at the ER or the Golgi apparatus by PI4KA and PI4KB respectively. Interestingly, PI4Ks are also important for HCV replication, where they appear to play a role in RO formation (19, 46). Expression of a mutated HCV NS5A, whose ability to recruit PI4KA is impaired, has been shown to produce ROs with irregular morphologies (19). A role for PI4Ks during RO biogenesis has also been demonstrated for enteroviruses, as RO formation was delayed under PI4KB inhibition during infections of the PI4KB inhibitor-resistant virus CVB3 3A-H57Y. Under these conditions RO were not detected at the peak of viral RNA synthesis, and this process occurred

instead on apparently intact Golgi membranes (20). In our study, PI4KA inhibition shifted the subcellular distribution of EMCV dsRNA, but did not affect the time post-infection at which ROs were first detected or alter their observed morphology, connectivity with the ER or competence to support viral RNA synthesis. These different observations in the two genera could arise from differences in the efficiency of the escape mechanism conferred by the specific resistance mutations, or alternatively suggest that, unlike for enteroviruses, PI4P does not play a significant role in cardiovirus RO formation. In either case, both mutants were able to (ultimately) produce ROs with normal morphology under PI4K inhibition, showing that any role of high PI4P levels in RO formation can be circumvented by members of both picornavirus genera. PI4P is also required for efficient polyprotein processing in enteroviruses, although this requirement is circumvented in PI4KB inhibitor escape mutants (20, 33, 34). Whether EMCV requires PI4P for polyprotein processing remains to be established.

ROs are believed to confer inherent advantages to the viruses that generate them, but it is unclear whether the different morphologies generated provide specific benefits. Although both single- and double-membrane ROs were found to support cardiovirus RNA synthesis, single-membrane structures predominated during the peak hours of genome replication. While this suggests that DMVs are largely superfluous for RNA synthesis, they may provide other benefits during infection. DMVs could selectively sequester viral products to prevent their detection by cellular innate immune sensors. In the case of enteroviruses, it has been suggested that DMVs may also be utilised for the non-lytic release of viral progeny (47). However, virions were only rarely detected within EMCV DMVs, which likely reflects random incorporation of virus particles and other cytosolic material when DMVs arise by enwrapping. Intriguingly, we found a large proportion of EMCV virions adjacent to ROs, suggesting close spatial coordination between RNA synthesis and capsid assembly. In enteroviruses, viral RNA synthesis and capsid assembly have been shown to be directly coupled, likely through interactions between the RNA replication machinery and the viral structural proteins (48, 49).

Collectively, our data reveal striking similarities between the ROs produced by enteroviruses and cardioviruses, and raise the possibility of a conserved mechanism of picornavirus RO biogenesis to form single-membrane structures that can transform into DMVs. In this regard picornaviruses appear to be unique, as other DMV-forming viruses, like coronaviruses or HCV, generate DMVs directly from the cellular donor membrane. Given that all +RNA viruses to date have been found to produce spherules or DMVs, viruses tend to be classified as producing one or the other RO type. However, while picornaviruses do produce DMVs, RNA synthesis transpires predominantly on the early single-membrane structures. Thus, in addition to the negative curvature spherules of alphaviruses and flaviviruses, and the DMVs formed by coronaviruses and hepaciviruses, positive curvature single membrane structures appear to represent a third major form of RO.

ACKNOWLEDGEMENTS

This work was supported by research grants from the Netherlands Organisation for Scientific Research (NWO-VENI-863.12.005 to HMvdS, NWO-VICI-91812628 to FJMvK, ERASysApp project 'SysVirDrug' ALW project number 832.14.003 to FJMvK and EJS, NWO-MEERVOUD 863.10.003 to MB), and from the European Union (7th Framework, EUVIRNA Marie Curie Initial Training Network,

grant agreement number 264286 to FJMvK and EJS). The funders had no role in study design, data collection and interpretation, or the decision to submit the work for publication.

EXPERIMENTAL PROCEDURES

Cell lines and reagents. HeLa R19 cells were maintained in Dulbecco's modified Eagle's medium (Gibco) supplemented with 10% fetal calf serum, penicillin, and streptomycin, and grown at 37°C in 5% CO2. The PI4KA inhibitor A1 (50) was kindly provided by T. Balla (National Institutes of Child Health and Human Development, National Institutes of Health, Bethesda, MD, USA) and used at a concentration of 10 nM.

Virus infections. Cells were inoculated for 1 hour with EMCV wt (strain Mengo) or EMCV 3A-A32V (described in (26)) at an MOI of 50, after which the inoculum was removed and fresh medium (with drug A1 where indicated) was added. At specified time-points after infection cells were prepared for qPCR, viral titer determination, immunofluorescence or electron microscopy.

Quantitative PCR. A Nucleospin RNA kit (Machery-Nagel) was used to isolate RNA from lysed cells. Random hexamer primers were used with a TaqMan reverse transcription reagents kit (Roche) to synthesize cDNA. Quantitative PCR was carried out using the LightCycler 480 SYBR Green I master kit (Roche) for 45 cycles (5 s at 95°C, 10 s at 60°C, and 20 s at 72°C) on a LightCycler 480 (Roche). Resulting Ct values were expressed as fold increase with the value at t = 2 h set as 1.

Viral titer determination. Total virus titers (of intra- and extra-cellular particles) were determined by freeze-thaw lysis of infected cells and endpoint titration.

Immunofluorescence microscopy. Cells were fixed with 3% paraformaldehyde and permeabilized with PBS containing 0.1% Triton X-100. Cells were then labelled with a mouse monoclonal antibody against dsRNA (J2 antibody; English and Scientific Consulting) and secondary Alexa Fluor 488-conjugated goat-anti-mouse IgG, alongside a nuclear stain (Hoechst 33342). Imaging was performed using a widefield DM5500 (Leica) fluorescent microscope.

Electron microscopy

Metabolic labelling and autoradiography. Infected cells were pre-incubated with 10 µg/ml dactinomycin for 1 hour to inhibit cellular transcription, then labelled for 45 minutes with tritiated uridine ([5-3H], 1 mCi/ml) (Perkin Elmer) also containing dactinomycin. Cells were then washed several times to remove unincorporated label and fixed for 1 hour in 1.5% glutaraldehyde in 0.1 M cacodylate buffer. Mock-infected control samples were similarly prepared. Post-fixation consisted of a 1-hour incubation with 1% osmium tetroxide in 0.1 M cacodylate buffer followed by a 1 hour incubation with 1% uranyl acetate solution. Samples were then washed and dehydrated in ethanol and infiltrated and embedded in LX 112 resin before polymerisation at 60°C. Sections of 50 nm were collected on formvar-coated EM grids and post stained with lead citrate and uranyl acetate, then carbon coated and prepared for autoradiography. For this, a thin layer of silver halide photographic emulsion (ILFORD L4) was applied in the dark to cell sections prepared for EM. Samples were incubated in the dark and developed after several weeks for autoradiography as described in (20). During incubation, the radiolabelled uridine incorporated during viral RNA synthesis decays, and the beta radiation emitted reduces the silver halide into atomic silver. These events manifest as

small, electron-dense grains dispersed around the original radioactive source that can be visualised during EM imaging.

High-pressure freezing and freeze substitution. Cells were high-pressure frozen using an EM PACT2 (Leica). Samples were maintained at -90°C in an AFS2 (Leica) freeze substitution device for 44 h in a solution of 20% H20, 2% osmium tetroxide and 1% anhydrous glutaraldehyde. A high water content was used as this was found to improve the contrast of RO membranes. The temperature was then raised to 0°C over a period of 22 h through a series of controlled warming phases (identical to those described in (21)). Samples were washed with acetone, infiltrated with epoxy resin LX-112 (Ladd Research) and polymerised at 60°C. Sections of 70 nm were collected on EM grids and post-stained with uranyl acetate and lead citrate. For tomography, thicker sections of 200 nm were collected. Before post-staining, both sides of the EM grid were incubated with 10 nm colloidal gold beads to serve as fiducial makers during tomogram reconstruction.

Electron microscopy imaging. Thin-section (50 or 70 nm) 2D images were collected (binning mode 2) on a Tecnai12 BioTWIN or TWIN electron microscope at 120 kV using an Eagle 4k slow-scan CCD camera (Thermo Fisher Scientific (formerly FEI)) or OneView 4k high frame-rate camera (Gatan) respectively. For the semi-automated collection of larger areas, meshes of overlapping images were acquired across the entire region of interest and later reconstituted into a single composite image (as described in (51)).

Electron tomography. Dual-axis tilt series of 200 nm sections each covering 130-140° around the region of interest were collected using an FEI F20 electron microscope at 200kV with zero-loss energy filtering using a 2k camera (Gatan) and 1.27 nm pixel size. Automated tilt series acquisition was performed using Xplore3DTM software (FEI). Tilt series alignment and tomogram reconstruction by weighted back-projection were carried out in IMOD (52) (version 4.7.15). In the process, the gold fiducial markers were digitally erased to be eliminated from the final 3D reconstruction. To determine the sizes of ROs spanning multiple sections, tilt series of the same region across 2-5 consecutive sections were collected and combined in IMOD to build tomogram volumes with a z-thickness of ~400-1000 nm. The sizes of ROs were estimated by measuring the SMTs, SMVs and DMVs within reconstructed volumes in IMOD. The maximum width of SMTs, SMVs and DMVs were considered the RO diameters. For all calculations SMTs were approximated to a cylinder, and the inner DMV membrane surface area was considered an approximation of the outer.

To generate models of features of interest, image segmentations were made from tomograms using Amira 6.0.1 (FEI). Before segmentation, tomograms were post-processed to enhance edges by nonlinear anisotropic diffusion filtering (53) as implemented in IMOD using 5 iterations and K=1000, and then binned by 2 in x and y. Membranes were selected in manually masked areas by thresholding, then refined by removing islands and smoothing. Surfaces that were poorly represented (e.g. top and bottom surfaces of vesicles and tubules) due to the missing-wedge effect were manually repaired.

REFERENCES

1. Carocci M, Bakkali-Kassimi L. 2012. The encephalomyocarditis virus. Virulence 3:351-67.
2. Koenen F, Vanderhallen H, Castryck F, Miry C. 1999. Epidemiologic, pathogenic and molecular analysis of recent encephalomyocarditis outbreaks in Belgium. Zentralbl Veterinarmed B 46:217-31.
3. Gazda LS, Collins J, Lovatt A, Holdcraft RW, Morin MJ, Galbraith D, Graham M, Laramore MA, Maclean C, Black J, Milne EW, Marthaler DG, Vinerean HV, Michalak MM, Hoffer D, Richter S, Hall RD, Smith BH. 2016. A comprehensive microbiological safety approach for agarose encapsulated porcine islets intended for clinical trials. Xenotransplantation 23:444-463.
4. Brewer LA, Lwamba HC, Murtaugh MP, Palmenberg AC, Brown C, Njenga MK. 2001. Porcine encephalomyocarditis virus persists in pig myocardium and infects human myocardial cells. J Virol 75:11621-9.
5. Mecha M, Carrillo-Salinas FJ, Mestre L, Feliu A, Guaza C. 2013. Viral models of multiple sclerosis: Neurodegeneration and demyelination in mice infected with Theiler's virus. Progress in Neurobiology 101:46-64.
6. Jones MS, Lukashov VV, Ganac RD, Schnurr DP. 2007. Discovery of a novel human picornavirus in a stool sample from a pediatric patient presenting with fever of unknown origin. J Clin Microbiol 45:2144-50.
7. Ren LL, Gonzalez R, Xie ZD, Xiao Y, Li YJ, Liu CY, Chen L, Yang QQ, Vernet G, Paranhos-Baccala G, Jin Q, Shen KL, Wang JW. 2010. Saffold Cardioviruses of 3 Lineages in Children with Respiratory Tract Infections, Beijing, China. Emerging Infectious Diseases 16:1158-1161.
8. Chiu CY, Greninger AL, Kanada K, Kwok T, Fischer KF, Runckel C, Louie JK, Glaser CA, Yagi S, Schnurr DP, Haggerty TD, Parsonnet J, Ganem D, DeRisi JL. 2008. Identification of cardioviruses related to Theiler's murine encephalomyelitis virus in human infections. Proceedings of the National Academy of Sciences of the United States of America 105:14124-14129.
9. Tan SZ, Tan MZ, Prabakaran M. 2017. Saffold virus, an emerging human cardiovirus. Rev Med Virol 27.
10. Benschop KS, van der Avoort HG, Duizer E, Koopmans MP. 2015. Antivirals against enteroviruses: a critical review from a public-health perspective. Antivir Ther 20:121-30.
11. De Palma AM, Vliegen I, De Clercq E, Neyts J. 2008. Selective inhibitors of picornavirus replication. Med Res Rev 28:823-84.
12. Rotbart HA. 2002. Treatment of picornavirus infections. Antiviral Res 53:83-98.
13. Thibaut HJ, De Palma AM, Neyts J. 2012. Combating enterovirus replication: state-of-the-art on antiviral research. Biochem Pharmacol 83:185-92.
14. Clayton EL, Minogue S, Waugh MG. 2013. Mammalian phosphatidylinositol 4-kinases as modulators of membrane trafficking and lipid signaling networks. Progress in Lipid Research 52:294-304.
15. Balla A, Balla T. 2006. Phosphatidylinositol 4-kinases: old enzymes with emerging functions.

Trends in Cell Biology 16:351-361.
16. Hsu NY, Ilnytska O, Belov G, Santiana M, Chen YH, Takvorian PM, Pau C, van der Schaar H, Kaushik-Basu N, Balla T, Cameron CE, Ehrenfeld E, van Kuppeveld FJ, Altan-Bonnet N. 2010. Viral reorganization of the secretory pathway generates distinct organelles for RNA replication. Cell 141:799-811.
17. van der Schaar HM, van der Linden L, Lanke KH, Strating JR, Purstinger G, de Vries E, de Haan CA, Neyts J, van Kuppeveld FJ. 2012. Coxsackievirus mutants that can bypass host factor PI4KIIIbeta and the need for high levels of PI4P lipids for replication. Cell Res 22:1576-92.
18. Dorobantu CM, Albulescu L, Harak C, Feng Q, van Kampen M, Strating JR, Gorbalenya AE, Lohmann V, van der Schaar HM, van Kuppeveld FJ. 2015. Modulation of the Host Lipid Landscape to Promote RNA Virus Replication: The Picornavirus Encephalomyocarditis Virus Converges on the Pathway Used by Hepatitis C Virus. PLoS Pathog 11:e1005185.
19. Reiss S, Rebhan I, Backes P, Romero-Brey I, Erfle H, Matula P, Kaderali L, Poenisch M, Blankenburg H, Hiet MS, Longerich T, Diehl S, Ramirez F, Balla T, Rohr K, Kaul A, Buhler S, Pepperkok R, Lengauer T, Albrecht M, Eils R, Schirmacher P, Lohmann V, Bartenschlager R. 2011. Recruitment and activation of a lipid kinase by hepatitis C virus NS5A is essential for integrity of the membranous replication compartment. Cell Host Microbe 9:32-45.
20. Melia CE, van der Schaar HM, Lyoo H, Limpens R, Feng Q, Wahedi M, Overheul GJ, van Rij RP, Snijder EJ, Koster AJ, Barcena M, van Kuppeveld FJM. 2017. Escaping Host Factor PI4KB Inhibition: Enterovirus Genomic RNA Replication in the Absence of Replication Organelles. Cell Rep 21:587-599.
21. Limpens RW, van der Schaar HM, Kumar D, Koster AJ, Snijder EJ, van Kuppeveld FJ, Barcena M. 2011. The transformation of enterovirus replication structures: a three-dimensional study of single- and double-membrane compartments. MBio 2(5):e00166-11.
22. Belov GA, Nair V, Hansen BT, Hoyt FH, Fischer ER, Ehrenfeld E. 2012. Complex dynamic development of poliovirus membranous replication complexes. J Virol 86:302-12.
23. Dales S, Franklin RM. 1962. A comparison of the changes in fine structure of L cells during single cycles of viral multiplication, following their infection with the viruses of Mengo and encephalomyocarditis. J Cell Biol 14:281-302.
24. Amako K, Dales S. 1967. Cytopathology of Mengovirus infection. II. Proliferation of membranous cisternae. Virology 32:201-15.
25. Friedmann A, Lipton HL. 1980. Replication of Theiler's murine encephalomyelitis viruses in BHK21 cells: an electron microscopic study. Virology 101:389-98.
26. Dorobantu CM, Albulescu L, Lyoo H, van Kampen M, De Francesco R, Lohmann V, Harak C, van der Schaar HM, Strating JR, Gorbalenya AE, van Kuppeveld FJ. 2016. Mutations in Encephalomyocarditis Virus 3A Protein Uncouple the Dependency of Genome Replication on Host Factors Phosphatidylinositol 4-Kinase IIIalpha and Oxysterol-Binding Protein. mSphere 1.
27. Knoops K, Barcena M, Limpens RWAL, Koster AJ, Mommaas AM, Snijder EJ. 2012. Ultrastructural Characterization of Arterivirus Replication Structures: Reshaping the Endoplasmic Reticulum To Accommodate Viral RNA Synthesis. Journal of Virology 86:2474-2487.

28. Knoops K, Kikkert M, van den Worm SHE, Zevenhoven-Dobbe JC, van der Meer Y, Koster AJ, Mommaas AM, Snijder EJ. 2008. SARS-coronavirus replication is supported by a reticulovesicular network of modified endoplasmic reticulum. Plos Biology 6:1957-1974.
29. Maier HJ, Hawes PC, Cottam EM, Mantell J, Verkade P, Monaghan P, Wileman T, Britton P. 2013. Infectious bronchitis virus generates spherules from zippered endoplasmic reticulum membranes. MBio 4:e00801-13.
30. Romero-Brey I, Merz A, Chiramel A, Lee JY, Chlanda P, Haselman U, Santarella-Mellwig R, Habermann A, Hoppe S, Kallis S, Walther P, Antony C, Krijnse-Locker J, Bartenschlager R. 2012. Three-dimensional architecture and biogenesis of membrane structures associated with hepatitis C virus replication. PLoS Pathog 8:e1003056.
31. Bienz KA. 1977. Techniques and applications of autoradiography in the light and electron microscope. Microsc Acta 79:1-22.
32. Ginsel LA, Onderwater JJ, Daems WT. 1979. Resolution of a gold latensification-elon ascorbic acid developer for Ilford L4 emulsion. Histochemistry 61:343-6.
33. Arita M. 2016. Mechanism of Poliovirus Resistance to Host Phosphatidylinositol-4 Kinase III beta Inhibitor. ACS Infect Dis 2:140-8.
34. Ford Siltz LA, Viktorova EG, Zhang B, Kouiavskaia D, Dragunsky E, Chumakov K, Isaacs L, Belov GA. 2014. New small-molecule inhibitors effectively blocking picornavirus replication. J Virol 88:11091-107.
35. Lyoo H, Dorobantu CM, van der Schaar HM, van Kuppeveld FJM. 2017. Modulation of proteolytic polyprotein processing by coxsackievirus mutants resistant to inhibitors targeting phosphatidylinositol-4-kinase IIIbeta or oxysterol binding protein. Antiviral Res 147:86-90.
36. Wang J, Du J, Jin Q. 2014. Class I ADP-ribosylation factors are involved in enterovirus 71 replication. PLoS One 9:e99768.
37. Bienz K, Egger D, Pasamontes L. 1987. Association of Polioviral Proteins of the P2-Genomic Region with the Viral Replication Complex and Virus-Induced Membrane Synthesis as Visualized by Electron-Microscopic Immunocytochemistry and Autoradiography. Virology 160:220-226.
38. Takeda N, Kuhn RJ, Yang CF, Takegami T, Wimmer E. 1986. Initiation of poliovirus plus-strand RNA synthesis in a membrane complex of infected HeLa cells. J Virol 60:43-53.
39. Monaghan P, Cook H, Jackson T, Ryan M, Wileman T. 2004. The ultrastructure of the developing replication site in foot-and-mouth disease virus-infected BHK-38 cells. J Gen Virol 85:933-46.
40. van der Hoeven B, Oudshoorn D, Koster AJ, Snijder EJ, Kikkert M, Barcena M. 2016. Biogenesis and architecture of arterivirus replication organelles. Virus Res 220:70-90.
41. Oudshoorn D, Rijs K, Limpens RWAL, Groen K, Koster AJ, Snijder EJ, Kikkert M, Bárcena M. 2017. Expression and Cleavage of Middle East Respiratory Syndrome Coronavirus nsp3-4 Polyprotein Induce the Formation of Double-Membrane Vesicles That Mimic Those Associated with Coronaviral RNA Replication. mBio DOI:10.1128/mBio.01658-17.
42. Jackson WT, Giddings TH, Jr., Taylor MP, Mulinyawe S, Rabinovitch M, Kopito RR, Kirkegaard K. 2005. Subversion of cellular autophagosomal machinery by RNA viruses. PLoS Biol 3:e156.
43. Richards AL, Soares-Martins JAP, Riddell GT, Jackson WT. 2014. Generation of Unique

Poliovirus RNA Replication Organelles. mBio 5.
44. Carlsson SR, Simonsen A. 2015. Membrane dynamics in autophagosome biogenesis. J Cell Sci 128:193-205.
45. Roulin PS, Lotzerich M, Torta F, Tanner LB, van Kuppeveld FJ, Wenk MR, Greber UF. 2014. Rhinovirus uses a phosphatidylinositol 4-phosphate/cholesterol counter-current for the formation of replication compartments at the ER-Golgi interface. Cell Host Microbe 16:677-90.
46. Berger KL, Kelly SM, Jordan TX, Tartell MA, Randall G. 2011. Hepatitis C virus stimulates the phosphatidylinositol 4-kinase III alpha-dependent phosphatidylinositol 4-phosphate production that is essential for its replication. J Virol 85:8870-83.
47. Chen YH, Du W, Hagemeijer MC, Takvorian PM, Pau C, Cali A, Brantner CA, Stempinski ES, Connelly PS, Ma HC, Jiang P, Wimmer E, Altan-Bonnet G, Altan-Bonnet N. 2015. Phosphatidylserine vesicles enable efficient en bloc transmission of enteroviruses. Cell 160:619-30.
48. Nugent CI, Johnson KL, Sarnow P, Kirkegaard K. 1999. Functional coupling between replication and packaging of poliovirus replicon RNA. Journal of Virology 73:427-435.
49. Liu Y, Wang CL, Mueller S, Paul AV, Wimmer E, Jiang P. 2010. Direct Interaction between Two Viral Proteins, the Nonstructural Protein 2C(ATPase) and the Capsid Protein VP3, Is Required for Enterovirus Morphogenesis. Plos Pathogens 6.
50. Bojjireddy N, Botyanszki J, Hammond G, Creech D, Peterson R, Kemp DC, Snead M, Brown R, Morrison A, Wilson S, Harrison S, Moore C, Balla T. 2014. Pharmacological and genetic targeting of the PI4KA enzyme reveals its important role in maintaining plasma membrane phosphatidylinositol 4-phosphate and phosphatidylinositol 4,5-bisphosphate levels. J Biol Chem 289:6120-32.
51. Faas FG, Avramut MC, van den Berg BM, Mommaas AM, Koster AJ, Ravelli RB. 2012. Virtual nanoscopy: generation of ultra-large high resolution electron microscopy maps. J Cell Biol 198:457-69.
52. Kremer JR, Mastronarde DN, McIntosh JR. 1996. Computer visualization of three-dimensional image data using IMOD. Journal of Structural Biology 116:71-76.
53. Frangakis AS, Hegerl R. 2001. Noise reduction in electron tomographic reconstructions using nonlinear anisotropic diffusion. Journal of Structural Biology 135:239-250.

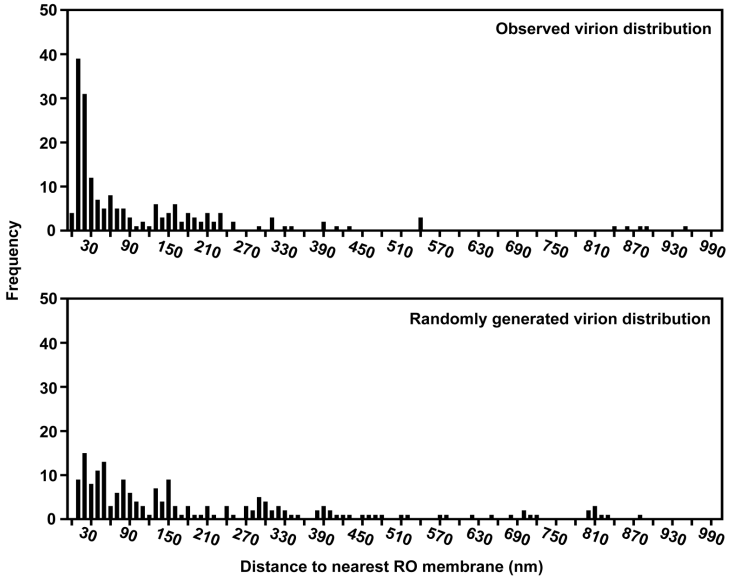


Figure S1. Analysis of the distribution of virus particles shows an association between EMCV virions and ROs. Distribution of EMCV virions relative to nearest RO membrane in HeLa cells infected with EMCV at 7 hpi (pooled data from two tomograms from two different cells). The distances from the centre of virions to the nearest SMV, SMT or DMV RO membrane was measured (n = 183, represented in upper graph). To independently assess whether this measured distribution of particles relative to ROs differed from a random distribution, tomograms were populated with models of simulated particles by randomly generating co-ordinates within the cytosolic space of the tomogram volume. The distances between the centres of these randomly-generated particles and the nearest RO membrane was then measured (n = 183, represented in lower graph). The cumulative frequency distributions of the observed and generated data were found to be significantly different (Kolmogorov–Smirnov, p = <000.1).

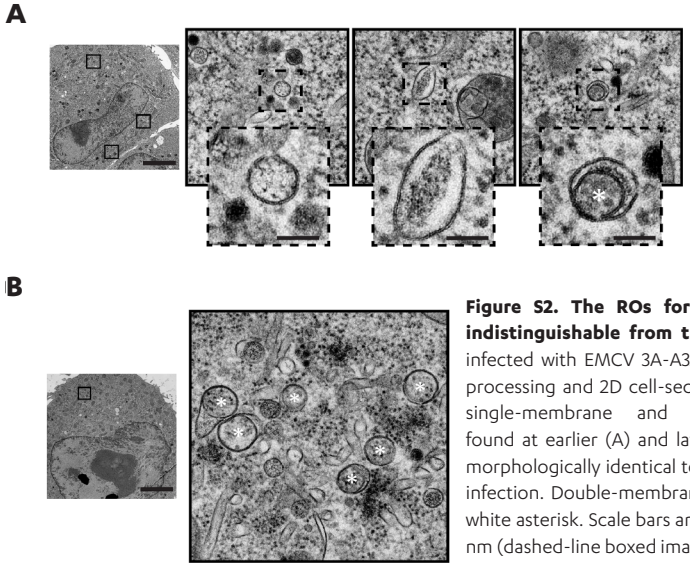


Figure S2. The ROs formed by EMCV 3A-A32V are indistinguishable from those of wt EMCV. HeLa cells infected with EMCV 3A-A32V were frozen at 5 hpi for EM processing and 2D cell-section analysis. The virus-induced single-membrane and double-membrane structures found at earlier (A) and later (B) stages of infection were morphologically identical to those formed during wt EMCV infection. Double-membrane structures are marked with a white asterisk. Scale bars are 5 µm (unboxed images) or 100 nm (dashed-line boxed images).

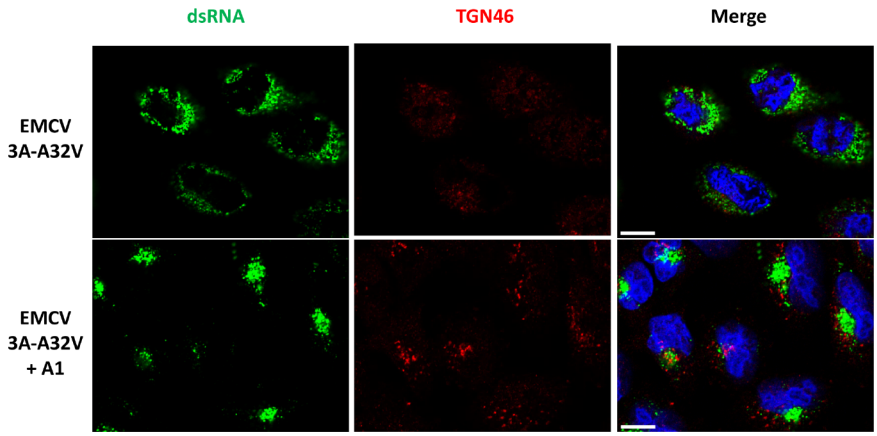


Figure S3. EMCV 3A-A32V dsRNA signal clusters in the perinuclear Golgi region under PI4KA inhibition. HeLa cells were infected with EMCV 3A-A32V at an MOI of 75 with or without 10 nM A1 treatment to inhibit PI4KA, and fixed at 7. The trans-Golgi network marker TGN46 was labelled with a primary rabbit polyclonal antibody (Novus Biologicals) and secondary Alexa Fluor 594-conjugated goat-anti-rabbit IgG for immunofluorescence analysis in a Leica SPII confocal microscope. PI4KA inhibition led to clustering of dsRNA signal (green) around the perinuclear region in foci that were often proximal to the TGN46 signal (red). Scale bar is 10 µm.

Movie S1. Reconstructed and joined serial tomograms and segmentation of ROs found at early stages of EMCV infection. The complete tomogram volume (1 µm x 2.4 µm x 2.4 µm) of the region featured in Fig.3A is shown, which represents a typical region in an infected cell at 5 hpi. Segmentation of a sub-volume within this data highlights connections between SMTs (blue) or SMVs (red) and the endoplasmic reticulum (green).

Movie S2. Reconstructed and joined serial tomograms and segmentation of ROs found at late stages of EMCV infection. The complete tomogram volume (0.4 µm x 2.3 µm x 2.3 µm) of the region featured in Fig. 4A is shown, which represents a typical region in an infected cell at 7 hpi. Segmentation of a sub-volume within this data highlights clusters of DMVs (yellow) and SMTs (blue).

CHAPTER 6

GENERAL DISCUSSION

Charlotte E. Melia[1,2]

[1] Department of Cell and Chemical biology, Section Electron Microscopy, Leiden University Medical Center, 2300 RC Leiden, The Netherlands.

[2] Sir William Dunn School of Pathology, University of Oxford, Oxford, OX1 3RE, United Kingdom.

THE MULTIFACETED ROLE OF PI4P IN PICORNAVIRUS INFECTION

As obligate intracellular parasites, viruses are dependent on the cells they infect for their propagation. In addition to hijacking cellular systems like endocytosis for virus entry and the ribosomal machinery for translation, individual host factors are utilised to support different processes throughout the virus life cycle.

In uninfected cells PI4P is a lipid with diverse functions, including the mediation of cholesterol exchange at the ER-Golgi interface via OSBP. Many of the viruses that utilise PI4P, including enteroviruses and cardioviruses, recruit PI4Ks to sites of replication to increase local PI4P levels (1-4), where it facilitates local cholesterol exchange (2, 5-8). A role for PI4P in modulating proteolytic processing of the viral polyprotein has also emerged from experiments in poliovirus (9, 10), where PI4P appears to mediate cleavage at the 3AB junction. In **Chapter 3**, we establish that this role is conserved in another enterovirus, CVB3. The mechanism underlying this effect in either enterovirus species has yet to be determined, but may relate to the influence of lipid composition on the orientation of 3A precursors within the membrane. Indeed, PI4KB resistant mutations in both poliovirus (3A-A70T) and CVB3 (3A-H57Y) lie within or proximal to the putative membrane-spanning hydrophobic domain of the 3A protein (11, 12). Interestingly, OSBP inhibition also impairs 3A-3B cleavage (10), suggesting that this effect could be mediated by low membrane cholesterol levels rather than low PI4P levels directly. In **Chapter 3** we also outline a new function of PI4KB. Utilising a CVB3 resistant to PI4KB inhibition, low local concentrations of PI4P were found to delay the formation of CVB3 ROs to beyond the phase of exponential viral RNA synthesis. ROs that appear to be morphologically typical formed only late in infection under PI4KB inhibition, and these structures appeared to be devoid of the high levels of PI4P associated with ROs in wt CVB3 infection. Thus, high PI4P levels are not strictly required for the development of ROs, but do expedite their formation. Inefficient cleavage of viral proteins has been suggested to affect RO formation in HCV (13), as well as in coronaviruses (14). However, poor polyprotein processing under low-PI4P conditions did not explain the delay in CVB3 RO formation we observed, as polyprotein processing of the PI4KB resistant CVB3 3A-H57Y was not impaired under PI4KB inhibition. This suggests that the role of PI4P in polyprotein processing and its role in expediting RO formation are independent in enterovirus-infected cells.

While the mechanism that underlies the role of PI4P in RO formation remains uncertain, it is likely to be more nuanced than for other host factors that influence RO development, like the ESCRT proteins and reticulons that shape virus-induced membrane modifications during infections of other +RNA viruses (15, 16), and perhaps also of enteroviruses (17). PI4P may in fact have a semi-redundant function during RO formation, rather than an intrinsic structural role. This is supported by findings in **Chapter 5**, in which an analogous PI4KA-resistant cardiovirus, EMCV 3A-A32V, was found to produce ROs under PI4KA inhibition at a similar time point post-infection to uninhibited wild-type virus. One tantalising possibility is that the effect of PI4P on RO formation stems from its role in OSBP-mediated cholesterol recruitment, as cholesterol has a direct effect on the formation of lipid domains and on membrane morphology (18-20). Indeed, enteroviruses have been shown to utilise other routes for cholesterol recruitment, for instance via endosomal transfer (21). These alternative routes may be more effectively harnessed, when PI4P levels are suppressed. However, while cholesterol is essential for replication and, like PI4P, has been shown to be important for polyprotein processing (21, 22), a role for cholesterol in RO formation has yet to be directly demonstrated.

MEMBRANE UTILISATION FOR RO FORMATION IS REMARKABLY FLEXIBLE

While our understanding of the viral and host components that engender enterovirus ROs is broadening, fundamental questions about their origin remain unanswered. Putative donor organelles have been identified for many +RNA viruses using electron microscopy, but connections between a donor organelle and ROs have been elusive in ultrastructural studies of enterovirus infection. Other studies that explore co-localisations between viral and host factors, or hunt for the locations of early viral RNA synthesis, have generated a sprawling and at times contradictory picture of where the first enterovirus ROs are formed. Much of the available evidence suggests that membranes of the Golgi apparatus contribute to enterovirus RO biogenesis (1, 23-25). This idea is supported by the chronological correspondence between Golgi apparatus disintegration and RO formation observed in EM (26), and in live-cell imaging data (**Chapter 2**) of infected cells, and by the association of viral replication with the Golgi in the absence of ROs found in **Chapter 3**. However, alternative origins have also been suggested, including the ER and the autophagy pathway (1, 23, 27-29). Interpretation of data that suggest potentially conflicting origins is confounded by the differences in virus species, the times post-infection assessed, and the experimental methodologies used across these studies. In **Chapter 4** we present compelling evidence that membrane utilisation by enteroviruses is diverse, revealing connections between ROs and both ER and Golgi membranes in SBF-SEM and TEM data. In addition to uniting disparate ideas about the origins of enterovirus ROs, these data highlight the surprising flexibility with which viruses can exploit cellular membranes for RO formation. This flexibility may extend to other +RNA viruses, as suggested by key experiments using tombusviruses and nodaviruses, where RO formation could be directed to specific organelles using localisation signals, or was found to occur at alternative organelles in the absence of the typical membrane target (30, 31).

Our observations further demonstrate that morphologically similar ROs can be derived from different membrane sources. This suggests that the host factors that drive or contribute to enterovirus RO biogenesis, and those that have a role in the transformation of single- into double-membrane structures, are not specific to the membrane origin, or can be recruited. These criteria are well met by PI4P, which is ubiquitous in the cell and produced by kinases that are readily recruited to specific cellular compartments. In uninfected cells PI4KB is recruited primarily to the Golgi apparatus, while PI4KA is responsible for PI4P generation at the plasma membrane and ER (32, 33). While PI4KB recruitment to the Golgi apparatus is enhanced during enterovirus infection, where it contributes to rapid RO formation (**Chapter 3**), the role of PI4P in ER-derived RO formation is less clear. PI4P production may be stimulated by the selective recruitment of PI4KB to the ER, else existing ER pools of PI4P generated by PI4KA may be sufficient (e.g. at ER exit sites (34)). Another possibility is that ROs of ER origin form independently of PI4P. Live-cell imaging data (Chapter 3) suggest that, under PI4KB inhibition, the 3A protein accumulates almost exclusively in the Golgi region rather than first forming in peripheral/ER-associated clusters, pointing to a role for PI4KB in ER-derived RO formation.

In **Chapter 5** this idea that characteristic picornavirus RO morphologies are not tied to a specific membrane origin was reinforced following the characterisation of the 3D morphology and development of EMCV ROs. Despite significant differences in cardiovirus and enterovirus host factor utilisation during replication, EMCV was found to produce ROs that bore a striking resemblance to

those of enteroviruses, producing initially single-membrane structures that developed into DMVs. Connections between endomembranes and early ROs were readily found during EMCV infection, suggesting that the ER is the exclusive donor organelle for cardiovirus ROs. Together with the results in **Chapter 4**, these data suggest that the donor organelle is not deterministic of the resulting RO morphology for enteroviruses and cardioviruses, and perhaps picornaviruses more generally. While studies in tombusviruses (35, 36) provide evidence that the viral replication machinery can be successfully diverted to different organelles, it is unclear whether virus-induced membrane rearrangements form at these sites and, if so, whether these structures have typical morphologies.
While viruses appear to target specific membrane compartments upon infection, these findings altogether raise the question of what defines an appropriate membrane platform for replication, or an appropriate membrane donor for RO formation. While viruses have typical membrane targets from which they derive ROs for genome replication, it is clear that the core requirements for replication are not tied to specific membrane compartments in all cases. Membrane utilisation may instead be decided by the localisation and dynamics of early replication events, the requirements for protein folding and processing, or be the result of favourable positioning or proximity to auxiliary organelles utilised during but not essential for replication, like lipid droplets or endosomes.

THE SITES OF RNA SYNTHESIS REPRESENT A NEW RO PHENOTYPE

The archetypal RO morphologies produced by +RNA viruses are broadly characterised as forming secluded compartments; the spherules of FHV (37), Zika virus (38), and DENV (39, 40) and the DMVs of SARS- and MERS- coronaviruses (41, 42), EAV (43), HCV (44), CVB3 (26), PV (25) and EMCV (**Chapter 5**). However, our findings from studies of EMCV (**Chapter 5**) and similar data from enterovirus studies ((25, 26), **Chapter 3**) suggest that, for the picornaviruses, the primary sites of RNA synthesis are single-membrane ROs with positive curvature. While the 3D structures of other picornavirus ROs remain to be explored, the 2D profiles found in EM cell-sections of other genera, like the aphthoviruses, also resemble those of the enteroviruses and cardioviruses (45). While putative DMVs identified in FMDV-infected cells could be found at the mid-point of infection, the predominant ROs at early and intermediate points in infection were single-membrane structures. Rather than the DMVs then, it is single-membrane structures that appear to be the primary support for picornavirus RNA synthesis. For this reason, single-membrane structures with positive curvature must be considered a third archetypal RO morphology produced by +RNA viruses. Unlike the spherules and DMVs utilised for genome replication in other +RNA virus families, these single-membrane tubule ROs of picornaviruses do not enclose cytosolic space.

THE ADVANTAGES OF GENERATING ROS FOR PICORNAVIRUS INFECTION

In **Chapter 3** we present an example of +RNA virus replication at a morphologically intact cellular organelle. These data effectively demonstrate that ROs are not strictly required for sustained enterovirus RNA synthesis, raising questions over the advantages of RO formation during replication. While a causative relationship between the delayed enterovirus RO formation and reduced replicative efficiency observed under PI4KB inhibition has not been established, this observation aligns with one of the prevailing hypotheses regarding the role of ROs; that they contribute to

effective RNA synthesis. The advantages conferred by RO formation in this regard may include the expansion of suitable membranes for genome replication, or the provision of an optimal environment for the RNA replication machinery to assemble and function. For FHV (46), poliovirus (47) and SARS-coronavirus (48) there is evidence to suggest that intact membranes are required for efficient viral RNA synthesis, supporting this notion.

Intact membranes may also prove beneficial by protecting viral RNA from sensors of the innate immune system. In vitro studies of FHV (46), and poliovirus (49) show a link between (intact) RO membranes and RNAse access to RO-associated viral RNA. Given that enterovirus replication complexes are thought to reside on the cytosolic face of ROs (28), this apparent protective function could serve to shield viral replication intermediates from cellular innate immune sensors in vivo. Another +RNA virus, HCV, appears to have developed an alternative or additional mechanism to shield viral RNA species from cellular sensors, by integrating nucleoporins into its membranous web to regulate protein access (50). It should be noted that, while these studies show that intact membranes confer protection, it remains unknown whether this effect is dependent upon specific ROs morphologies. For spherule-forming viruses, the morphology of ROs may provide a straightforward shielding mechanism. Given that only a small, neck-like opening bridges the space between cytosol and spherule interior, these compartments are relatively isolated from the remainder of the cytosol, limiting the availability of viral products for detection by cellular sensors. Unlike spherules, the tubules and vesicles produced by picornaviruses, and (if their outer membrane is utilised for genome replication) the DMVs generated by nidoviruses and flaviviruses replication, represent a large, exposed surface area vulnerable to sensing. For these viruses, the concept that the morphology of their ROs is adapted to shield RNA is less intuitive. In fact, an absence of ROs at the peak of RNA synthesis in CVB3 3A-H57Y infection was found to have no significant impact on the measured IFN-b response across infection, or the state of the innate immune sensors MAVS and PKR, as described in **Chapter 3**. While it remains to be established whether viral RNA is also physically shielded (e.g. from RNases) in these conditions, these data could suggest that any protective function is unrelated to RO morphology, and that replication at a morphologically intact Golgi apparatus is similarly protective to replication at ROs. Protection could feasibly be conferred by the viral replication machinery within the replication membrane. Viral dsRNA must be available to the C terminus and helicase domain of the RIG-I-like receptor MDA5 for its activation (51), and the juxtaposition of membrane and replicating RNA, or the viral machinery surrounding it, may limit accessibility. It may also be that membranes, morphology-dependent or otherwise, serve at best a semi-redundant function in innate immune evasion, given the efficacy of viral proteases that cleave innate immunity recognition and signalling molecules (52, 53).

ROs may also facilitate other processes during infection, by co-ordinating different events during the viral life cycle. For enteroviruses, genome replication at ROs is directly coupled to genome encapsidation (54, 55). This mechanism may have developed as a means of increasing the efficacy of nascent virion production by eliminating the need for RNA diffusion ahead of packaging. If RO membranes represent a protective environment for viral products, then diffusion of ssRNA away from ROs would also expose the virus to cellular innate immune proteins like RNAse L (56) in viruses like CVB3 whose genomes are vulnerable to its endonuclease activity (57). The direct coupling of viral genome synthesis and encapsidation also ensures specificity of RNA packaging, and represents part of the 'higher order proof-reading' mechanism inherent in the successful translation,

replication and packaging of viral genome (58). That these processes are coupled implies that virus particles also assemble at ROs, and may in some way utilise the membrane platform they provide to co-ordinate assembly. Alternatively, particles may assemble in the cytosol and aggregate at ROs. In accordance with these possibilities, a striking spatial proximity between ROs and virus particles was observed in EMCV-infected cells in **Chapter 5**, which could reflect a similar association between RNA synthesis and virion packaging in cardioviruses.

THE ROLE OF DMVS IN PICORNAVIRUS REPLICATION

Enteroviruses DMVs have also been reported to serve as vehicles for the en bloc transfer of mature virions (59-61), which may increase the likelihood of a viable infection if complementary viral quasispecies are exported together. However, the analysis of EMCV virion distribution in **Chapter 5** demonstrated that only a small fraction of DMVs contain virus particles. While this does not exclude the possibility that these DMVs are exported, it suggests that en bloc transfer is not a prominent mechanism of viral export in cardioviruses.

A clear role for DMVs in picornavirus replication has yet to be identified. The peak of viral RNA synthesis in enteroviruses and cardioviruses (**Chapters 4** and **5**) occurs when single-membrane structures predominate, ahead of their transformation into DMVs, raising the question of why this transformation occurs. One possibility is that DMV formation, by enwrapping small volumes of cytosol, is a mechanism to shield a proportion of the RNA replication machinery or replicative products from innate immune sensors. This could be advantageous particularly at late stages of infection, when other viral mechanisms to evade the cellular innate immune system, like the viral protease-mediated cleavage of cellular sensors, may be overburdened. Evidence for the accumulation of viral RNA within DMVs has been found in nidoviruses (41, 43), although it remains unclear whether the inner membrane of nidovirus DMVs, which do not have openings connecting the DMV interior to the cytosol, are the primary site of nidovirus RNA synthesis. A small proportion of enterovirus and cardiovirus DMVs were found in a vase-like configuration that connected the DMV interior and the cytosol ((26), **Chapter 5**). It is unclear whether these openings represent (semi-) stable structures found in a low percentage of DMVs, or a transient late stage of DMV formation. Given that picornavirus RNA synthesis continues following the transformation of tubules into DMVs, open DMVs could represent a shielded environment for late-stage viral genome replication. Indeed, given the evidence for coupled genome replication and virion packaging, those DMVs that contain openings may correspond to those that accumulate nascent virions, perhaps ahead of pore fusion and en bloc transfer.

RETHINKING THE VIRAL REPLICATION MEMBRANE

While categorisations based on morphology are contextually useful, archetypal RO morphologies are an incomplete picture of how viral replication membranes develop throughout infection. Indeed, prior to the accumulation of RO-forming viral proteins, viral genome replication may occur at largely unmodified membranes.

It is also significant that, while the vast majority of viral RNA synthesis occurs at ROs under typical infection conditions, imposing specific modifications or conditions can produce exceptions to this.

In **Chapter 3,** extended enterovirus RNA synthesis was shown to occur at a morphologically intact Golgi apparatus under low PI4P conditions, without any apparent penalty to innate immune evasion, but with a corresponding drop in RNA replication efficiency. In this case it is unclear whether low replication efficiency results directly from a lack of archetypal enterovirus ROs, or indirectly from (the incomplete rescue of) defects in polyprotein processing. Other evidence suggests that RO morphology can be dispensed without a cost to fitness. Manipulating the relative levels of the BMV 1a and 2a polymerase shifted the BMV replication membrane morphology from archetypal spherules to flat membrane sheets, without a reduction to replicative efficiency (62). This highlights again the surprising flexibility with which viruses can use membranes, and emphasises the pitfalls of defining the membranes utilised for replication by their morphology. Indeed, the evidence thus far aligns with a scenario where specific membrane morphologies may be secondary for viral RNA synthesis. A holistic approach is required to understand the membrane composition that underlies the efficient, sustained viral RNA synthesis that is typically associated with ROs. Improved procedures for the isolation and lipidomic or proteomic analysis of replication membrane fractions will allow for a more comprehensive understanding of the changing compositions of replication membranes at different stages of infection. This information can be coupled with powerful techniques to visualise native-state RO structures by cryo-electron microscopy, which can inform us regarding the conformation of intact replication complexes, and demonstrate how these assemble and function on the surface of replication membranes with changing compositions. The mechanism that drives the development of archetypal RO morphologies may well emerge from this enhanced understanding of their composition. It is this mechanism that lies at the heart of the question of RO function, and whether the morphologies that arise during infection represent the result of, or a prerequisite to, effective replication.

REFERENCES

1. Hsu NY, Ilnytska O, Belov G, Santiana M, Chen YH, Takvorian PM, Pau C, van der Schaar H, Kaushik-Basu N, Balla T, Cameron CE, Ehrenfeld E, van Kuppeveld FJM, Altan-Bonnet N. 2010. Viral Reorganization of the Secretory Pathway Generates Distinct Organelles for RNA Replication. Cell 141:799-811.
2. Dorobantu CM, Albulescu L, Harak C, Feng Q, van Kampen M, Strating JRPM, Gorbalenya AE, Lohmann V, van der Schaar HM, van Kuppeveld FJM. 2015. Modulation of the Host Lipid Landscape to Promote RNA Virus Replication: The Picornavirus Encephalomyocarditis Virus Converges on the Pathway Used by Hepatitis C Virus. Plos Pathogens 11.
3. Sasaki J, Ishikawa K, Arita M, Taniguchi K. 2012. ACBD3-mediated recruitment of PI4KB to picornavirus RNA replication sites. EMBO J 31:754-66.
4. Reiss S, Rebhan I, Backes P, Romero-Brey I, Erfle H, Matula P, Kaderali L, Poenisch M, Blankenburg H, Hiet MS, Longerich T, Diehl S, Ramirez F, Balla T, Rohr K, Kaul A, Buhler S, Pepperkok R, Lengauer T, Albrecht M, Eils R, Schirmacher P, Lohmann V, Bartenschlager R. 2011. Recruitment and activation of a lipid kinase by hepatitis C virus NS5A is essential for integrity of the membranous replication compartment. Cell Host Microbe 9:32-45.

5. Arita M, Kojima H, Nagano T, Okabe T, Wakita T, Shimizu H. 2013. Oxysterol-Binding Protein Family I Is the Target of Minor Enviroxime-Like Compounds. Journal of Virology 87:4252-4260.
6. Strating JRPM, van der Linden L, Albulescu L, Bigay J, Arita M, Delang L, Leyssen P, van der Schaar HM, Lanke KHW, Thibaut HJ, Ulferts R, Drin G, Schlinck N, Wubbolts RW, Sever N, Head SA, Liu JO, Beachy PA, De Matteis MA, Shair MD, Olkkonen VM, Neyts J, van Kuppeveld FJM. 2015. Itraconazole Inhibits Enterovirus Replication by Targeting the Oxysterol-Binding Protein. Cell Reports 10:600-615.
7. Ishikawa-Sasaki K, Nagashima S, Taniguchi K, Sasaki J. 2018. Model of OSBP-Mediated Cholesterol Supply to Aichi Virus RNA Replication Sites Involving Protein-Protein Interactions among Viral Proteins, ACBD3, OSBP, VAP-A/B, and SAC1. J Virol 92.
8. Wang HL, Perry JW, Lauring AS, Neddermann P, De Francesco R, Tai AW. 2014. Oxysterol-Binding Protein Is a Phosphatidylinositol 4-Kinase Effector Required for HCV Replication Membrane Integrity and Cholesterol Trafficking. Gastroenterology 146:1373-+.
9. Arita M. 2016. Mechanism of Poliovirus Resistance to Host Phosphatidylinositol-4 Kinase III beta Inhibitor. Acs Infectious Diseases 2:140-148.
10. Lyoo H, Dorobantu CM, van der Schaar HM, van Kuppeveld FJM. 2017. Modulation of proteolytic polyprotein processing by coxsackievirus mutants resistant to inhibitors targeting phosphatidylinositol-4-kinase IIIbeta or oxysterol binding protein. Antiviral Res 147:86-90.
11. Towner JS, Ho TV, Semler BL. 1996. Determinants of membrane association for poliovirus protein 3AB. J Biol Chem 271:26810-8.
12. Wessels E, Notebaart RA, Duijsings D, Lanke K, Vergeer B, Melchers WJG, van Kuppeveld FJM. 2006. Structure-function analysis of the coxsackievirus protein 3A - Identification of residues important for dimerization, viral RNA replication, and transport inhibition. Journal of Biological Chemistry 281:28232-28243.
13. Romero-Brey I, Berger C, Kallis S, Kolovou A, Paul D, Lohmann V, Bartenschlager R. 2015. NS5A Domain 1 and Polyprotein Cleavage Kinetics Are Critical for Induction of Double-Membrane Vesicles Associated with Hepatitis C Virus Replication. MBio 6:e00759.
14. Oudshoorn D, Rijs K, Limpens R, Groen K, Koster AJ, Snijder EJ, Kikkert M, Barcena M. 2017. Expression and Cleavage of Middle East Respiratory Syndrome Coronavirus nsp3-4 Polyprotein Induce the Formation of Double-Membrane Vesicles That Mimic Those Associated with Coronaviral RNA Replication. MBio 8.
15. Diaz A, Zhang JT, Ollwerther A, Wang XF, Ahlquist P. 2015. Host ESCRT Proteins Are Required for Bromovirus RNA Replication Compartment Assembly and Function. Plos Pathogens 11.
16. Diaz A, Wang XF, Ahlquist P. 2010. Membrane-shaping host reticulon proteins play crucial roles in viral RNA replication compartment formation and function. Proceedings of the National Academy of Sciences of the United States of America 107:16291-16296.
17. Tang WF, Yang SY, Wu BW, Jheng JR, Chen YL, Shih CH, Lin KH, Lai HC, Tang P, Horng JT. 2007. Reticulon 3 binds the 2C protein of enterovirus 71 and is required for viral replication. J Biol Chem 282:5888-98.
18. Lippincott-Schwartz J, Phair RD. 2010. Lipids and cholesterol as regulators of traffic in the endomembrane system. Annu Rev Biophys 39:559-78.

19. Yesylevskyy SO, Demchenko AP, Kraszewski S, Ramseyer C. 2013. Cholesterol induces uneven curvature of asymmetric lipid bilayers. ScientificWorldJournal 2013:965230.
20. Kawakami LM, Yoon BK, Jackman JA, Knoll W, Weiss PS, Cho NJ. 2017. Understanding How Sterols Regulate Membrane Remodeling in Supported Lipid Bilayers. Langmuir 33:14756-14765.
21. Ilnytska O, Santiana M, Hsu NY, Du WL, Chen YH, Viktorova EG, Belov G, Brinker A, Storch J, Moore C, Dixon JL, Altan-Bonnet N. 2013. Enteroviruses Harness the Cellular Endocytic Machinery to Remodel the Host Cell Cholesterol Landscape for Effective Viral Replication. Cell Host & Microbe 14:281-293.
22. Strating JR, van der Schaar HM, van Kuppeveld FJ. 2013. Cholesterol: fa(s)t-food for enterovirus genome replication. Trends Microbiol 21:560-1.
23. Schlegel A, Giddings TH, Jr., Ladinsky MS, Kirkegaard K. 1996. Cellular origin and ultrastructure of membranes induced during poliovirus infection. J Virol 70:6576-88.
24. Richards AL, Soares-Martins JAP, Riddell GT, Jackson WT. 2014. Generation of Unique Poliovirus RNA Replication Organelles. Mbio 5.
25. Belov GA, Nair V, Hansen BT, Hoyt FH, Fischer ER, Ehrenfeld E. 2012. Complex Dynamic Development of Poliovirus Membranous Replication Complexes. Journal of Virology 86:302-312.
26. Limpens RWAL, van der Schaar HM, Kumar D, Koster AJ, Snijder EJ, van Kuppeveld FJM, Barcena M. 2011. The Transformation of Enterovirus Replication Structures: a Three-Dimensional Study of Single- and Double-Membrane Compartments. Mbio 2.
27. Lai JKF, Sam IC, Chan YF. 2016. The Autophagic Machinery in Enterovirus Infection. Viruses-Basel 8.
28. Bienz K, Egger D, Pasamontes L. 1987. Association of Polioviral Proteins of the P2-Genomic Region with the Viral Replication Complex and Virus-Induced Membrane Synthesis as Visualized by Electron-Microscopic Immunocytochemistry and Autoradiography. Virology 160:220-226.
29. Rust RC, Landmann L, Gosert R, Tang BL, Hong WJ, Hauri HP, Egger D, Bienz K. 2001. Cellular COPII proteins are involved in production of the vesicles that form the poliovirus replication complex. Journal of Virology 75:9808-9818.
30. Rubino L, Russo M. 1998. Membrane targeting sequences in tombusvirus infections. Virology 252:431-437.
31. Miller DJ, Schwartz MD, Dye BT, Ahlquist P. 2003. Engineered retargeting of viral RNA replication complexes to an alternative intracellular membrane. Journal of Virology 77:12193-12202.
32. Boura E, Nencka R. 2015. Phosphatidylinositol 4-kinases: Function, structure, and inhibition. Exp Cell Res 337:136-45.
33. Clayton EL, Minogue S, Waugh MG. 2013. Mammalian phosphatidylinositol 4-kinases as modulators of membrane trafficking and lipid signaling networks. Progress in Lipid Research 52:294-304.
34. Blumental-Perry A, Haney CJ, Weixel KM, Watkins SC, Weisz OA, Aridor M. 2006. Phosphatidylinositol 4-phosphate formation at ER exit sites regulates ER export. Developmental Cell 11:671-682.

35. Xu K, Huang TS, Nagy PD. 2012. Authentic In Vitro Replication of Two Tombusviruses in Isolated Mitochondrial and Endoplasmic Reticulum Membranes. Journal of Virology 86:12779-12794.
36. Jonczyk M, Pathak KB, Sharma M, Nagy PD. 2007. Exploiting alternative subcellular location for replication: Tombusvirus replication switches to the endoplasmic reticulum in the absence of peroxisomes. Virology 362:320-330.
37. Kopek BG, Perkins G, Miller DJ, Ellisman MH, Ahlquist P. 2007. Three-dimensional analysis of a viral RNA replication complex reveals a virus-induced mini-organelle. Plos Biology 5:2022-2034.
38. Cortese M, Goellner S, Acosta EG, Neufeldt CJ, Oleksiuk O, Lampe M, Haselmann U, Funaya C, Schieber N, Ronchi P, Schorb M, Pruunsild P, Schwab Y, Chatel-Chaix L, Ruggieri A, Bartenschlager R. 2017. Ultrastructural Characterization of Zika Virus Replication Factories. Cell Reports 18:2113-2123.
39. Gillespie LK, Hoenen A, Morgan G, Mackenzie JM. 2010. The endoplasmic reticulum provides the membrane platform for biogenesis of the flavivirus replication complex. J Virol 84:10438-47.
40. Welsch S, Miller S, Romero-Brey I, Merz A, Bleck CKE, Walther P, Fuller SD, Antony C, Krijnse-Locker J, Bartenschlager R. 2009. Composition and Three-Dimensional Architecture of the Dengue Virus Replication and Assembly Sites. Cell Host & Microbe 5:365-375.
41. Knoops K, Kikkert M, van den Worm SHE, Zevenhoven-Dobbe JC, van der Meer Y, Koster AJ, Mommaas AM, Snijder EJ. 2008. SARS-coronavirus replication is supported by a reticulovesicular network of modified endoplasmic reticulum. Plos Biology 6:1957-1974.
42. de Wilde AH, Raj VS, Oudshoorn D, Bestebroer TM, van Nieuwkoop S, Limpens RWAL, Posthuma CC, van der Meer Y, Barcena M, Haagmans BL, Snijder EJ, van den Hoogen BG. 2013. MERS-coronavirus replication induces severe in vitro cytopathology and is strongly inhibited by cyclosporin A or interferon-alpha treatment. Journal of General Virology 94:1749-1760.
43. Knoops K, Barcena M, Limpens RW, Koster AJ, Mommaas AM, Snijder EJ. 2012. Ultrastructural characterization of arterivirus replication structures: reshaping the endoplasmic reticulum to accommodate viral RNA synthesis. J Virol 86:2474-87.
44. Romero-Brey I, Merz A, Chiramel A, Lee JY, Chlanda P, Haselman U, Santarella-Mellwig R, Habermann A, Hoppe S, Kallis S, Walther P, Antony C, Krijnse-Locker J, Bartenschlager R. 2012. Three-Dimensional Architecture and Biogenesis of Membrane Structures Associated with Hepatitis C Virus Replication. Plos Pathogens 8.
45. Monaghan P, Cook H, Jackson T, Ryan M, Wileman T. 2004. The ultrastructure of the developing replication site in foot-and-mouth disease virus-infected BHK-38 cells. J Gen Virol 85:933-46.
46. Short JR, Speir JA, Gopal R, Pankratz LM, Lanman J, Schneemann A. 2016. Role of Mitochondrial Membrane Spherules in Flock House Virus Replication. Journal of Virology 90:3676-3683.
47. Fogg MH, Teterina NL, Ehrenfeld E. 2003. Membrane requirements for uridylylation of the poliovirus VPg protein and viral RNA synthesis in vitro. J Virol 77:11408-16.
48. van Hemert MJ, van den Worm SHE, Knoops K, Mommaas AM, Gorbalenya AE, Snijder EJ.

2008. SARS-coronavirus replication/transcription complexes are membrane-protected and need a host factor for activity in vitro. Plos Pathogens 4.
49. Bienz K, Egger D, Pfister T, Troxler M. 1992. Structural and Functional-Characterization of the Poliovirus Replication Complex. Journal of Virology 66:2740-2747.
50. Neufeldt CJ, Joyce MA, Van Buuren N, Levin A, Kirkegaard K, Gale Jr M, Tyrrell DLJ, Wozniak RW. 2016. The Hepatitis C Virus-Induced Membranous Web and Associated Nuclear Transport Machinery Limit Access of Pattern Recognition Receptors to Viral Replication Sites. PLOS Pathogens 12:e1005428.
51. Wu B, Peisley A, Richards C, Yao H, Zeng X, Lin C, Chu F, Walz T, Hur S. 2013. Structural basis for dsRNA recognition, filament formation, and antiviral signal activation by MDA5. Cell 152:276-89.
52. Feng Q, Langereis MA, Lork M, Nguyen M, Hato SV, Lanke K, Emdad L, Bhoopathi P, Fisher PB, Lloyd RE, van Kuppeveld FJ. 2014. Enterovirus 2Apro targets MDA5 and MAVS in infected cells. J Virol 88:3369-78.
53. Barral PM, Sarkar D, Fisher PB, Racaniello VR. 2009. RIG-I is cleaved during picornavirus infection. Virology 391:171-6.
54. Nugent CI, Johnson KL, Sarnow P, Kirkegaard K. 1999. Functional coupling between replication and packaging of poliovirus replicon RNA. Journal of Virology 73:427-435.
55. Liu Y, Wang CL, Mueller S, Paul AV, Wimmer E, Jiang P. 2010. Direct Interaction between Two Viral Proteins, the Nonstructural Protein 2C(ATPase) and the Capsid Protein VP3, Is Required for Enterovirus Morphogenesis. Plos Pathogens 6.
56. Malathi K, Dong B, Gale M, Jr., Silverman RH. 2007. Small self-RNA generated by RNase L amplifies antiviral innate immunity. Nature 448:816-9.
57. Han JQ, Townsend HL, Jha BK, Paranjape JM, Silverman RH, Barton DJ. 2007. A phylogenetically conserved RNA structure in the poliovirus open reading frame inhibits the antiviral endoribonuclease RNase L. J Virol 81:5561-72.
58. Jiang P, Liu Y, Ma HC, Paul AV, Wimmer E. 2014. Picornavirus morphogenesis. Microbiol Mol Biol Rev 78:418-37.
59. Chen YH, Du WL, Hagemeijer MC, Takvorian PM, Pau C, Cali A, Brantner CA, Stempinski ES, Connelly PS, Ma HC, Jiang P, Wimmer E, Altan-Bonnet G, Altan-Bonnet N. 2015. Phosphatidylserine Vesicles Enable Efficient En Bloc Transmission of Enteroviruses. Cell 160:619-630.
60. Bird SW, Maynard ND, Covert MW, Kirkegaard K. 2014. Nonlytic viral spread enhanced by autophagy components. Proc Natl Acad Sci U S A 111:13081-6.
61. Taylor MP, Burgon TB, Kirkegaard K, Jackson WT. 2009. Role of microtubules in extracellular release of poliovirus. J Virol 83:6599-609.
62. Schwartz M, Chen J, Lee WM, Janda M, Ahlquist P. 2004. Alternate, virus-induced membrane rearrangements support positive-strand RNA virus genome replication. Proc Natl Acad Sci U S A 101:11263-8.

NEDERLANDSE SAMENVATTING

In dit proefschrift worden verschillende aspecten van replicatie organellen (RO's), die tijdens een picornavirus infectie in de cel ontstaan, onderzocht. **Hoofdstuk 1** bevat een inleiding over de rol en het belang van deze picornavirus RO's. Ook komen er belangrijke vraagstukken die nog opgehelderd moeten worden aan bod, zoals wat de oorsprong van RO's is, wat de vereisten zijn voor het ontstaan ervan, en welke functies de RO's hebben. De verschillende methodes die worden gebruikt om deze vragen te beantwoorden worden tevens uitgelegd, met name de voordelen van "Serial Block-Face Scanning Electron Microscopy" (SFB-SEM). Deze techniek maakt het mogelijk om, in tegenstelling tot conventionele Electronen Microscopie (EM), gehele cellen te bestuderen, hetgeen ongekende contextuele informatie oplevert. De technieken en methoden die tijdens dit werk zijn ontwikkeld en gebruikt bieden nieuwe mogelijkheden voor vervolg studies naar vorm en functie van RO's.

In **Hoofdstuk 2** wordt de constructie en toepassing besproken van een enterovirus dat een zogeheten split-GFP-tag draagt in zijn genoom. Deze kleine split-GFP-tag wordt geïntroduceerd in het RO-geassocieerde 3A eiwit en zal ervoor zorgen dat de enterovirus RO's groen zullen oplichten tijdens infectie. De implementatie en validatie van dit split-GFP virus komen achtereenvolgens aan bod. Als eerste wordt aangetoond dat de introductie van de split-GFP-tag in het enterovirale 3A eiwit geen nadelige gevolgen heeft voor de bekende functies van dit eiwit. Vervolgens wordt met Correlatieve Licht en Electronen Microscopie (CLEM) bewezen dat de RO's geïnduceerd door het split-GFP virus inderdaad groen oplichten en een morfologie hebben die karakteristiek is voor enterovirus RO's. Tot slot wordt in levende cellen onderzocht wat de ruimtelijke en chronologische relatie is tussen de vorming van enterovirus RO's en het uiteenvallen van het Golgi apparaat. Dit split-GFP virus omzeilt de beperkingen van het gebruik van grote fluorescerende eiwitten, die niet worden getolereerd in het enterovirale genoom, en is een elegant antwoord op het ontbreken van de mogelijkheid om enterovirale RO's in levende, geinfecteerde cellen te bestuderen.

De split-GFP methodologie die gepresenteerd is in **Hoofdstuk 2** wordt in **Hoofdstuk 3** gebruikt om de rol van PI4P lipides tijdens enterovirus infectie te bestuderen. Dit maal wordt de split-GFP-tag geïntroduceerd in het 3A eiwit van een mutant enterovirus. Dit mutante enterovirus is in staat om zichzelf te vermenigvuldigen wanneer de activiteit van PI4KB, een kinase dat PI4P lipides synthetiseert, wordt geremd. Hiermee zijn de effecten van lage PI4P concentraties op de vorming van enterovirus RO's bestudeerd. Eerst wordt met Transmissie Electronen Microscopie (TEM) aangetoond dat er geen RO's aanwezig zijn in cellen die geïnfecteerd zijn met het mutante virus in aanwezigheid van de PI4KB remmer. Dit resultaat is het eerste bewijs dat langdurige replicatie van het enterovirale genome kan plaatsvinden in afwezigheid van RO's of andere modificaties van de intracellulaire membranen. Met CLEM is gevonden dat de genoom replicatie onder deze condities daarentegen plaatsvindt op een schijnbaar intact Golgi apparaat. Deze bevinding wordt bevestigd met autoradiografie studies, die direct bewijs leveren voor viraal genoom synthese op het Golgi laat in infectie. Deze resultaten samen suggereren dat PI4P lipides een belangrijke rol spelen in het uiteen vallen van het Golgi apparaat en vervolgens tijdens de vorming van enterovirus RO's. Om dit verder te onderzoeken is een replicatie-onafhankelijk systeem opgezet, waarmee wordt bevestigd

dat de aanwezigheid van PI4P lipides het ontstaan van RO's versnelt, maar niet strikt noodzakelijk is voor RO vorming. Deze rol van PI4P lipides blijkt niet verweven te zijn met de rol tijdens de proteolytische digestie van het enterovirale "polyprotein". De intrigerende eigenschap van dit mutante enterovirus om zichzelf te vermenigvuldigen in de afwezigheid van RO's is vervolgens benut om de functies van RO's verder te onderzoeken. Replicatie in afwezigheid van RO's blijkt geen zichtbare effecten te hebben op interferon beta levels, hetgeen vraagtekens zet bij de notie dat RO's een cruciale rol spelen in het ontwijken van de aangeboren afweer tegen virale infecties.

In **Hoofdstuk 4** worden de donor organellen die gekaapt worden voor de vorming van enterovirus RO's opgehelderd. Dit is bewerkstelligd door het vastleggen van het moment van ontstaan van RO's uit het donor organel met behulp van het split-GFP virus, dat in **Hoofdstuk 2** is beschreven, en de SBF-SEM techniek. Hiervoor zijn levende, geïnfecteerde cellen gemonitord en gefixeerd op het moment dat de eerste groene RO's verschenen. Deze gefixeerde cellen zijn onderworpen aan SBF-SEM om zo CLEM informatie van de gehele cel te verkrijgen. Verrassend genoeg is gevonden dat de eerste RO's ontstaan uit het endoplasmatisch reticulum en wat later in infectie uit het trans-Golgi netwerk. Dit suggereert dat beide organellen het ontstaan van enterovirus RO's ondersteunen, waardoor schijnbaar conflicterende hypotheses over de oorsprong van RO's worden verenigd. Daarnaast zijn in deze data fysieke connecties tussen RO's en "lipid droplets" gedetecteerd, die mogelijk wijzen op een route voor lipide uitwisseling tussen beide die belangrijk is voor replicatie van het enterovirale genoom. Deze rijke dataset illustreert de voordelen van de SBF-SEM techniek gecombineerd met fluorescentie, waarmee contextuele informatie van de gehele cel kan worden vastgesteld.

In **Hoofdstuk 5** worden de RO's van een ander picornavirus bestudeerd, te weten een cardiovirus. Electronen Tomografie wordt toepast om de driedimensionale morfologie van de cardiovirus RO's op verschillende tijdstippen van infectie op te helderen. Deze studie toont aan dat sferische cardiovirus RO's met een enkelvoudig membraan ontspringen uit het endoplasmatisch reticulum en vervolgens transformeren in blaasjes met een dubbelvoudige membraan naarmate de infectie vordert. Daarnaast wordt aangetoond met een cardiovirus mutant, die zichzelf kan vermenigvuldigen bij lage concentraties van PI4P lipides, dat PI4P lipides een belangrijke rol spelen bij de vorming van cardiovirus RO's. Deze overeenkomsten en de verschillen met enterovirussen wordt besproken in de context van de gelijkenissen tussen verschillende picornavirussen.

Hoofdstuk 6 bevat een algemene disccusie van de verschillende hoofdstukken, waarbij de belangrijkste bevindingen worden gebruikt om nieuwe thema's in het onderzoek naar positief-strengs RNA virussen uit te lichten. De belangrijke rol van PI4P lipides voor verschillende aspecten van picornavirus replicatie wordt besproken. Mogelijke functies van picornavirus RO's, in het bijzonder die van de blaasjes met een dubbelvoudige membraan die later in infectie ontstaan, worden bediscusieerd. Het zichtbare gemak waarmee sommige picornavirussen verschillende organellen en intracellulaire membranen kunnen benutten voor de vorming van RO's benadrukt dat niet zozeer de oorsprong of morfologie van RO's, maar juist de specifieke functionele vereisten van het replicatie membraan cruciaal zijn voor picornavirus replicatie.

CURRICULUM VITAE

Charlotte Melia was born on 30th August 1989 in Bolton, United Kingdom, where she completed her secondary school education. She undertook her undergraduate studies at the University of York, United Kingdom, in 2007, and was awarded a BSc in Biology in 2011. She subsequently attained a post-graduate Bioscience Technology MSc qualification at the University of York in 2013. As part of this qualification Charlotte undertook research with Dr. Lucy M. Collinson at Cancer Research UK, London, studying the morphology and composition of the nucleoplasmic reticulum by light and electron microscopy. Charlotte then moved to the Netherlands where she carried out her PhD research in the group of Prof. Abraham J. Koster at Leiden University Medical Center under the supervision of Dr. Montserrat Bárcena. In 2018, Charlotte joined the group of Dr. Tanmay Bharat at the Sir William Dunn School of Pathology, University of Oxford, United Kingdom, studying bacterial biofilms and their formation using (cryo)electron microscopy.

LIST OF PUBLICATIONS

Locating macromolecules and determining structures inside bacterial cells using electron cryotomography
Melia CE and Bharat TAM
Biochmica et Biophysica Acta - Proteins & Proteomics. 2018 Sept 9:973-981

The Origin, Dynamic Morphology, and PI4P-Independent Formation of Encephalomyocarditis Virus Replication Organelles
Melia CE, van der Schaar HM, de Jong AWM, Snijder EJ, Koster AJ, van Kuppeveld FJ, Bárcena M.
mBio. 2018 Apr 17;9(2).

Escaping Host Factor PI4KB Inhibition: Enterovirus Genomic RNA Replication in the Absence of Replication Organelles
Melia CE*, van der Schaar HM*, Lyoo H, Limpens RWAL, Feng Q, Wahedi M, Overheul GJ, van Rij RP, Snijder EJ, Koster AJ, Bárcena M, van Kuppeveld FJ
Cell Reports. 2017 Oct 21:587-599. *Joint first authorship

Illuminating the Sites of Enterovirus Replication in Living Cells by Using a Split-GFP-Tagged Viral Protein
van der Schaar HM*, Melia CE*, van Bruggen JA, Strating JR, van Geenen ME, Koster AJ, Bárcena M, van Kuppeveld FJ
mSphere. 2016 Jul 6;1(4). *Joint first authorship

Correlative and integrated light and electron microscopy of in-resin GFP fluorescence, used to localise diacylglycerol in mammalian cells
Peddie CJ, Blight K, Wilson E, Melia C, Marrison J, Carzaniga R, Domart MC, O'Toole P, Larijani B, Collinson LM.
Ultramicroscopy. 2014 Aug;143:3-14.

SHORTLIST OF FREQUENTLY USED ABBREVIATIONS

TEM	Transmission electron microscopy
SEM	Scanning electron microscopy
SBF-SEM	Serial block-face scanning electron microscopy
ET	Electron tomography
CLEM	Correlative light and electron microscopy
RO(s)	Replication organelle(s)
DMV	Double-membrane vesicle
SMV/T	Single-membrane vesicle/tubule
CVB3	Coxsackievirus 3B
EMCV	Encephalomyocarditis virus
PI4P	Phosphatidylinositol-4 phosphate
PI4KB	Phosphatidylinositol-4 kinase 3 beta
LD(s)	Lipid droplet(s)
IFN	Interferon
PKR	Protein kinase R
MAVS	Mitochondrial antiviral-signaling protein

